August 2015

Ultra-Thin Polymer Films and Hierarchical Composites: Processing and Mechanical Properties

Yujie Liu
UMassAmherst

Recommended Citation

Liu, Yujie, "Ultra-Thin Polymer Films and Hierarchical Composites: Processing and Mechanical Properties" (2015). *Doctoral Dissertations*. 379.
https://scholarworks.umass.edu/dissertations_2/379

ULTRA-THIN POLYMER FILMS AND HIERARCHICAL COMPOSITES: PROCESSING AND MECHANICAL PROPERTIES

A Dissertation Presented
by
YUJIE LIU

Submitted to the Graduate School of the
University of Massachusetts Amherst in partial fulfillment
of the requirements for the degree of

DOCTOR OF PHILOSOPHY

May 2015

Polymer Science and Engineering

ULTRA-THIN POLYMER FILMS AND HIERARCHICAL COMPOSITES: PROCESSING AND MECHANICAL PROPERTIES

A Dissertation Presented

by

YUJIE LIU

Approved as to style and content by:

____
Alfred J. Crosby, Chair

____
James J. Watkins, Member

____
Shelly Peyton, Member

____
David A. Hoagland, Department Head
Polymer Science and Engineering

To my grandpa and family, for always loving me

ACKNOWLEDGEMENTS

First, I would like to thank my advisor, Al Crosby, for taking me as his student, and encouraging me over the last five and a half years. Completing PhD is a long and challenging journey, but Al always inspired me and never gave up on me. I appreciate the knowledge and attitude about science that Al has passed to me. We are Crosby Group, and we do careful science.

Additionally, I would like to thank the rest of my committee, Jim Watkins and Shelly Peyton. Professor Watkins always encouraged me to think about research from a broad scientific perspectives, instead of just one or two. Professor Peyton has not only been my committee member, but also my collaborator. Thanks for teaching me about the breast cancer cells and helping me to always think about the big picture of my research. I would like to thank both of you for dedicating your time as my committee members.

Furthermore, I would like to thank Professor Todd Emrick and Jimmy Lawrence, for being patient collaborators to me, Professor Cécile Monteux for being an author on my paper and her constructive suggestions on my research, and Professor Tom McCarthy for his willingness to chat with me all the time.

My first scientific advisor, Professor Lin Li, and my first scientific mentor, Fu Yang, played an important role, guiding me to the graduate school life at UMASS Amherst. I enjoyed my undergraduate research experience with the group. Thanks for supporting me over these years.

The Crosby Group consists of a fantastic group of people for me. We hang out both inside and outside Conte, and we collaborate and brainstorm about research frequently. To all the previous and current group members, Derek, Chelsea, Andrew, Kate, Dinesh, Hyun

Suk, Jun, Yuri, Dong Yun, Aline, Mike, Sam, Cheol, Shelby, Sami, Marcos, Jon, Dan, Yu-Cheng, Minchao, Mike, Satyan, Shruti, Han-Yu, Richard, Kasey, Yongjin, and David, thanks for all your friendship and support. I would like to thank Dong Yun for being a fantastic mentor and teaching me how to be a scientist. Jon and Dan, they are a combo to me, both taking care of my academic and personal life. Thanks for always listening to me, calming me down, and cooking meals for me. I would like to thank Yu-Cheng for his willingness to discuss science with me all the time, he is an invaluable office mate. Minchao, thanks for being my partner, either in the lab or in the shopping mall.

Outside of Crosby group, I would like to acknowledge the Class of 2009. The laughs and tears that we shared together in our classes and cumulative exam study group (Jimmy, Xiaobo, Irem, Maria, Jinhye, and Polina). Furthermore, I would like to specifically thank Xiaobo, Irem, Maria, Jinhye, Polina, Miao, and Katie. To our girls group, Irem, Maria, Jinhye and Polina, thanks for being my sisters. I enjoyed our trips to Burlington, Cape Cod, and Polina’s wedding! Additionally, I would like to thank my Zumba friends, Brittany, Megan, Feng, Lin, Jin, and Olivia, for reminding me to smile to myself. I would also like to thank my ski and snowboard friends, Yihui, Hongbo, Jin, and Sheng, for encouraging me to take new challenges.

I would like to thank my best friends, Jingjing Wu, Yi Tang, Weiwei Huang, and Rina Sa. Even though we can barely see each other these years, I always feel that I am loved and supported by you.

This PhD journey would have been impossible without the endless support from my family. Dad, thanks for teaching me to always look ahead to the bright future and telling me that I can do it. Mom, thanks for being proud of me all the time. Grandpa, I miss you!

Thanks for being considerate. He taught me that being a black sheep is not a disaster, but it opens a broader space for me to explore and improve. Grandma, thanks for loving me from your deepest heart and teaching me to be an independent girl. I would like to specially thank my aunts and uncles, Hui Liu, Hua Wang, and Hao Wang, for their encouragements and supports. Finally, I would like to thank Sheng, who has been there taking care of me all the time. I am glad to have you in my life.

ABSTRACT

ULTRA-THIN POLYMER FILMS AND HIERARCHICAL COMPOSITES: PROCESSING AND MECHANICAL PROPERTIES

MAY 2015

YUJIE LIU, B.S., BEIJING UNIVERSITY OF CHEMICAL TECHNOLOGY

M.S., UNIVERSITY OF MASSACHUSETTS AMHERST

PH.D., UNIVERSITY OF MASSACHUSETTS AMHERST

Directed by: Professor Alfred J. Crosby

Properties and fabrications of ultra-thin polymer films and hierarchical composites are of great interest in packaging, electronics, separations, and other manufacturing fields. However, due to the inherently fragile nature of ultra-thin polymer films, measuring their properties has proven difficult. Additionally, variables controlling thin polymer patterns (e.g. substrate wetting property) and composites (weight percent of particulates in matrix) formation have not been fundamentally well understood. Within this spectrum, fundamental understanding of formation mechanisms of these patterns and composites are needed. Additionally, a new characterization technique is required to be able to measure the mechanical properties of fabricated composites and thin films.

The pattern (Chapter 2) and composite (Chapter 3) formation presented in this thesis is based upon flexible blade flow-coating, an evaporative self-assembly method. The impact of substrate wetting, varying from being hydrophobic (water advancing contact angle 113°) to hydrophilic (water advancing contact angle 27°), on polymer pattern formation is examined here (Chapter 2). We observe a variety of polystyrene structures including dots, hyper-branched patterns, stripes and lines that can be deposited on

substrates with a range of wetting properties. We propose the mechanism for these pattern formations as a balance between Marangoni instability and solute absorption. When adding quantum dot nanoparticles into the polymer (poly(methyl methacrylate) solution in the flow-coating process on hydrophilic substrates, we could obtain free-standing hierarchical nanocomposite films with alternating line and film structures (Chapter 3). The ability to guide assemblies of nanoparticles and polymers in designated areas in one step via flow-coating, provides new understanding of the flow competition of mixing two components which are both on the nanometer scale. Additionally, we introduce a method designated for ultra-thin film tensile testing (Chapter 4). We demonstrate the capability of this method by stretching two-dimensionally macroscopic, yet nanoscopically thin, polymer films on the surface of water. Through laser tracking of the force and displacement on the film, we characterize the full stress-strain response of brittle (polystyrene), ductile (polycarbonate), and rubbery (cross-linked polydimethylsiloxane) polymer thin films. In the brittle (polystyrene) films, we observe a precipitous decrease in mechanical properties (Young's modulus, strain at failure, and nominal stress at failure) for film thicknesses approaching the size of an individual polymer chain (~ 25 nm) yielding insights into polymer chain entanglement theory. To verify our hypothesis in polymer chain entanglement theory for determining failure properties of thin polymer films, we further study the molecular weight effect (853, 490, 137 and 61.8 kg/mol) of polystyrene on failure properties (Chapter 5). We compare maximum tensile strain, maximum tensile stress, and modulus respectively as a function of molecular weight as well as film thickness. We support our hypothesis on polymer inter-chain entanglements theory in thin polymer films by this molecular weight study. This thesis provides direct measurements of failure properties of ultra-thin films.

These findings have important implications for the design of materials used in wide range of applications, as well as for the pursuit of new fundamental understanding of polymer physics in confined states.

TABLE OF CONTENTS

Page

LIST OF TABLES

Table Page

LIST OF FIGURES

CHAPTER 1

INTRODUCTION

1.1 Project Overview

Polymers have quite successfully replaced traditional materials such as metals in our daily life and in product design across industries due to their extremely lightweight. For example, manufacturing compact size laptops meets our desire to carrying portable devices to work. Polymer thin films and patterns have been incorporated in a myriad of technological applications such as packaging, microelectronics, and separators, and are attractive materials due to their lightweight, cheap cost and easy processing. However, certain fundamental questions to improve their performance in these applications still remain unanswered. For example, how does the wetting property of the device substrate affect the formation of polymer patterns and how can we determine whether failure properties of thin polymer films induces failure in the device?

This thesis aims to provide reasonable answers to open questions in the field of polymer patterning and thin films. Properties of bulk polymers have been studied extensively, but knowledge learned from bulk cannot be translated directly to thin polymer films or patterns. This thesis investigates processing and mechanical properties of thin polymer films and patterns. Specifically, this thesis consists of two sections: one focuses on the fabrication of ordered patterns of polymers or polymer based nanocomposites, and the other focuses on the characterization of mechanical properties of thin polymer films.

In the first section, we utilize flow-coating to study the effect of substrate wetting on ordered homogeneous polymer pattern formation. Additionally, to extend the control of structure patterning to composites, we utilize flow-coating to fabricate hierarchical composites of nanoparticles and polymers with structured regions of high concentrations of nanoparticles. However, the direct characterization of the hierarchical composites cannot be fulfilled with current techniques, for example to characterize mechanical properties in different directions of the hierarchical composite. In the second section, we develop a new approach to directly measure complete stress-strain responses of thin homogeneous polymer films, which can enable the characterization of the hierarchical nanocomposite. Furthermore, we investigate polymer molecular weight effects on mechanical properties of thin polymer films to understand the fundamental polymer physics in confined states.

1.2 Evaporative Self Assembly

Evaporative self-assembly techniques have been developed to create ordered structures on nanometer to micron scales for a range of applications from electronics[1,2], optical sensors[3], biotechnology[4] to printing[5]. Several methods that utilize evaporative assemblies of nonvolatile solutes through irreversible solvent evaporation are dip-coating[6], Marangoni flow-induced self-assembly[7], constraining solutions in a sphere-on-flat geometry[8], and flow coating[9,10]. In particular, flow coating is a simple and inexpensive method to deposit uniform or gradient polymer thin films, stripes or grid patterns of polymer or nanoparticles[9–11] in a controlled manner. However, how the flow inside the solution affects patterning via evaporative assemblies has not been well studied. Our goal is to identify possible flows and underlying mechanisms, and apply these lessons to explain resulting patterns.

1.2.1 Evaporative Self Assembly from Droplets

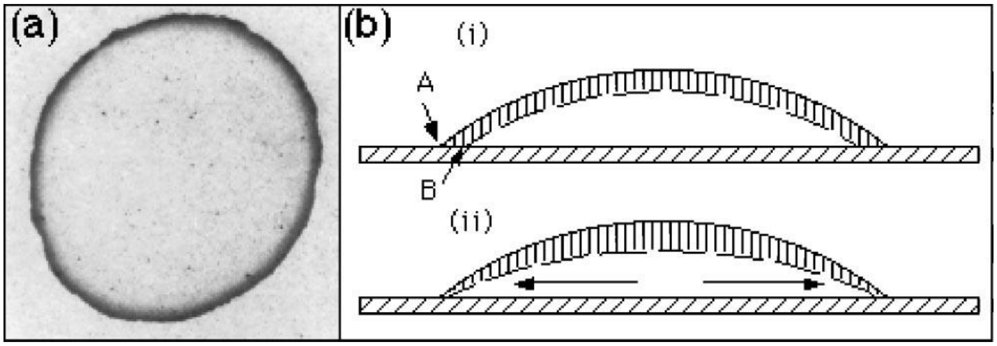

Figure 1.1 - Evaporation of a drying droplet. (a) A ring stains of dried coffee on a solid substrate. (b) Schematics demonstrate an outward capillary flow during evaporation to pin the contact line. (i) If the contact line were not pinned. (ii) The movement of the outward flow[13]. Reprinted with permission from Deegan, R. Pattern Formation in Drying Drops. *Phys. Rev. E. Stat. Phys. Plasmas. Fluids. Relat. Interdiscip. Topics* **2000**, *61*, 475–485.

Consider a spilled coffee drop on a solid substrate; after the solvent evaporates, a ring-like deposit will remain. This ring-like deposit is the commonly observed "coffee-ring" phenomenon which also applies to other nonvolatile solutes, such as DNA, colloids, and polymers[12–14]. Deegan and co-workers first explained the essential physics behind the ring formation (Figure 1.1)[12–14]. They found that the pinning of contact line to its initial position and the evaporation of solvent are two requirements for the ring formation. To pin the contact line, an outward flow carrying solute moves towards the contact line to replenish the evaporation at the contact line, where the highest evaporation rate is achieved.

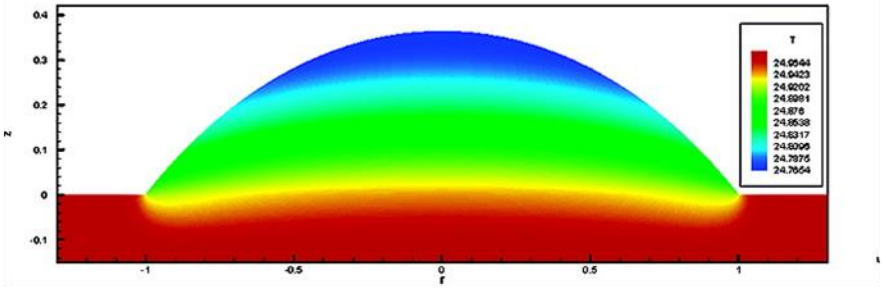

Figure 1.2 - Temperature gradient in a drying droplet on a substrate with contact angle of 40°[14]. Reprinted with permission from Hu, H.; Larson, R. G. Analysis of the Effects of Marangoni Stresses on the Microflow in an Evaporating Sessile Droplet. *Langmuir* **2005**, *21*, 3972–3980.

Meanwhile the ring shape is dictated by surface tension is responsible for the spherical cap shape of droplet.

To understand the state inside the droplet, having knowledge of the final deposition is not enough. Researchers have worked on revealing the solute concentration field[15,16] and have shown that the solute concentration is a function of evaporation time and droplet radius[15]. This finding indicates that the loss of solute at the center region is induced by outward flow. The increase in concentration can possibly create viscous regions at the edge, and viscous forces induced by viscosity differences also need to be considered[16].

Marangoni flow, that is the flow from lower surface tension to higher surface tension in the solution, becomes significant in solutions with organic solvents (octane and hexane for example)[17–19] or water with surfactants[16,20,21], in addition to the outward capillary flow. Surface tension gradients in Marangoni flow can be caused by either temperature gradient (thermal Marangoni) or concentration gradient (solutal Marangoni). Thermal Marangoni flow (Figure 1.2), results in solute deposition preferentially at the center of the droplet[14]. Solutal Marangoni, in combination with viscous force in the vicinity of concentrated region near the edge, leaves a polymer film instead of a coffee-ring[16]. Due to the role played by Marangoni flow in a drying droplet, many researchers have reported ordered patterns including rings and hexagonal arrays[18,19], polygons[20], hexagonal and stripe-like patterns[7], and micro-channels[21].

As the droplet evaporates, a series of rings and other patterns are deposited besides one ring at the periphery ("coffee-ring effect")[22–24] in dilute solutions of colloids, DNAs and polymers. Researchers believe that multiple rings result from the "stick-slip" motion of the contact line and this motion follows an oscillatory process[22–25]. First, the contact line is self-pinned. Accumulation of solute deposition at the contact line also enhances pinning. This pinning is referred as “stick”. Second, as the droplet evaporates while the contact line is pinned, the contact angle decreases. When it reaches a critical value, the contact line de-pins and recedes to a new position which is referred as “slip”. At the new position, the contact line “sticks” again and leaves a new ring, and then it “slips” to another position[12,22–25]. The “stick” and “slip” motion alternate as the solvent evaporates.

Besides flow states in the droplet, we also need to consider the role of substrates in solute depositions[14,16,26]. The substrate contact angle influences the evaporation rate of the droplet, which affects the amount of outward flow that carries solute for deposition[14,27]. At small contact angles, the evaporation rate and the transport of solute are enhanced at the contact line. As the contact angle increases, the evaporation rate slows down and the transport of solute diminishes[16,26]. The contact angle or wetting property of the substrate needs to be considered to control patterning, as it varies affects the transport of solute to deposition.

Most researchers have utilized the coffee-ring effect and the stick-slip motion of the contact line to assemble nonvolatile solutes on hydrophilic substrates. In some cases, regular polymer patterns have been reported[2,28,29]. However, these patterns are generally limited to the ring or line form[2,28,29], and few groups have attempted to finely control spacing between rings and lines in these patterns. Flow-coating, which creates various patterns and controls the stick-slip motion of the contact line in a programmed way, is a very promising technique to overcome this limitation[9,10].

1.2.2 Controlled Evaporative Assembly in a Confined Geometry

Without constrained solutions, dissipative structures (for example, coffee-rings and polygonal networks[12,20]) lacking in higher order regularity are usually formed from evaporative assemblies in a freely drying droplet. In contrast, controlled patterns (for example, stripes[24], grids[9], and concentric square stripes and rings[30–32]) are produced from evaporative assemblies in a confined geometry. Confined geometries include “curve on flat” geometry, and two parallel or nonparallel plates, which provide controls of evaporation dynamics (such as evaporation rate) and associated flows[33]. In the two parallel plates case, patterns of polymers and colloids are formed as dots[34], stripes[24], and ladders[35,36] by sliding one plate at a controlled velocity. In the two nonparallel plates case, regular depositions of polymers, colloids, and nanoparticles are formed as stripes, grids and more complex structures by sliding the upper angled plate at a controlled velocity[37] or by programming the movement of the bottom plate[1,9,10,38].

Evaporative assemblies in a confined geometry have improved regularity of deposited patterns from freely evaporating droplets. However, the ability to provide various shapes for patterns is still limited[7,12,18,20,21]. In addition, the stick-slip motion of the contact line to program the spacing between patterns is not well controlled[24,30,28,32,36,38]. Furthermore, most methods cannot achieve the fast deposition and form patterns over large area (on the order of cm by cm). To overcome these shortcomings, flow-coating technique is utilized to achieve fast deposition of patterns over large area in this thesis.

1.2.3 Flexible Blade Flow-Coating

Flow-coating is a simple, non-lithographic, and external-field-free technique to control patterning of polymers, nanoparticles, and polydimethylsiloxane (PDMS)[9,10]. Flexible blade flow-coating, a development from razor blade flow-coating, is recently reported and utilized in this thesis[10]. It enables smaller feature size of deposited pattern (on the nanometer scale), easier alignment of the blade, and smaller loading volume of the solution when compares to the razor blade flow-coating. With flexible blade as the upper confined plate, when dilute solutions are trapped between the flexible blade and substrate, the gap between the two plates is self-constrained with capillary force. Following the programmed velocity profile of the substrate (Figure 1.3b), stick-slip motion of the contact line can be manipulated by the computerized program. Since solutes assemblies occur

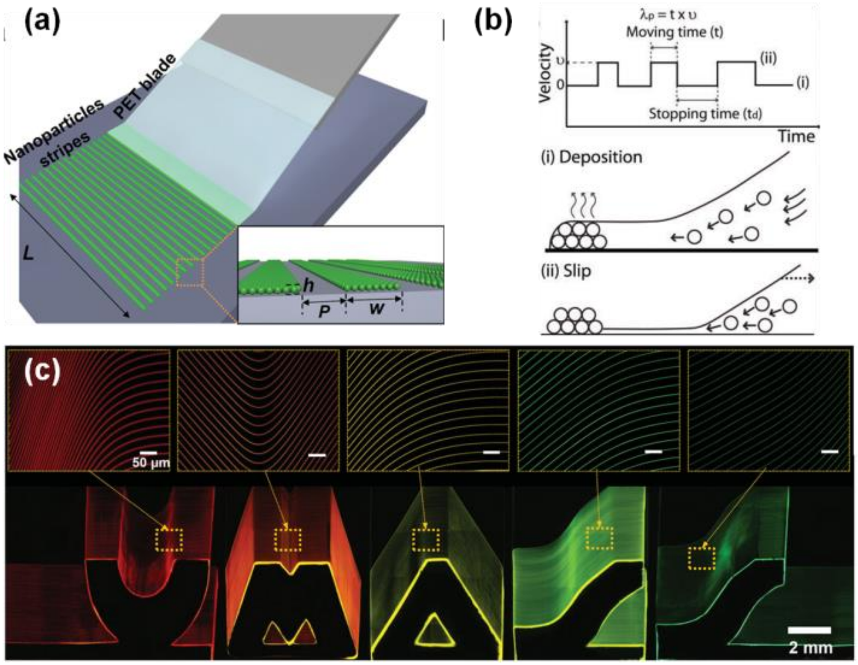

Figure 1.3 – Flexible blade flow-coating. (a) Schematic of flexible blade flow-coating in patterning stripes of nanoparticles[10]. (b) Velocity profile of the substrate to manipulate stick-slip motion of the contact line[9]. (i) Stick. (ii) Slip. (c) Centimeter scale "UMASS" pattern fabricated by the flexible blade flow-coating[10]. Reprinted with permission from Lee, D. Y.; Pham, J. T.; Lawrence, J.; Lee, C. H.; Parkos, C.; Emrick, T.; Crosby, A. J. Macroscopic Nanoparticle Ribbons and Fabrics. *Adv. Mater.* **2013**, *25*, 1248–1253; and Kim, H.; Lee, C.; Sudeep, P.; Emrick, T.; Crosby, A. J. Nanoparticle Stripes, Grids, and Ribbons Produced by Flow Coating. *Adv. Mater.* **2010**, *22*, 4600–4604.

parallel to the contact line, multiple shapes such as “blocky” stripes, “weaves,” and “UMASS” (Figure 1.3c) can be written by configuring the blade shape at the meniscus front[10]. Another advantage of flexible blade flow-coating is that features with nanometer scale in height and width, while centimeter scale in length are fabricated. The width and height profile of deposited patterns are affected by initial concentration and stopping time, while length is determined by the flexible blade.

Flexible blade flow-coating and other methods in evaporative assemblies under a confined geometry have utilized a wide range of patterns and materials with controllable depositions. However, few studies regarding wetting property of substrates effects on solutes patterning in evaporative assemblies have been carried out[39,40]; and details of flows at the meniscus front in confined evaporative assembly has not been investigated. This thesis will discuss mechanisms of patterning on substrates with different wetting properties, and possible flows at the meniscus front that affects pattern formation. In addition, fabrication of hierarchical nanocomposite of polymers and nanoparticles within one step processing by flow-coating is investigated.

1.3 Properties of Thin Polymer Films

Thin polymer films have been investigated comprehensively during the past decade for its uses in studies ranging from glass transition theory[41–44] to glass-phase physics[45–47], and technological applications include surface coatings, thin film transistors, separation membranes and electronic sensors. It has been widely observed that physical properties of thin polymer films including glass transition temperature[41–44], viscosity[48], and modulus[49–52] deviate from their bulk counterparts. Specifically, thin polystyrene films have been often used as the model material, because they can be easily fabricated and manipulated[53].

However, no consensus has been received on glass transition theory in confined thin film system. In addition, current methods largely yield only one property of thin films, usually from indirect measurements. For example, modulus from wrinkling patterns[54,55], and modulus from bubble inflation[56]. Few groups have attempted to characterize the full mechanical properties in thin polymer films including both elastic region and plastic region. There is a need to develop a new method that can directly measure mechanical properties of thin films, and that can characterize more than one property of the thin film.

1.3.1 The Glass Transition Temperature of Thin Polymer Films

Glass transition temperature (T_g) of polymer is a critical point that divides states of polymer chains into rubbery state (temperature above T_g) and glassy state (temperature below T_g)[57]. Even though T_g has been widely used as a key parameter in polymer processing, the underlying physics of T_g is not well understood. For example, whether the glass transition is a thermodynamic or kinetic phenomenon[41]. One way that researchers have chosen to understand this thermodynamic and kinetic question is by examining T_g of thin polymer films. As glass transition results in polymer chains to be cooperatively rearranging on the order of 1 nm[58], confinements of polymer chains in the thin polymer

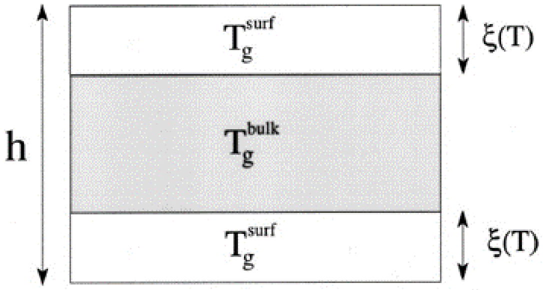

Figure 1.4 – Schematic of surface mobile layer occurrence in the free-standing thin PS film with low molecular weights. Surface mobile layer has a T_g labeled as T_g^{surf} and its characteristic length scale is a function of temperature, denoted as ξ(T)[61]. Reprinted with permission from Mattsson, J.; Forrest, J.; Borjesson, L. Quantifying Glass Transition Behavior in Ultrathin Free-Standing Polymer Films. *Phys. Rev. E. Stat. Phys. Plasmas. Fluids. Relat. Interdiscip. Topics* **2000**, *62,* 5187–5200.

film can perturb the size and arrangement of the cooperatively rearranging regions (CRRs) and yield new insights into the fundamental physics of T_g.

T_g of thin polymer films deviates from their bulk counterparts, but whether T_g increases or decreases in the thin film region depends on the experimental conditions[59], for example, whether the thin film is supported by substrates or not. For free-standing thin PS films, very large reductions in T_g are observed when film thickness is smaller than the end to end distance of polymer chain ($R_{EE} = 2R_g$)[41,60,61]. For thin PS films supported by substrates, interactions between thin films and substrates affect T_g. For example, when it is attractive interactions, smaller reductions in T_g or even an increase in T_g is observed[62].

For free-standing thin PS films, the T_g reduction is attributed to the occurrence of mobile surface layer[61,63,64] which higher mobility results in lower T_g than bulk. When varying molecular weights of PS, the degree of T_g reduction and the surface mobile layer

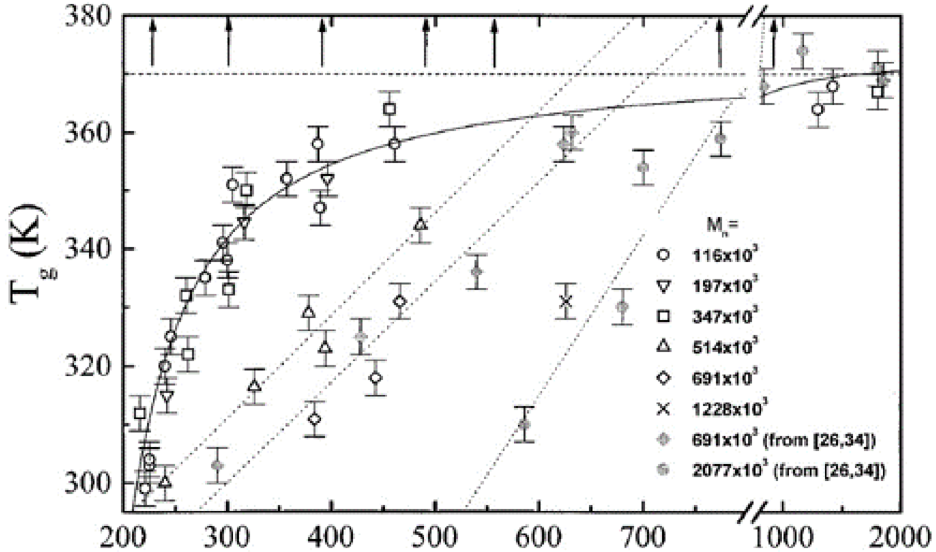

Figure 1.5 - T_g value measured by Brillouin light scattering of seven different molecular weights[61]. Reprinted with permission from Mattsson, J.; Forrest, J.; Borjesson, L. Quantifying Glass Transition Behavior in Ultrathin Free-Standing Polymer Films. *Phys. Rev. E. Stat. Phys. Plasmas. Fluids. Relat. Interdiscip. Topics* **2000**, *62*, 5187–5200.

length is affected. For low molecular weight PS (number average molecular weight, $M_n <$ 350 kg/mol), T_g is independent of molecular weight (Figure 1.4 and Figure 1.5)[61,65]. For high molecular weight PS ($M_n >$ 350 kg/mol), the threshold film thickness for T_g reduction is dependent on R_{EE} of the polymer chain, which is determined by PS molecular weight (Figure 1.5).

T_g measurements of thin films have suggested the enhanced surface mobility which predicts deviation in mechanical properties of thin films from bulk counterparts. However, from device manufacturing perspective, measurements of mechanical properties of thin polymer films instead of polymer chain mobility theory would provide more direct guidelines in manufacturing.

1.3.2 Mechanical Properties of Thin Polymer Films

In this thesis, we do not vary temperature to study mechanical properties of thin PS films, but examine their properties at room temperature.

1.3.2.1 Elastic Properties

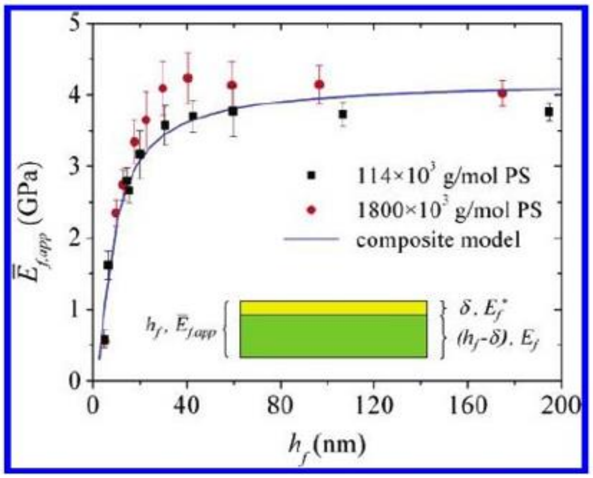

Figure 1.6 – Modulus of thin PS films as a function of film thickness for M_w of 114 kg/mol PS and 1800 kg/mol PS. A two layer composite model is proposed for explaining the modulus reduction[50]. Reprinted with permission from Stafford, C. M.; Vogt, B. D.; Harrison, C.; April, R. V; Re, V.; Recei, M.; June, V. Elastic Moduli of Ultrathin Amorphous Polymer Films. *Macromolecules* **2006**, *39*, 5095–5099.

Studies for thin PS films at room temperature have demonstrated that modulus of thin PS films deviates from the bulk[50,66,67]. For most tested molecular weights of thin PS films (usually M_n > 3.2 kg/mol[67]), the threshold film thickness for modulus reduction is approximately 40 nm[50,67]. As indicated by the T_g measurements of thin PS films, researchers have utilized the surface mobile layer to explain the modulus reduction[50,66,67]. For modulus measurements, instead of testing free-standing films for T_g, thin polymer films are usually supported by substrates (such as cross-linked polydimethylsiloxane (PDMS)[50,67] and silicon wafers[51,66]) or a medium (such as water[68,69]). In this way, one surface mobile layer with a underneath bulk like layer is proposed (Figure 1.6) [50].

The proposed two layer model fits the measured modulus of thin films well, but there are disagreements on the thickness of surface mobile layer. From fits to modulus value, the mobile surface layer at room temperature is suggested to be 2 nm[50], 6 nm[67], and 10 nm[53] respectively. In addition, by adding fluorescent probe into thin PS films, the mobile surface layer at room temperature is measured to be less than 1 nm[65]. These studies claim the mobile surface layer to be independent of total film thickness and PS molecular weight[50,53,65,67] which suggests a constant or comparable mobile surface layer thickness, but the proposed mobile layer thickness for PS varies from 1 nm to 10 nm.

Furthermore, many current studies[49,50,56,70] on modulus of thin PS films utilize secondary measurements of properties (including wrinkle wavelength and amplitude), to extrapolate modulus value, instead of direct measurements of modulus from stress-strain responses. Furthermore, many studies on thin film mechanical properties are limited to the elastic properties, and few studies have considered properties in the inelastic region, for example, failure properties of thin films, which is more important in real applications.

1.3.2.2 Failure or Close to Failure Properties

Further research has been continued to discover failure or close to failure properties of thin PS films by examining extension ratio[71] and thickness[47,72] of craze, critical yield strain[53], and onset fracture strain[70]. These researchers utilizing methods of wrinkling[53,70] to plastic region and straining to craze region[47] suggest that thinner polymer films will stretch further (Figure 1.7). However, instead of direct measurements of maximum tensile strain, these researchers use indirect properties (including wrinkle wavelength and amplitude[53,70], and neck thickness of craze[47]) together with proposed theories of thin polymer films to extrapolate maximum tensile strain. Considering if we use a different theory of thin polymer films, for example, the inter-chain entanglements dominated the mechanical failure strain[73,74], on the other hand, we would expect an opposite trend that thinner polymer films will stretch less. This expectation is supported by inter-chain entanglement density decrease in thinner polymer films[74], by the craze micromechanics which proposes lower stress for craze occurrence in thinner polymer films[71], as well as by the experimental

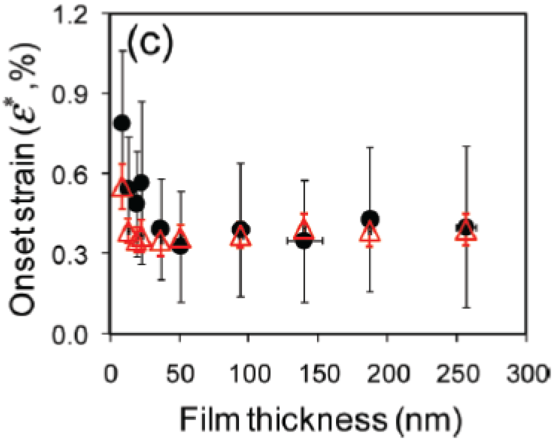

Figure 1.7 – Onset fracture strain of PS thin films plotted against film thickness[70]. Reprinted with permission from Lee, J.-H.; Chung, J. Y.; Stafford, C. M. Effect of Confinement on Stiffness and Fracture of Thin Amorphous Polymer Films. *ACS Macro Lett.* **2012**, *1*, 122–126.

craze measurements which demonstrates the increasing craze depth growth rate for thinner polymer films[72].

To quantify whether thin polymer film will stretch further or not, a new method that can directly measure failure properties of thin polymer films is needed. In addition, to consistently understand thin polymer film properties, this method should enable mechanical properties characterizations in elastic and inelastic (plastic) region in the same test. The full spectrum of mechanical properties of thin polymer films will better assist manufacturing and understanding of underlying physics, rather than a partial spectrum.

1.4 Dissertation Organization

We have introduced flexible blade flow-coating to fabricate organized polymer patterns and thin films on nanometer scale and the need for developing a new method to directly characterize mechanical properties of these thin films and patterns. In this thesis, we will increase our understanding of variables that control formations of ordered polymer patterns and composite films. We additionally develop a new method to directly and mechanically characterize thin polymer films properties, which will facilitate mechanical understanding of those fabricated polymer patterns.

Chapter 2 introduces the effects of substrate wetting on polymer pattern formation via flexible blade flow-coating. Variables of set distance in flow-coating, stopping time in flow-coating, initial concentration in solution, and wetting properties of substrates are systematically studied. In particular, the variables controlling hyper-branched polymer structure formations are investigated extensively. Through understanding the structure formation from solutions of polymers, we propose an explanation based on the competition between flow instabilities, solution viscosity and adsorption and friction to the substrate.

Chapter 3 focuses on the fabrication of hierarchical nanocomposite by flexible blade flow-coating in a one-step process. To understand the distribution of nanoparticles in the polymer matrix based nanocomposite, the volume fraction of nanoparticles in different regions of the nanocomposite must be known. This is preliminary work discussing the solute volume fraction measurements and possible ways to control the nanoparticle distribution. The results of this chapter demonstrate a simple way to fabricate large scale nanocomposites, which will serve as a model material for understanding structural effects on mechanical properties of thin nanocomposite films.

Chapter 4 moves away from fabrications of patterns and nanocomposites, and introduces the ultra-thin film tensile tester, a new method designed to directly measure the full stress-strain response of ultra-thin films. The ability of our tensile tester is demonstrated by characterizing brittle, ductile and elastomeric polymers in the thin film form. We propose that a decrease in inter-chain entanglements explains the failure property reduction in thin films compared to thick films. The results of this chapter demonstrates a general method for directly determining mechanical properties of ultra-thin films.

Chapter 5 expands the thin polymer film study by investigating the molecular weight dependence in mechanical properties. Maximum tensile strain, maximum tensile stress, and modulus are examined systematically by varying polymer chain molecular weight and thin film thickness. The inter-chain entanglements explanation in Chapter 4 is demonstrated to be effective to predict failure properties of polymer films with different molecular weights.

Chapter 6 concludes with lessons learned in this thesis. Additional future work is presented, to further study properties of thin polymer films and other materials, including hierarchical nanocomposites.

CHAPTER 2

HYPER-BRANCHED POLYMER STRUCTURES VIA FLEXIBLE BLADE FLOW-COATING

2.1 Introduction

Evaporative self-assembly techniques have been developed to create ordered structures on nanometer to micron scales for a range of potential applications from electronics[1,2] to printing[5]. Several techniques that use evaporative assembly have been reported, including dip-coating[6], Marangoni flow-induced self-assembly[7,75], constraining solutions in a sphere-on-flat geometry[8], and oscillating flow-coating[9,76]. In particular, flow-coating is a simple and inexpensive method to controllably deposit uniform or gradient polymer thin films, as well as stripe or grid patterns of polymers or nanoparticles[9,11,76].

For many of these methods, silicon-based substrates are commonly used. However, this material choice has presented problems for certain solutes. For example, polystyrene (PS) has been observed to form rings with fingers and rings with hole-punch-like structures on hydrophilic silicon wafers, rather than the typical, well-defined rings from a sphere-on-flat evaporative assembly process[8,77]. Although some understanding has been provided for the formation of such defects, a systematic study of substrate properties has not been conducted. Therefore, to fully realize the opportunities of confined evaporative assembly, such as flow-coating, the influence of substrate surface energy on the creation of structures must be understood.

In this Chapter, we investigate the effect of surface energy on structure formation during flexible blade flow coating[76] by tuning the substrate surface energy and varying flow-coating parameters with PS in toluene as a model solute. Upon modifying the surface energy of a silanized substrate with ultraviolet / ozone (UVO) exposure (which provides a range of water advancing contact angles from 112° to 34° as shown in Figure 2.1), we find that a variety of structures (such as hyper-branched structures and lines perpendicular or parallel to the flow receding direction) may be fabricated with flow-coating. In particular, our findings lead to the description of a mechanism for the formation of regular, centimeter scale hyper-branched structures due to the interplay between Marangoni flow and solute deposition on the surface.

2.2 Approach

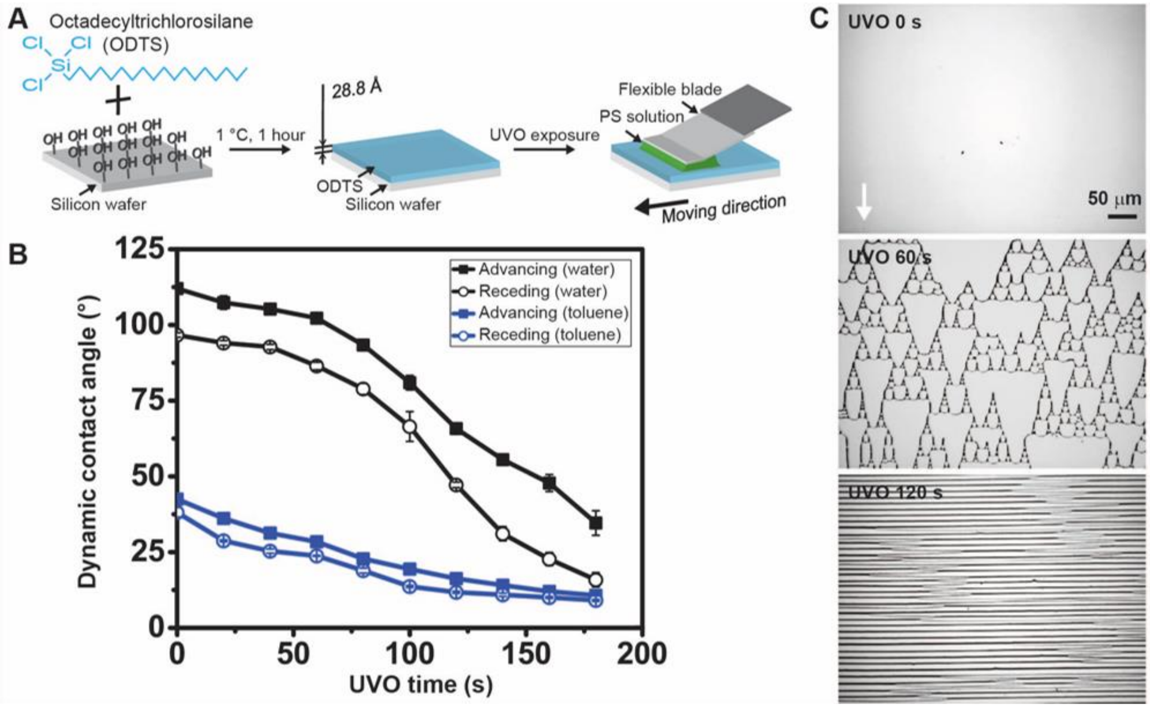

Figure 2.1 – Tune substrate surface energy and discover pattern formation on these substrates. (A) Schematic of preparing substrates with tunable surface energy and then applying flow-coating process. (B) Dynamic contact angles including advancing (solid data points) and receding (open data points) of substrates as a function of UVO time. Liquid of water (black data points) and toluene (blue data points) are used. The error bars denote standard deviation for three independent samples. (C) Structures fabricated on substrates with tunable surface energy, varying from no deposition, hyper-branched structures to horizontal lines via flow-coating. Other flow-coating parameters used here are initial concentration, c_o, as 0.5 mg/ml, stopping time, t, as 100 ms, and set distance, d, as 5 μm.

We utilize an evaporative self-assembly process based on flexible blade flow-coating to fabricate organized structures on substrates that have been modified to systematically vary surface energy. To analyze polymer structure formation, we change process parameters, including substrate surface energy, initial solution concentration, stopping time and set distance. Upon modifying the UVO exposure time on the silanized substrate, the wetting property or substrate surface energy can be tuned. Besides substrate surface energy, other process parameters can be varied through the computerized control program of flow-coating.

2.3 Experimental

2.3.1 Substrate Fabrication

Polished silicon wafer (100 mm diameter, ~ 500 µm thickness, 100 orientation, P/B doped, University Wafers) substrates (typically cut into 1.2 cm x 1.2 cm) were prepared by rinsing with toluene, acetone, and deionized water, drying under nitrogen, and then treating with Harrick oxygen plasma at 250 mTorr for 20 minutes. The oxide layer thickness was measured with ellipsometry (refractive index, n_1 = 1.46-setting by LSE Stokes ellipsometer, Gaertner, Inc.). Surface modified substrates were transferred to sealed 20 mL scintillation vials containing 1 µL n-octadecyltrichlorosilane (ODTS) (95%, Gelest, Inc.) and 999 µL toluene (use as received from Fisher Scientific) (0.1% ODTS by volume). Each vial was placed in an ice water bath for one hour to regulate the temperature to 1 °C. After one hour, the modified silicon wafer in each vial was rinsed and dried following the same pre-treatment process, but excluding the 20 minutes oxygen plasma treatment. The wafers were then baked in a 120 °C oven for two hours, allowed to cool to room temperature, and sonicated in toluene for 60 seconds. The wafers were again rinsed and dried. The thickness of the ODTS layer was measured with ellipsometry (ODTS, refractive index, $n_2 = 1.457$, Gelest, Inc.) as 28.8 ± 0.83 Å (averaged by 20 samples) (Figure 2.1A). To control surface energy, the modified ODTS layers were treated with UVO (Jelight 342 UVO system with the average lamp intensity in the range of 28 to 32 mW/cm^2 at the wavelength of 253.7 nm) for different exposure times. Immediately thereafter, the substrates were used for measuring dynamic contact angle or flow-coating.

2.3.2 Dynamic Contact Angle Measurement

Advancing and receding contact angles for ODTS treated substrates is determined using deionized water and toluene at room temperature (VCA-optima TM, AST, Inc.).

2.3.3 Flexible Blade Flow-coating of Polystyrene

Flow-coating is conducted with programmed velocity (v) (velocity the substrate moved), set distance (d) (distance the substrate moved), and stopping time (t) (time the substrate paused) under move-stop alternating steps. In this work, the programmed velocity, *v*, is kept constant at 1 mm/s. The flow-coating technique is discussed in detail in references (H. Kim et al[9] and D. Lee et al[76]). An improvement in the flow-coating technique has recently been reported[76] where a flexible polyethylene terephthalate (PET) blade is used as the top confining boundary. A flexible PET blade (75 µm x 2 cm x 4 cm) will be used in this work. A solvent region was made by scoring the PET blade 1 mm from the meniscus edge. The solution used for flow coating experiments reported here was polystyrene 0.0115 wt% to 0.1721 wt% in toluene solution (polystyrene, $M_n = 1100$ kg/mol, PDI = 1.15, Polymer Source, Inc.). *In situ* observation of structure formation was performed with an upright optical microscope (Zeiss Axio Tech Vario, Pixel Link CCD camera).

2.4 Results and Discussion

Various flow-coating parameters are used to form different structures, such as hyper-branched structures, lines perpendicular to the flow direction (which we will denote as “horizontal lines”), or lines parallel to the flow direction (which we will denote as “vertical stripes”). To explore the formation of these structures, we control the following parameters: UVO exposure time (to control the substrate surface energy), initial PS solution concentration (c_o), stopping time of flow-coating (t), and set distance of flow-coating (d).

2.4.1 Importance of Substrate Surface Energy (UVO Exposure Time)

UVO exposure time induces bond breaking and crosslinking in the ODTS layer to cause a change in surface energy of the ODTS modified substrate[78]. The increase in UVO exposure time leads to the decrease in the contact angle of water and toluene (Figure 2.1B). In our study, flow-coating a PS solution on UVO treated ODTS substrates with UVO exposure times between 0 s and 20 s results in no PS deposition (Figure 2.1C). As UVO exposure time increases to between 70 s to 180 s, horizontal lines of PS are deposited with spacing determined by the slip distance (the distance between pinning and depinning of the contact line)[76]. However, interestingly at 60 s of UVO exposure, hyper-branched structures are observed as well-aligned, self-similar triangles (Figure 2.1C).

One of the significant results of our work here is the formation of these hyper-branched structures on 60 s UVO exposed ODTS substrates via flow-coating. Importantly,

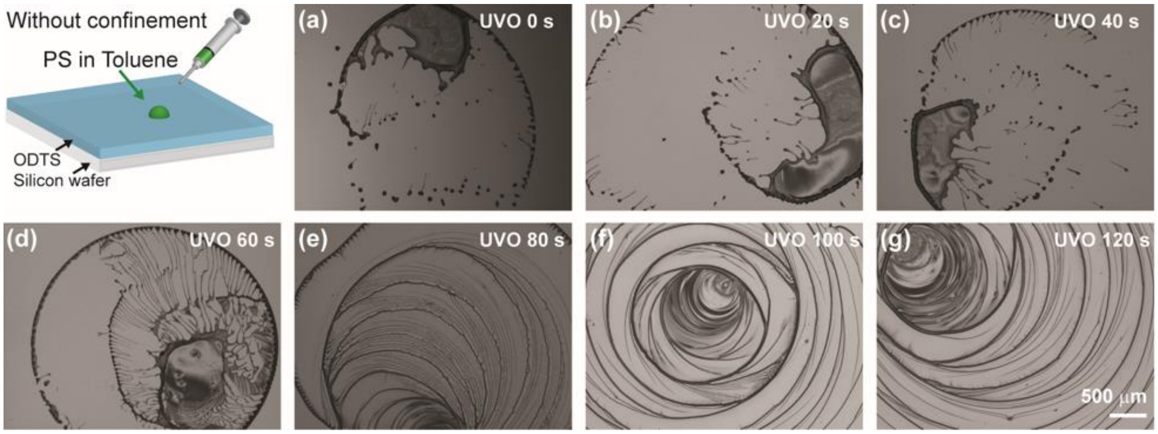

Figure 2.2 – Droplets deposition of polystyrene (PS) in toluene on ODTS modified substrates as a function of UVO time. Schematic illustrates the sessile drop deposition with initial concentration of 0.5 mg/ml and volume of 4 μl. (a) to (g) demonstrates the PS deposition as UVO exposure time increases from 0 s to 120 s.

these structures are created via flow-coating, which introduces controlled "stick-slip" motion into the contact line where PS deposition occurs. Without flow-coating, in a droplet of PS solution for example, vertical stripes are deposited (Figure 2.2d). When depositing droplets of PS solution, without confinement from flow-coating flexible blade, for lower UVO exposure time (0 s to 60 s), the outer ring deposition is obvious. Inside the outer ring, dots with finger tails (0 s to 40 s) or vertical stripes (60 s) are deposited. For higher UVO exposure time (80 s to 120 s), besides the outer ring, a series of rings are deposited on the substrate. As UVO exposure time increases, contact angle of water and toluene decreases, leading to easier wetting and more solute deposition on the substrate.

2.4.2 Solutal Marangoni Flow

To our knowledge, arrays of hyper-branched structures have not previously been obtained via confined evaporative assembly; however, similar periodic patterns have been created by adding surfactant to an evaporative drop containing microshperes[13] on neat silicon wafers. Stebe et al. speculated that Deegan's periodical patterns result from Benard cells, driven by thermal Marangoni stresses[17,20,79]. As the droplet evaporates, the surface of the droplet cools and creates temperature gradients as a function of depth and radius. These temperature gradients create surface tension gradients which induce the thermal Marangoni stresses[80,81]. Besides thermal Marangoni stress, surface tension gradients can also be generated from solute concentration gradient. This effect is referred to as a solutal Marangoni effect. One noteworthy example of solutal Marangoni stresses is "Tears of Wine", in which fluid from an area of lower surface tension is drawn to an area of higher surface tension due to a tension gradient[82,83] (Marangoni force). In our work, friction

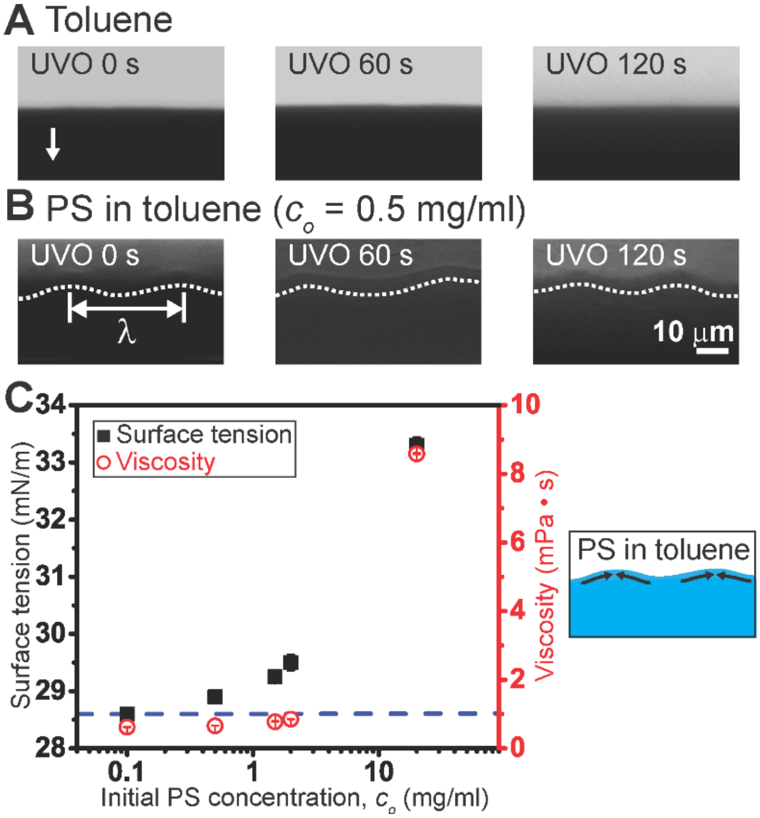

Figure 2.3 – Solutal Marangoni flow induced by solution local concentration difference. (A) Meniscus front of toluene only via flow-coating. The arrow indicates the flow receding direction. (B) Meniscus front of polystyrene (PS) in toluene via flow-coating. The white dash lines are guides to the eye and the meniscus front follows periodic wavelength of λ. (C) Surface tension and viscosity as a function of initial PS concentration. The blue dash line indicates the surface tension of toluene. The schematic illustrates possible flows caused by surface tension gradient (induced by concentration gradient) for PS in toluene at the meniscus evaporating front.

induced by the moving substrate plays the same role as gravity in "Tears of Wine". This friction occurs in the direction of the edge front to the bulk solution[84], a direction that is opposite to that of the Marangoni force in flow-coating. These opposing forces induce the periodic formation of vertical stripes, parallel to the flow direction. Consequently, we speculate that these stripes give rise to hyper-branched structures.

While the thermal Marangoni effect is of minor importance for our process, as illustrated by the stability of the toluene meniscus in the absence of PS in Figure 2.3A, we believe that the solutal Marangoni effects play a large role in the formation of hyper-branched structures (Figure 2.3B). The meniscus fronts, shown in Figure 2.3A and Figure 2.3B, display a straight line for toluene only and a sinusoidal wave for PS in toluene suggesting that the solutal Marangoni effect is more important than the thermal Marangoni effect. The solutal Marangoni effect, which is generated by a concentration gradient induced surface tension gradient, results from the local fluctuation of the concentration[85] of polystyrene (Figure 2.3C).

To quantify the solutal Marangoni effect[86,87], we estimate the Marangoni number (M_a) and Marangoni wavelength (λ).

$$M_a = \left(\frac{d\gamma}{dc}\right)\frac{\Delta c \cdot h}{\eta D} \qquad \text{Equation 2.1}$$

$$\lambda = \frac{2\pi h}{\sqrt{M_a/8}} \qquad \text{Equation 2.2}$$

Here, $\left(d\gamma/dc\right)\cdot\Delta c$ is the surface tension difference caused by concentration gradient, *h* is the size of the gap height beneath the flexible flow coating blade[76], η is the viscosity, and *D* is the diffusion coefficient. The viscosity of the PS in toluene solution increases as the PS concentration increases[88]. The change in surface tension changes corresponding to various levels of initial PS concentration (Figure 2.3C) was measured with the Wilhelmy method using Micro Trough XS (Kibron, Inc.). From this data, we determine $\left(d\gamma/dc\right)\cdot\Delta c$. Also, the changes in viscosity corresponding to various levels of initial PS concentration (Figure 2.3C) was measured, using TA Instruments AR2000 Rheometer with standard concentric cylinders at 20 °C under shear rate 200 s^{-1}. From measured values and the Zimm model, the diffusion constant D is calculated by Equation 2.3.

$$D \cong 0.196\frac{k_B T}{\eta_o R_g} \qquad \text{Equation 2.3}$$

where k_B is the Boltzman constant, T is the experimental temperature, η_o is the viscosity of toluene, and R_g is the radius of gyration of polystyrene (PS) in toluene. Assume T as 20 °C, use η_o as 0.60 mPa· s and R_g as 63 nm, D is calculated to be 2.1 * 10^{-11} m^2/s (comparable to references[89]). Assuming that the solution concentration changes near the evaporating meniscus, we find the Marangoni number to be on the order of 10^5 to 10^6 from Equation 2.1. If we assume the bulk solution region as the initial PS concentration (here c_o = 0.5 mg/ml) and the contact line region (more evaporation yields higher concentration) as 3.0 mg/ml or 20 mg/ml, incorporating the surface tension measurement as a function of concentration in Figure 2.3C, the surface tension difference $\Delta\gamma$ ($\Delta\gamma = \left(\frac{d\gamma}{dc}\right)\Delta c$) is calculated to be 2 mN/m to 4.4 mN/m. For calculating Marangoni number M_a, we assume h as the comparable length scale to the thickness of the flexible blade in flow coating ($h \cong$ 75 μm), and η as the viscosity of 0.5 mg/ml PS in toluene (η = 0.66 mPa· s) or the viscosity of 20 mg/ml PS in toluene (η = 8.59 mPa· s). From these values, the Marangoni number M_a is calculated to be 1.827 * 10^5 to 1.058 * 10^6, which is significant for generating the Marangoni flow. This significant M_a number indicates a major contribution at the meniscus front by the solutal Marangoni effect.

Therefore, the local Marangoni flow (schematic in Figure 2.3C) results in a sinusoidal shape for the meniscus whose wavelength is given by the characteristic wavelength of Marangoni flow. Thus, this Marangoni effect sets the periodicity of the vertical stripes and dots. Although the magnitude of the Marangoni wavelength (from the Marangoni number, we can calculate the characteristic wavelength of Marangoni flow λ (Equation 2.2)) is predicted to be between 1.3 µm and 3.1 µm, which is smaller than measured 30 µm, it remains nearly constant regardless of UVO exposure time. This discrepancy in predicted and measured Marangoni wavelength is most likely due to the unmeasurable increase in viscosity at the evaporating meniscus front[87].

2.4.3 Hyper-branched Structure Formation

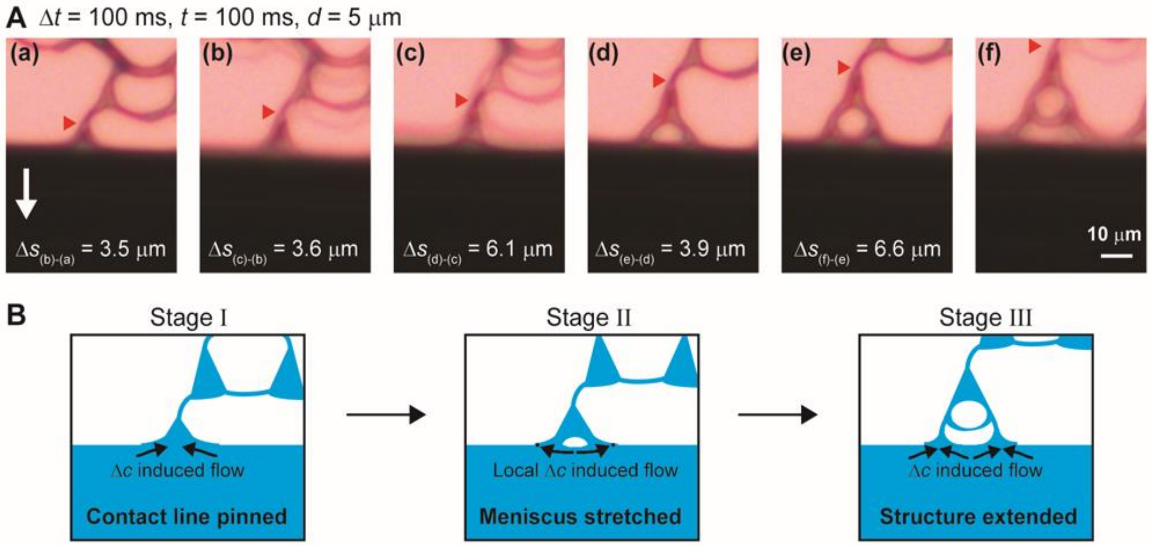

Figure 2.4 – Hyper-branched structure formation. (A) *In-situ* video images of hyper-branched structure formation with stopping time, t = 100 ms and set distance, d = 5 µm. The interval time (Δt) is 100 ms between snapshots, and the step distance (Δs) is measured from the red triangle marker. The white arrow indicates the flow receding direction. (B) Schematic of evolution in hyper-branched structures.

To reveal the details of spontaneous structure formation of hyper-branched structures, we employed *in-situ* microscopy (Figure 2.4A). The video images revealed that hyper-branched structures are generally formed in three stages (Figure 2.4B). In the first stage, fingers parallel to the flow direction appeared as a result of Marangoni instability and friction. Importantly, a triangularly shaped meniscus connects the fingers to the meniscus front. Since the fingers are more highly concentrated with PS than the bulk solution, the surface tension of a finger is relatively higher, drawing in the bulk solution, which has a lower surface tension. This step is shown schematically in Figure 2.4B (a).

In the second stage, one finger divides into two, thereby creating a branch. This division is associated with sufficient thinning of the triangularly shaped meniscus as it is stretched to a length determined by the flow coating set distance. If the set distance is sufficiently small, then thinning does not occur and PS solution continues to feed the vertical stripe. For thinned triangular meniscus, the two edges (two dots in Figure 2.4B stage II) evaporate at a faster rate than other points. Therefore, the edges become more concentrated, increasing the surface tension, which in turn draws in a lower level of solution (curved arrows of flows in Figure 2.4B stage II). The outward flow in the stretched

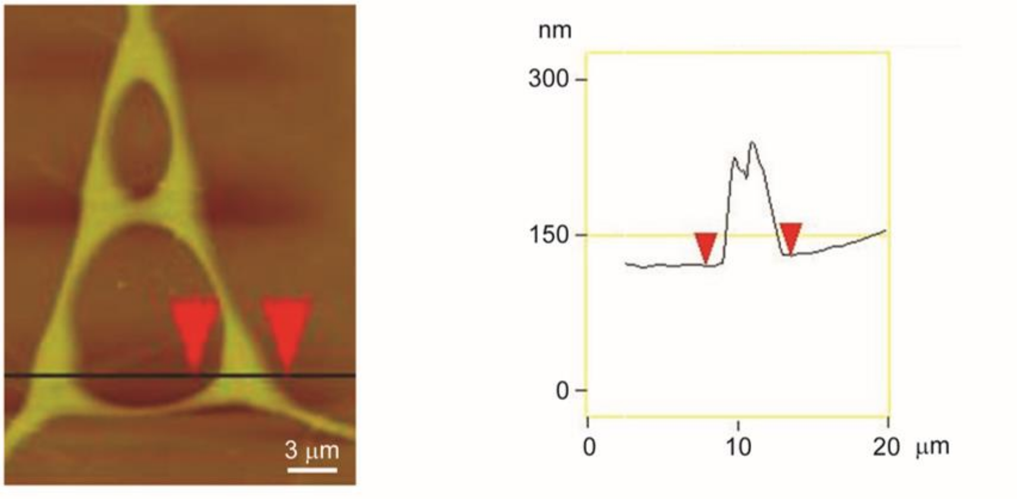

Figure 2.5 – Height profile of the hyper-branched structure characterized by AFM.

triangular meniscus results in a lower height profile in the middle as characterized by atomic force microscopy (Figure 2.5).

The branching continues until the third stage (Figure 2.4B stage III) when the programmed set distance is reached. At this time, the substrate stops moving, and the triangularly shaped meniscus fingers again form, and the process repeats to form an extended hyper-branched structure (same as in Figure 2.4B stage I).

2.4.4 Importance of Set Distance

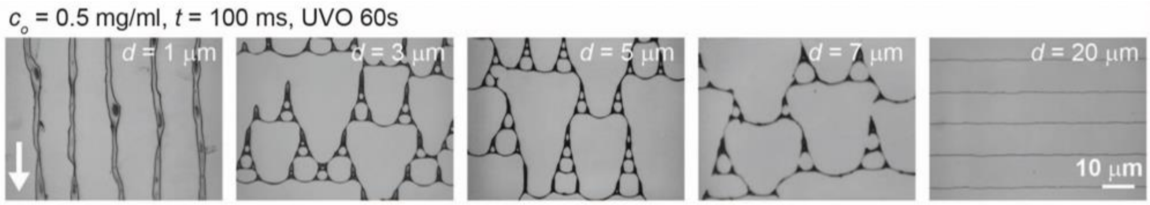

Figure 2.6 - PS patterns as a function of set distance d with constant c_o (c_o = 0.5 mg/ml), t (t = 100 ms) and UVO exposure time (60 s). The white arrow indicates the flow receding direction.

To understand the controlling parameter of the hyper-branch geometry, we examined the effect of set distance d (Figure 2.6), while holding c_o, stopping time, and UVO exposure time constant. When d was small, e.g. d = 1 or 2 μm, vertical stripes parallel to the flow direction were formed. The spacing of these vertical stripes is set by the Marangoni wavelength; however, as the set distance was increased, structures changed from stripes to hyper-branched structures. Furthermore, when d was greater than the slip distance, e.g. d = 20 μm or greater, horizontal lines perpendicular to the flow receding direction were deposited. This transition is associated with the development of a critical stress at the meniscus contact line to cause destabilization. At small d, while the Marangoni flow drives material to the contact line, the blade movement drags the polymer material away from the contact line, and therefore vertical stripes are deposited. When the meniscus is stretched between 3 to 7 µm, hyper-branched structures are formed. For sufficiently large *d*, the meniscus is strongly stretched and destabilized. The concentrated materials at the pinned contact line is deposited and forms a horizontal line, while the other part of the stretched film moves along with the blade.

2.4.5 Solute Deposition

Although surface energy does not influence the Marangoni flow, it does play a role in the deposition of polymer during flow-coating of hyper-branched structures (Figure 2.1C). As reported previously[12,86,90], evaporation is faster when contact angle is lower, thus outward flow of solute is increased, resulting in more deposition. This effect was confirmed in our method by observing the quantity of PS deposited at the initial contact line with controlled stopping time (Figure 2.7A). The quantity of PS adsorption increased as UVO exposure time increased, due to the increased solvent evaporation at lower contact angles for the meniscus.

2.4.6 Importance of Initial Solution Concentration and Stopping Time

To further explore the variables influencing hyper-branched structure formation, we kept the UVO exposure time and set distance, *d*, constant, 60 s and 5 µm respectively, and varied the flow-coating parameters, initial solution concentration, c_o, and stopping time, *t*. Figure 2.7B shows typical morphological features of deposited PS as a function of c_o and *t*. For deposition of the PS solute at the contact line, to some extent, stopping time

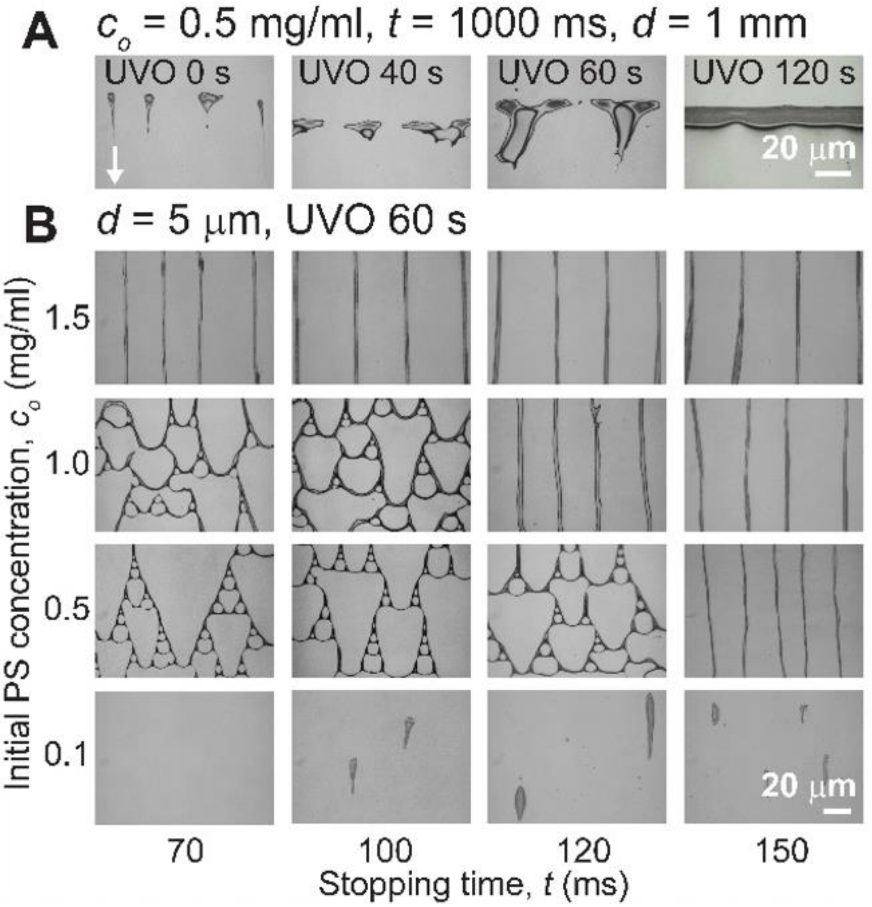

Figure 2.7 – PS pattern formation. (A) PS patterns as a function of UVO exposure time with constant initial PS concentration (c_o = 0.5 mg/ml), stopping time (t = 1000 ms) and set distance (d = 1mm). The white arrow indicates the flow receding direction. (B) PS patterns as functions of c_o and t while keeping constant set distance (d = 5 µm) and UVO exposure time at 60 s.

is equivalent to concentration. Longer stopping times facilitate more evaporation[91], thus creating a more concentrated region at the contact line, compared to shorter stopping times with the same c_o. This similarity was revealed by increasing c_o or by increasing stopping times, show the same transition from hyper-branched structures to vertical stripes. Transitions were achieved by lower c_o with longer stopping times or by shorter stopping times with higher c_o. At low c_o (c_o = 0.1mg/ml), no deposition was observed at shorter stopping times (t = 70 ms), or dots with vertical tails were produced at longer stopping times (t = 100~150 ms). For these lower c_o, it is anticipated that even longer stopping times would be required for sufficient viscosity increases to be achieved for PS deposition. At higher c_o or longer stopping times, more polymer material is available close to the contact line, preventing the destabilization of the stretched meniscus into the branched structure. The periodicity (wavelength) between vertical stripes was determined by the Marangoni instability and the periodicity increased as c_o increased (vertical columns at t = 120 and 150 ms in Figure 2.7B). This increase in periodicity was observed because the viscosity, η, increase (Figure 2.3C demonstrated the η increase as c_o increased) results in a decrease in M_a and an increase in λ (Equation 2.1 and 2.2).

2.5 Conclusion

In this chapter, we utilize flexible blade flow coating to study polymer structure formation on substrates with systematically varied surface energy. We focus on the patterning of polystyrene. We observe a variety of polystyrene structures including dots, hyper-branched patterns, stripes and lines that can be deposited on substrates with a range of wetting properties. The geometry of the hyper-branched structure is affected by the surface energy of substrates (i.e. UVO exposure time), concentration or stopping time, and set distance. The patterns are a result of competition between Marangoni flow and friction in the stretched meniscus created during subsequent oscillations in the programmed flow-coating process. Beyond explaining the formation of these patterns, our findings provide new, fundamental knowledge on the flexible flow-coating method, which is critical for improving and guiding practical implementation of this scalable method for polymer nanostructure fabrication. This may lead to new fabrication methods for creating structurally integrated assemblies.

2.6 Acknowledgements

This work was funded by the Center for Hierarchical Manufacturing (CMMI-1025020) at the University of Massachusetts. We thank NSF MRSEC (NSF DMR-2820506) for facilities support. I would like to thank Professor Cécile Monteux and Dongyun Lee for their fruitful discussions, Professor Cécile Monteux for being an author on my paper from this chapter, Joseph W. Krumpfer and Professor Thomas McCarthy for help in silane surface modification, Lang Chen for help in surface tension measurement, and Jon Pham, Dan King, and Yu-Cheng Chen for proofreading support.

CHAPTER 3

HIERARCHICAL COMPOSITE OF ASSEMBLED NANOPARTICLES AND POLYMERS

3.1 Introduction

In Chapter 2, polymer patterning is assisted by the confined evaporative assembly setup, flow-coating. Previous research on the addition of nanoparticles (NPs) into polymers as nanocomposites has presented advantageous physical properties changes, such as improved adhesion, self-healing capabilities, and different failure mechanisms compared to polymers[92–94]. Additionally, controlling local distribution of NPs can be helpful for nanocomposite properties. Importantly, accomplishing the controlled NPs distribution in the nanocomposite with minimal steps is critical for transferring lab scale technologies to manufacturing. It is necessary to develop fabrication methods that can control the local distribution of NPs within a polymer matrix. This chapter utilizes flow-coating to fabricate nanocomposite with controlled distributions of NPs in a one step process. We create a hierarchical nanocomposite with structured fluctuations in compositional volume fraction of NPs.

Beyond the achievement of one step processing of NPs and polymers, deposition difference of volume fraction of NPs and polymers at the evaporating contact line, yields opportunity to understand the flow competition mechanism of nanometer scale material under confined evaporative assembly. Our findings are significant because previous research on the flow competition of particles is limited to the large size difference of bi-dispersed particles (nm scale particles and µm scale particles) in the drying drop[95,96]. In addition, the fabrication of nanocomposite film with controlled local deposition of NPs provides a model material for exploring structural effect on mechanical properties of thin composite films. In particular, the possibility of forming hierarchical structure (shaped patterns and films) in one step via flow-coating provides preferential segregation of nanoparticle or polymer. This may offer striking properties compared to filming of uniformly distributed nanoparticle and polymer mixture.

3.2 Approach

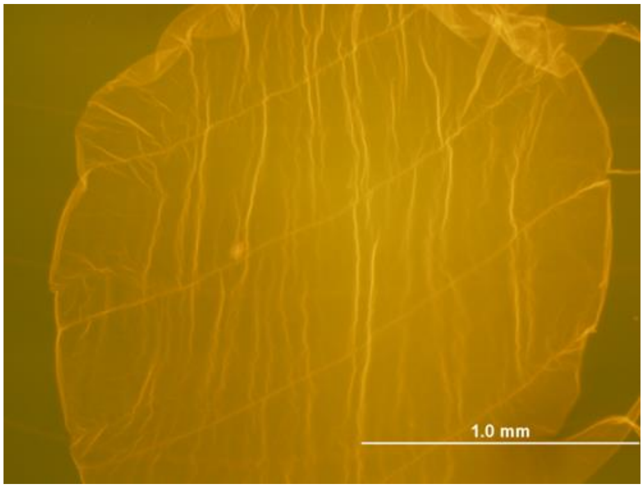

Figure 3.1 Free-standing nanocomposite films of NPs and PMMA in water under fluorescent microscope.

The hierarchical nanocomposite materials are fabricated by flow-coating (Figure 3.1). In this method[9], an angled razor blade is first positioned on top of the substrate (Figure 3.2A), then a dilute solution of a mixture of NPs and poly(methyl methacrylate) (PMMA) homo-polymer in toluene, is injected between the blade and substrate. Next, the substrate is translated in a periodic fashion including programmed velocity step functions, the set distance (*d*) between stopped positions, and the time in the stopped positions (stopping time, *t*) (Figure 3.2B). When the substrate moves with a programmed velocity (*v*), the solution is sheared and a film is formed until the set distance (*d*) is reached. When the substrate stops with a programmed stopping time (*t*), solutes are transported to the three-

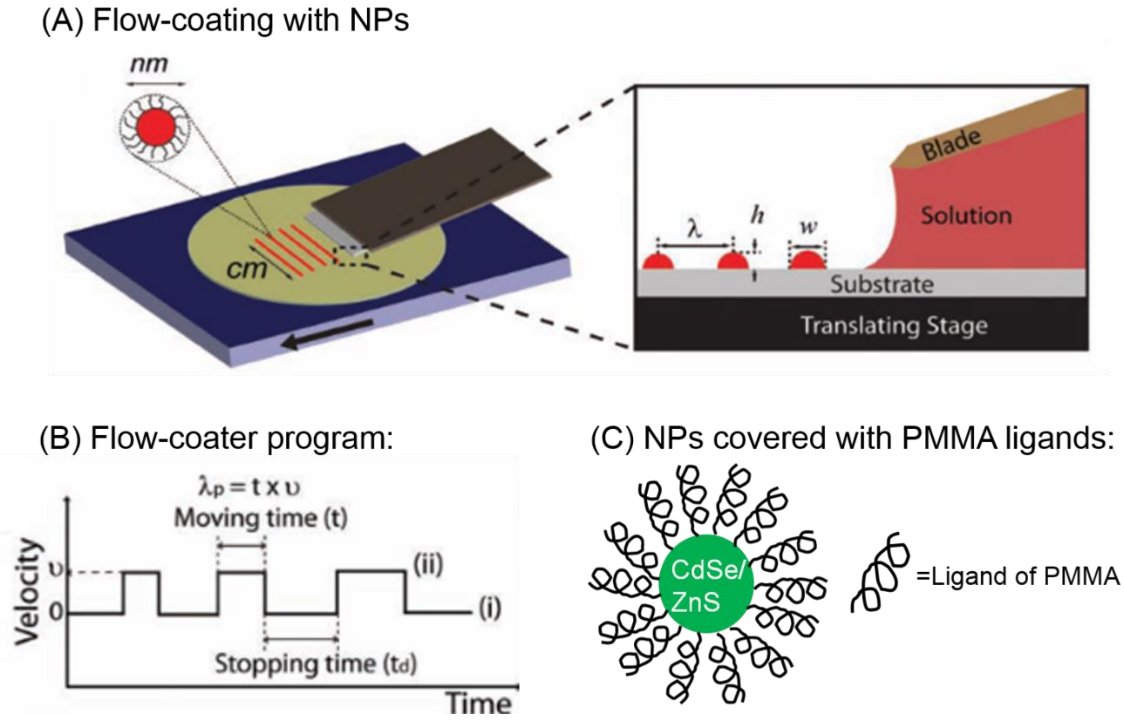

Figure 3.2 – Razor blade flow-coating to form nanocomposite. (A) Schematic of Flow-coater for fabricating nanoparticle (NP) lines on substrates. (B) The velocity profile of the flow-coater[9]. (Reprinted with permission from Kim, H.; Lee, C.; Sudeep, P.; Emrick, T.; Crosby, A. J. Nanoparticle Stripes, Grids, and Ribbons Produced by Flow Coating. *Adv. Mater*. **2010**, *22*, 4600–4604.) (C) NPs used in this chapter functionalized with poly(methyl methacrylate) (PMMA) ligands.

phase contact line to deposit at an increased rate due to increased evaporation rates, similar to the coffee-ring phenomenon[97]. At each stop of the substrate, the solute deposition forms a line with a triangularly shaped height profile (Figure 3.6B), which maximum height is higher than the film. As the programmed velocity step function alternates with move and stop, hierarchical composites form with structures of film and line alternatively.

3.3 Experimental

3.3.1 Materials

The NPs were synthesized to have a core-shell structure, where a cadmium selenide (CdSe) core transitioned to a zinc sulfide (ZnS) shell (the weight percent of CdSe and ZnS in the NP without ligand was approximately 50wt% and 50 wt%) and PMMA ligands were grafted to the outer surface (Figure 3.2C). These PMMA ligands functionalized NPs were synthesized by Jimmy Lawrence from Professor Todd Emrick group in the same Department at UMASS. The PMMA ligand coverage of NPs was 84 wt% characterized by

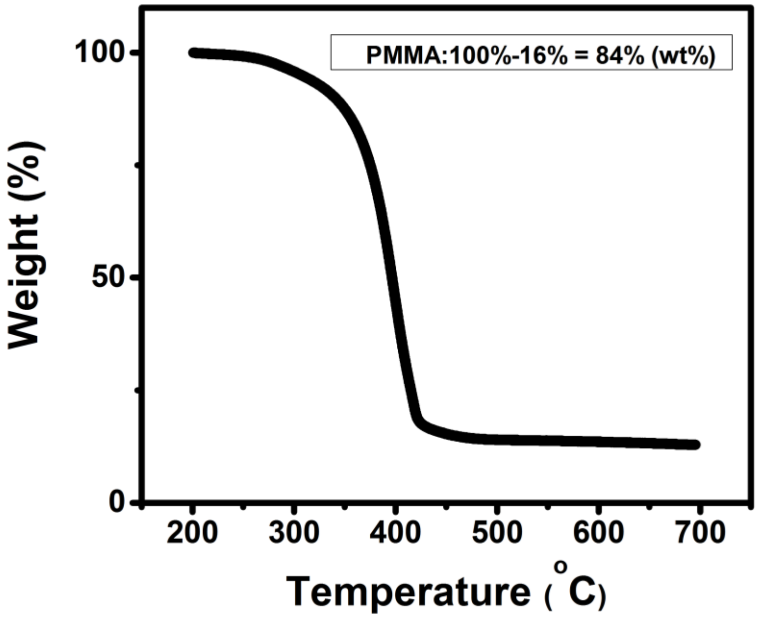

Figure 3.3 – Thermogravimetric analysis (TGA) of PMMA ligands functionalized NPs.

thermogravimetric analysis (TGA, TGA 2950, TA instruments) (Figure 3.3).

For the mixture solution preparation, poly (methyl methacrylate) (PMMA) (M_w = 1,540kg/mol, PDI = 1.4, Polymer Source) was initially dissolved in toluene. Next, quantum dots NPs (8~10 nm in diameter without ligands, characterized by transmission electron microscopy) functionalized with PMMA ligands (M_w = 15~30kg/mol) were added to the solution. The ligands (PMMA) were chosen to be the same with the homo-polymer (PMMA).

3.3.2 Nanocomposite Film Fabrication

In the tested samples in this chapter, the mixing solution contained 2 mg/ml NPs and 2 mg/ml PMMA (homo-polymer) in toluene (the concentration was the measured solute weight relative to the solvent volume). If the solvent evaporated fully, this mixing solute yielded 50 wt % NPs and 50 wt% homo-polymer PMMA.

In this chapter for nanocomposite films with hierarchal patterns, the flow-coating parameters were set as 1 mm/s for the programmed velocity (*v*), 30 µm for the set distance (*d*), and 1 s for the stopping time (*t*).

3.3.3 Substrate Preparation

Polished silicon wafer (100 mm diameter, ~ 500 µm thickness, 100 orientation, P/B doped, University Wafers) substrates (typically cut into 3 cm x 4 cm) were first cleaned by sonication in soap water, acetone, toluene and isopropanol for 15 minutes respectively. After sonication, substrates were dried under nitrogen and exposed to UV-Ozone (Jelight 342 UVO system) for 30 minutes. Then nanocomposite films were flow-coated on top of PAA.

For releasing nanocomposite films, sacrificial layer of filtered 1 wt% polyacarylic acid (PAA) (M_w=1800 g/mol, Aldrich) in water solution was spin-coated onto clean substrates before flow-coating. When releasing the nanocomposite film, film was usually cut into rectangular shape and water was added along edges of the film.

3.3.4 Characterization

Fluorescent images of the nanocomposites were captured by a reflection fluorescent microscope (Olympus BX51 with a CCD camera and a 100 W Mercury arc lamp). Transmission electron microscope (TEM) images were obtained by Joel JEM-2000FX. Atomic force microscope (AFM) images were carried out in tapping mode with Nanoscope III (Digital Instrument Co). Oxidation analysis of the nanocomposite was examined by X-ray photoelectron spectroscopy (XPS) using a Quantum 2000 scanning ESCA microprobe

(Physical Electronics, Inc.). Chemical analysis of nanocomposite films on silicon wafers were conducted by scanning electron microscope (SEM) equipped with energy dispersive spectrometer (EDS) at 5 kV and 50 pA.

3.4 Results and Discussion

3.4.1 Films Formation in the Nanocomposite

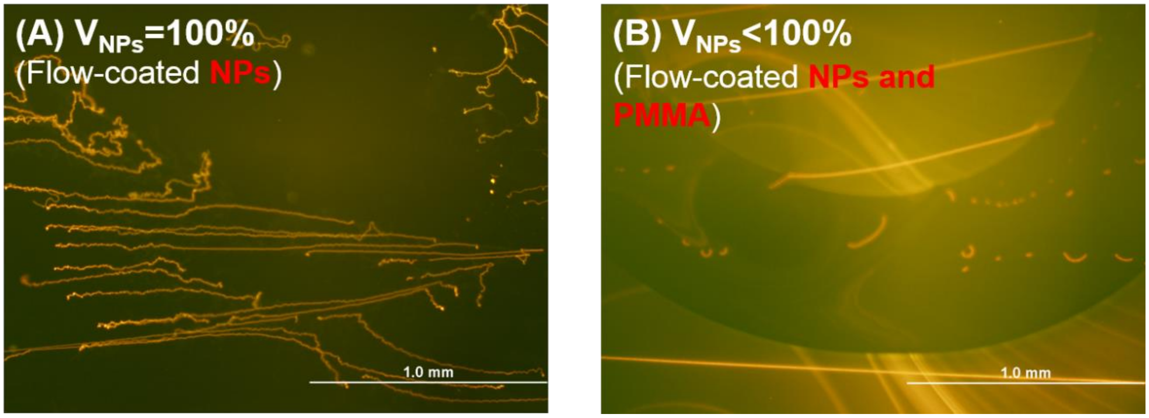

Figure 3.4 – Nanocomposite film formation. Upon releasing flow-coated patterns into water (fluorescent images): (A) without homo-polymer PMMA (volume fraction of NPs in the flow-coated pattern, V_{NPs} = 100%), no nanocomposite film was formed; (B) with addition of homo-polymer PMMA ($V_{NPs} < 100\%$), nanocomposite film was formed.

In previous work of flow-coating individual solutions of polymers or nanoparticles [9,10], only lines are formed, without films between the lines. Upon releasing, these lines would be floating separately. However, in this chapter, when flow-coating mixed solutions of NPs and polymers, the hierarchical structures of lines and films are formed (Figure 3.4B). We noticed the higher concentration of our NPs (2 mg/ml) and polymers (2 mg/ml) mixture solution compared to the previous work (0.1 mg/ml of NPs or polymers)[9,10]. To investigate whether the hierarchical structures are formed because of the high concentration of solute, we flow-coated the 2 mg/ml NPs solution, and the 2 mg/ml polymer solution separately. For the 2 mg/ml NPs, only lines are formed as lines are floating separately upon releasing (Figure 3.4A). For the 2 mg/ml PMMA solution, hierarchical structures of lines and films are formed (Figure 3.5B). These results suggest that PMMA induces the formation of films between lines. To further verify the concentration effect of PMMA in the hierarchical formation, we flow-coated PMMA solutions (without NPs) at different concentrations (Figure 3.5), smaller and greater than the overlap concentration of PMMA (c*). Overlap concentration of PMMA (c*, Equation 3.1) is the critical point for polymers to overlap and entangle in the solution. In our case, our PMMA molecular weight is greater than the entanglement molecular weight (M_e) of PMMA (M_e=27.5 kg/mol[98,99]), which also facilitates overlapping and entanglements.

$$c^* = \frac{M_W / N_{AV}}{\frac{4}{3}\pi R_g^{\ 3}} \qquad \text{Equation 3.1}$$

where N_{AV} is the Avogadro's number and R_g is the radius of gyration of the polymer chain.

When the concentration of PMMA is smaller than 2 mg/ml, no film is formed between lines (Figure 3.5A). When the concentration is greater than 2 mg/ml, films are formed between the lines and the nanocomposite film releases as one coherent unit (Figure 3.5C). As the critical concentration of PMMA (2 mg/ml) for the hierarchical structure formation is close to the overlap concentration of PMMA (c* = 1.7 mg/ml here), we propose that the formation of films between lines are determined by the overlap concentration of PMMA (c*).

3.4.2 Depositions of NPs or Polymers in the Nanocomposite

In the hierarchical nanocomposite of NPs and polymers, the hierachical structures consisit of lines and films. As demonstrated by the last section that films between the lines are formed by the PMMA polymer, we would expect most polymers to be deposited in the films, then most NPs would be deposited in the lines. The NPs deposition is demonstrated by the fluorescent light intensity, as fluorscent intensity of NPs that deposit in the line is greater than in the film with the same projected area (Figure 3.6A). TEM also demonstrates that the greater number of NPs is deposited at the line than at the film by black and white contrast (Figure 3.6C). At the line region, the substrate stops moving and the contact line pins. This pinning faciliates outward flows of NPs and polymers to replenish the evaporation at the contact line. Previous work of mixture solutions of small particles (~ 100 nm) and large particles (~ 1 µm) in an evaporating droplet demonstrate that smaller particles tend to move closer to the contact line as larger particles are obstructed by the liquid meniscus[96,100]. Here, the size of NPs is 8 to 10 nm in diameter, while the R_g of PMMA (M_W = 1,540kg/mol) is estimated to be 33 nm[101]. However, whether we can directly utilize the size difference between NPs and polymers to explain the distribution difference between the lines and the films in the nanocomposite needs further investigation. Our

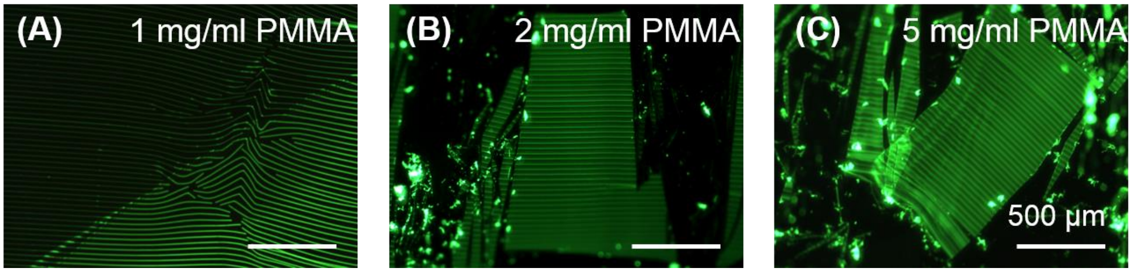

Figure 3.5 – Fluorescent images of flow-coated PMMA patterns at different concentrations upon releasing into water. Fluorescent dye (Coumarin 153, Aldrich) was added into the solution for image purposes. (A) 1 mg/ml PMMA. (B) 2 mg/ml PMMA. (C) 5 mg/ml PMMA.

polymers are not solid particles and the size difference between NPs and polymers is much smaller than previous work.

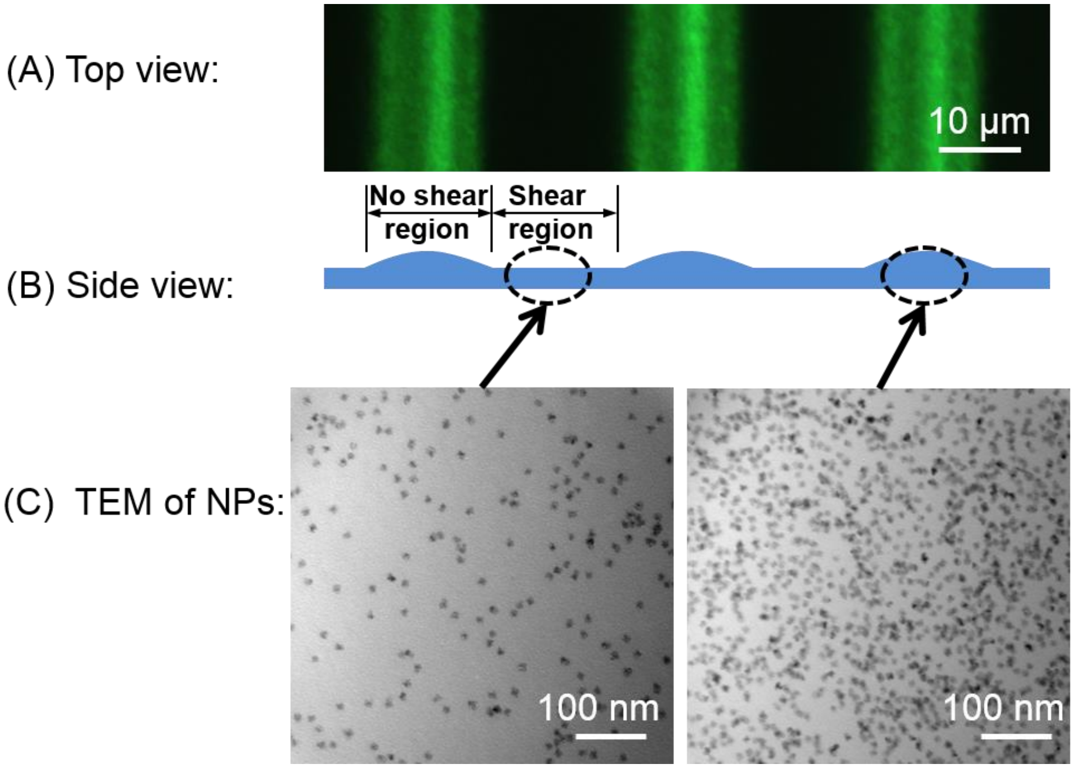

Figure 3.6 – NPs deposited at different regions in the nanocomposite. (A) Top view: fluorescent images of the nanocomposite. (B) Side view: schematic of the hierarchical pattern: lines (no shear region) and films (shear region). (C) TEM of NPs at different regions in the nanocomposite.

3.4.3 Local Volume Fraction of NPs at the Film Region

As the hierarchical nanocomposite does not have a uniform thickness (the average thickness of the line region is higher than that of the film region), the number of NPs cannot represent relative distribution of NPs to polymers in the line or the film. We should consider the thickness and geometry difference between lines and films, and utilize the local volume fraction of NPs at the line and the film instead of the number of NPs. However, as several layers of NPs stack on each other at the line region, conventional TEM cannot be utilized for determining volume fraction of NPs at the line region.

At the film region of the hierarchial nanocomposite, we can utilize conventional TEM to determine the NPs local distribution, as the thickness is uniform and NPs are usually deposited by one layer without stacking NPs.

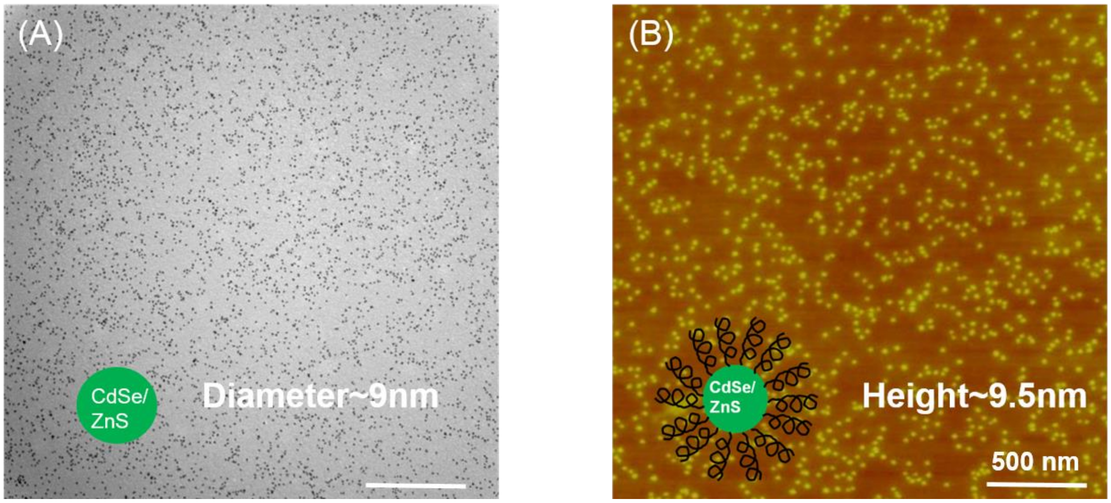

Figure 3.7 – Size of NPs. (A) TEM: average diameter of the NP without ligand is 9 nm. (B) AFM: average diameter of the NP with ligand is 9.5 nm.

From the TEM image (Figure 3.6C), we can estimate the local volume fraction of NPs without ligands in the film region ($V_{film,\,NPs}$) using Equation 3.2.

$$V_{Film,\mathrm{NPs}} = \frac{N_{NPs}\left(\frac{4}{3}R_{NPs}{}^{3}\right)}{W_{Film}L\;H_{Film}} = \frac{W_{Film}L\;\boldsymbol{\varphi}_{\mathbf{AREA}}\left(\frac{4}{3}R_{\mathrm{NPs}}\right)}{W_{Film}L\;H_{Film}} \qquad \text{Equation 3.2}$$

where N_{NPs} is the number of NPs in the film region, W_{Film} is the width of the film region, L is the length of the film, H_{Film} is the thickness of the film region (Figure 3.8), $\boldsymbol{\varphi}_{\mathbf{AREA}}$ is the

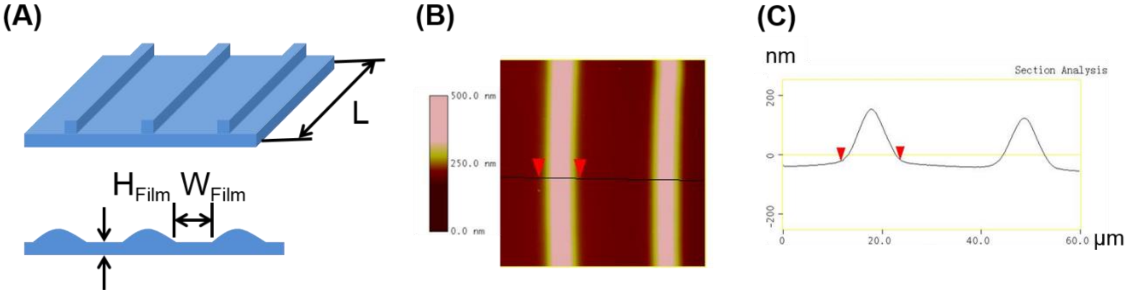

Figure 3.8 – Thickness profile of hierarchical nanocomposite. (A) Schematic. (B) AFM height image. (C) Height profile of the cross-section line in (B).

area fraction of NPs (obtained from TEM), and R_{NPs} is the radius of the NP (obtained from TEM and AFM) (Figure 3.7).

From Equation 3.2, we estimate the volume fraction of NPs without ligands in the film region to be 0.91%. How is this value compared to the volume fraction of NPs in the mixed solute (when solvents evaporate fully in the solution)? As we know the weight fraction of NPs with ligands is 50 wt% in the mixed solute, incoporating the weight fraction of core-shell in the NP without ligands from TGA, and considering the density of ZnS (4.09 g/cm^3), CdSe (5.82 g/cm^3), and PMMA (1.18 g/cm^3), we can estimate the volume fraction of NPs without PMMA ligands in the mixed solute to be 2%.

The volume fraction of NPs decreases slightly from 2% in the solute to 0.91% in the film region. This decrease suggests a NPs volume fraction increase in the line region.

3.4.4 Local Volume Fraction of NPs at the Line Region

3.4.4.1 High Temperature Oven to Decompose Polymers

To obtain estimations of local volume fractions in the line region, flow-coated hierarchical nanocomposites on a silicon wafer are placed in 450 °C oven for 12 hours. TGA demonstrates that PMMA (M_w = 996 kg/mol) degrades completely at 400 °C[102]. Thus

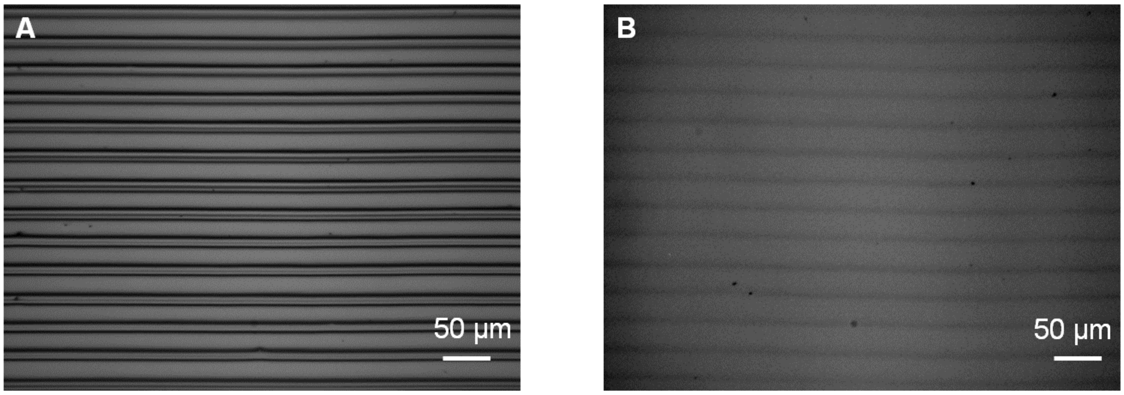

Figure 3.9 - Optical micrographs of hierarchical nanocomposite patterns. (A) Before heating in 450 °C oven. (B) After heating in 450 °C oven.

Figure 3.10 – AFM height images of a line in the nanocomposite. (A) Before the 450 °C heating. (B) After the 450 °C heating.

after heating at 450 °C, homo-polymer PMMA and ligands of PMMA are depleted. The melting point of nanoparticles (a core of CdSe with a gradient shell of ZnS) is over 1000 °C, therefore these inorganic nanoparticles will remain after baking at 450 °C. The loss of organic materials and the remaining inorganic materials are displayed by optical images before and after heating (Figure 3.9). To calculate the local volume fraction of NPs, dimension profiles of the line region are characterized with AFM before and after baking (Figure 3.10). Under the assumption that the highest volume fraction of NPs is calculated after baking and the cross-sectional area equals to $\frac{1}{2}WH$ (where W is the width of the line and H is the maximum height of the line), we estimate volume fractions of nanoparticles in the line and in the film as:

$$\phi_{NP,L} = \frac{\frac{1}{2}W_{2,L}H_{2,L}L}{\frac{1}{2}W_{1,L}H_{1,L}L} = \frac{W_{2,L}H_{2,L}}{W_{1,L}H_{1,L}} \qquad \text{Equation 3.3}$$

$$\phi_{NP,F} = \frac{W_F H_{2,F}\phi_{AREA}L}{W_F H_{1,F}L} = \frac{H_{2,F}\phi_{AREA}}{H_{1,F}} \qquad \text{Equation 3.4}$$

where $W_{2,L}$ and $H_{2,L}$ are parameters after heating at the line, $W_{1,L}$ and $H_{1,L}$ are parameters before heating at the line, $H_{2,F}$ and $H_{1,F}$ are parameters after and before heating respectively at the film, and ϕ_{AREA} is the area fraction of NPs after heating at the film. From Equation

3.3 and 3.4, we estimate the volume fraction of NPs in the line to be 15.8% and in the film to be 0.5%.

While heating causes decomposition of organic materials, it could also result in chemical changes to the NP chemistry. We can utilize XPS to demonstrate whether chemical content of NP has changed. At 75° take off angle in XPS, the atomic oxygen content of NPs increases 15.5% after baking. For the control sample of bare silicon wafer at the same take off angle, after baking, the atomic oxygen content only increases 9.4%.

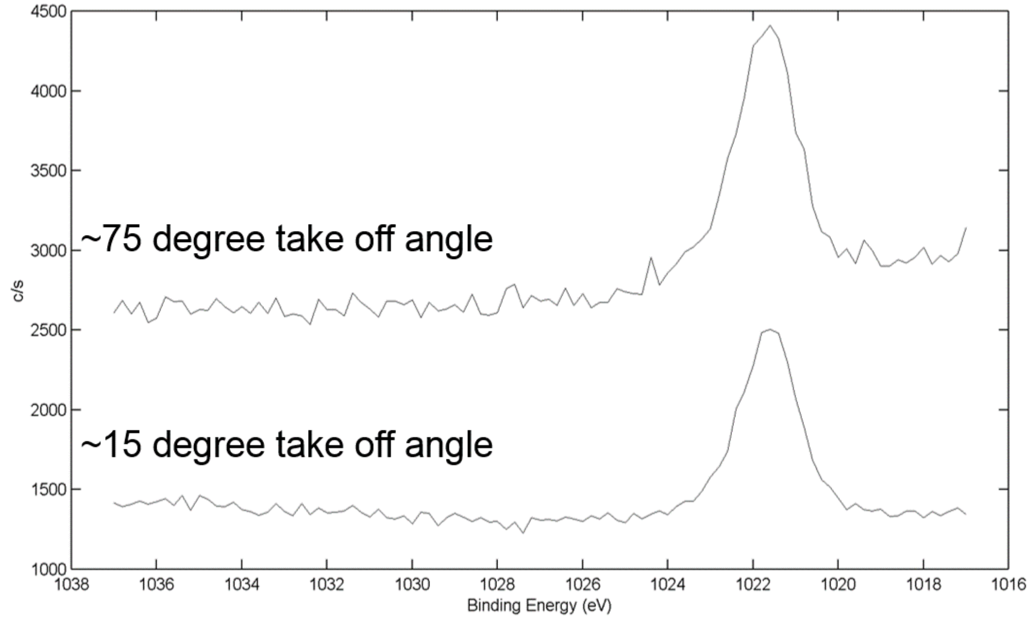

Figure 3.11 – XPS spectrum of NPs on silicon wafers after heating in 450 °C oven for 12 hours. The spectrum demonstrates 1 eV shift in Zn peak from both take off angles.

This 6.1% oxygen increase in the NP compared to bare silicon wafer control indicates the occurrence of oxidation in the NP. In addition, the zinc (Zn) peak shift of 1 eV after the baking indicates the oxidation of Zn (Figure 3.11). The XPS results suggest that in addition to the organic component removal in the high temperature furnace. This oxidation of NPs would possibly change the size of NPs. Thus we cannot use the high temperature oven method to determine local volume fraction of NPs in the line.

3.4.4.2 Energy Filtered TEM Imaging (Future Plans)

The ability of energy-filtered transmission electron microscopy (EFTEM) to distinguish between elements based on in-elastically scattered electrons and its ability to determine composition as well as sample thickness through Electron Energy Loss Spectroscopy (EELS) will greatly improve our understanding of the distribution of polymers to nanoparticles (NPs) in the nanocomposite, specifically at areas with or without shear flows.

The thickness variations of areas under shear (the film region) and no shear (the line region) is taken into account by Electron Energy Loss Spectroscopy (EELS) in the EFTEM, and its ability to determine relative ratio of elements, such as carbon (C) to zinc (Zn), can assist calculations of local volume fractions at different areas. We suggest use a 300 kV source since one of our polymers (PMMA) is known to be quite electron beam sensitive and higher acceleration voltages should induce less beam damage due to the

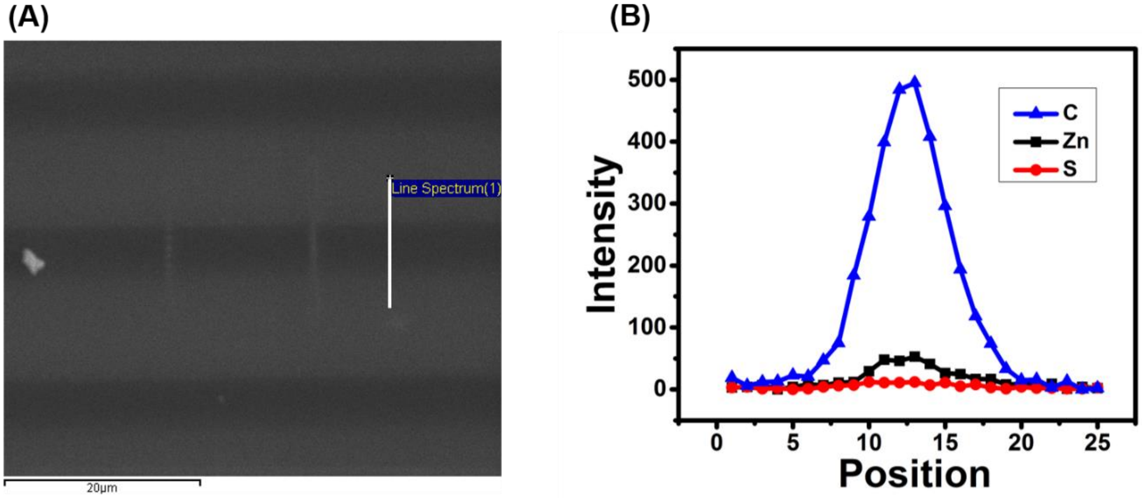

Figure 3.12 – Intensity difference of components in the nanocomposite using SEM-EDS. (A) SEM image of the nanocomposite with darker region representing lines in the nanocomposite. The white line indicates the line spectrum scanned by EDS. (B) Atomic component intensity profile of carbon (C, blue solid triangles), zinc (Zn, black solid rectangles) and sulfur (S, red solid circles) of the line scanning by EDS. Distance between neighboring positions is 560 nm.

longer mean free path. If a cryo sample holder is available, freezing the sample to liquid nitrogen temperature will stabilize the sample as well. The sample could be frozen once in the microscope (no cryo-transfer needed).

To verify whether EFTEM can be used to detect the element difference between lines and films, we apply a line spectrum scanning of the hierarchical nanocomposite pattern using SEM-EDS across the line and the film region (Figure 3.12). As SEM characterizes the sample surface without including all the information from underlying layers, we cannot use SEM-EDS to determine the local volume fraction of NPs. In addition, the intensity profile of atomic component from EDS can only be compared within the same atomic component but not others.

As the polymer PMMA is enriched with carbon (C) and the NP surface is enriched with zinc (Zn) and Sulfur (S), we characterize the content of C, Zn and S using SEM-EDS. The SEM line scanning from position 0 to 25 goes through the film region, the line region and the film region in the nanocomposite. The intensity difference of C or Zn between the film region and the line region demonstrates the feasibility of EFTEM for determining the local volume fraction of NPs or homo-polymer PMMA. EFTEM will be conducted in the future for determining local volume fraction of NPs and PMMA in the nanocomposite.

3.4.5 Molecular Weight Effect of Homo-polymer on Distribution of NPs (Future Plans)

We predict that the local volume fraction of NPs can be altered by changing molecular weight (M.W.) of homo-polymers in the nanocomposite. In mixtures of nanometer scale nanoparticles and nanometer scale polymers, conformational entropy of the polymer chains dominate the nanoparticle distribution. This entropy term can be varied through controlling the relative size of the polymer to the size of the nanoparticle[94,103,104]. By changing the M.W. of homo-polymers from greater than that of the polymer ligand of NP to smaller, the local volume fraction change in the same region can provide insight into our hypothesis whether entropic interactions control the relative deposition of NPs in the polymer matrix.

3.5 Conclusions

The results shown here demonstrate a one-step method to fabricate a hierarchical nanocomposite system of NPs and polymers. Future experiments with EFTEM can help to answer the question of local volume fraction of NPs at different regions in the nanocomposite. This study will be important in the nanocomposite field, as understanding how entropic interactions of polymers to NPs controlling the relative deposition of NPs. Importantly, the ability to create hierarchical nanocomposites over large length scales (on the order of centimeter) and the ability to release the hierarchical nanocomposite film open up new opportunities for biological applications and nanotechnology applications. It can provide platform of nanometer topography and stiffness stimulations to direct cells in biological applications[105,106]. It can also enable direct performance characterization of thin nanocomposite film to understand structural effects on mechanical properties of hierarchical nanocomposite thin films. One of our ultimate goals is to directly characterize mechanical properties of hierarchical nanocomposite thin film. In the following chapter, we develop a new method to characterize mechanical properties of thin films and demonstrate its ability to characterize thin films with uniform thicknesses, which serves as the stepping stone for the hierarchical nanocomposite characterization.

3.6 Acknowledgements

This work was funded by the Center for Hierarchical Manufacturing (CMMI-1025020) at the University of Massachusetts. We thank NSF MRSEC (NSF DMR-2820506) for facilities support. I would like to thank Alexander Ribbe for fruitful discussions and help with SEM, Laju Bu for help with TEM, Jack Hirsch for help with XPS, and Jon Pham and Dan King for proofreading support.

CHAPTER 4

CHARACTERIZATION OF ULTRA-THIN POLYMER FILM MECHANICAL PROPERTIES

4.1 Introduction

Robust, predictable thin polymeric films provide a key mechanical element to a variety of applications, including packaging, electronics and separators[107–110]. However, as film thicknesses decrease, we anticipate deviations from the mechanical properties encountered in bulk. For example, when the film thickness is comparable to the polymer chain length, the dimension of film starts to confine chain conformations, resulting in altered material properties. Previous studies proposed that this nanoconfinement effect on the decrease in the glass transition temperature T_g[41,43,44,62,64] and the viscosity[48] can be explained by enhanced surface mobility theory[41,43,44,48,62,64,111] of ultrathin polymer films. Secondary measurements of ultrathin polymer films also suggested that mechanical property changes including modulus decrease[50] and onset of yield strain increase[53] can correlate to the mobility theory. However, these few existing techniques for mechanical properties dependence on ultrathin film thicknesses are indirect measurements, both based on buckling instabilities[50,53]. Whether mechanical properties of ultrathin polymer films can be directly characterized and correlate with the increased surface mobility remains an open and challenging question.

Furthermore, although the nonlinear mechanical behavior (for example, high mechanical strength and shock resistance) of ultrathin films find practical uses in gas barrier films[107], flexible electronic sheets[108,109] and battery separator membranes[110], efforts to characterize mechanical properties beyond the small strain, linear elastic regime have been limited[53,56]. Most characterization methods can only report a Young's modulus[50–52,55,112]. However, the nonlinear regime of a material's stress-strain response is both central to understanding its failure and often related to microstructural changes[113–115]. In thin films this regime has not been discussed due to the inherent difficulty of manipulating fragile, ultrathin polymer films into traditional tensile testing setups.

Imagine attempting to stretch and measure an ultrathin film with a thickness 10,000 times thinner than regular copy paper. The fragile ultrathin film will be easily crumpled[116] and hardly maintain its integrity[117]. Conventional tensile testing equipment lacks the ability

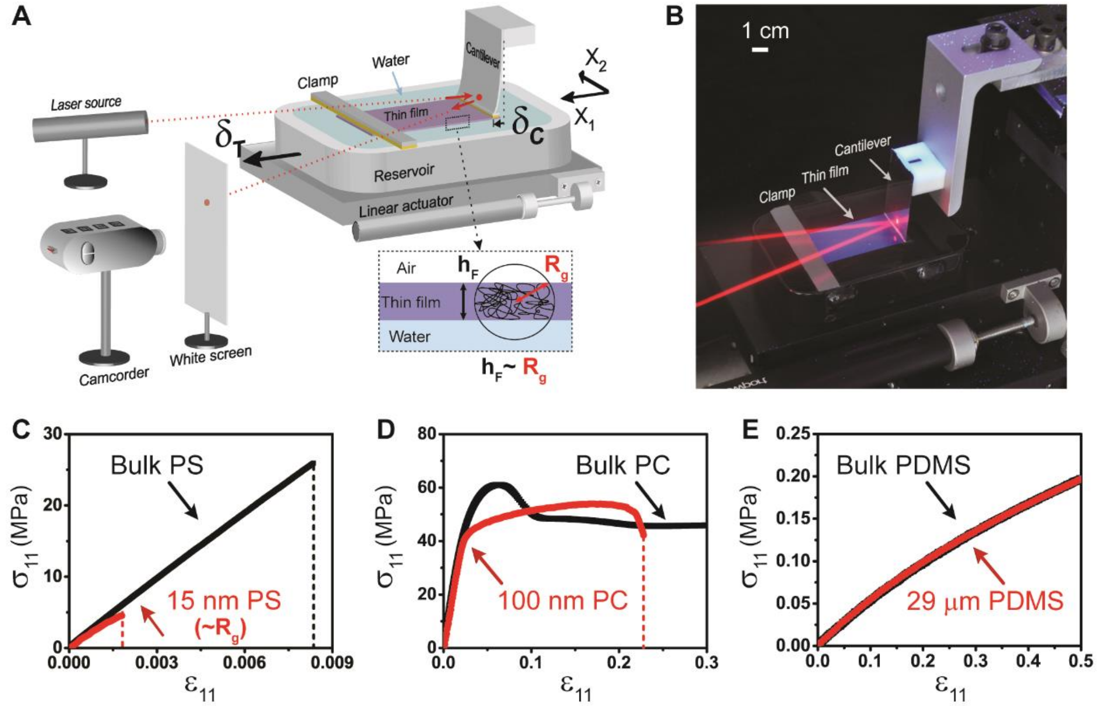

Figure 4.1 - Ultrathin Film Tensile-tester (UFT) and representative stress-strain responses at room temperature. (A) A schematic of UFT for ultrathin films. The capable testing film thickness h_F is comparable to polymer chain radius of gyration R_g. (B) Rectangular thin film of PDMS (9 μm in thickness, 2.2 cm in width, and 4 cm in length) on UFT. The image is taken under UV light and fluorescent dye (Coumarin 153) is added into the PDMS. (C to E) Different material stress-strain responses of thin films (red circles) versus their bulk counterparts (black squares). Thin films are characterized by UFT and their bulk counterparts are characterized by traditional tensile testers. (C) Brittle PS. (D) Ductile PC. (E) Rubbery PDMS.

to mount ultrathin films and typically fall short of the necessary resolution in force[55]. Here, we report a solution to these challenges using an in-house Ultra-thin Film Tensile-tester (UFT) (Figure 4.1A-B) capable of quantifying the full mechanical response of ultrathin polymer films under uniaxial tension (Figure 4.1C-E). This method stretches ultrathin polymer films as they rest stabilized on a water surface[69]. The films themselves average a two-dimensional macroscale size (~ cm^2) while still maintaining nanoscale thickness. Because the elastic stretching energy dominates over the surface energy effects, this setup enables characterization of the uniaxial stress-strain relationship in a variety of materials.

4.2 Approach

We developed an in-house ultra-thin Film Tensile-tester (UFT), where thin films are placed on a water surface and their full mechanical responses are quantified under uniaxial tension. UFT (schematic in Figure 4.1A and real apparatus in Figure 4.1B) utilizes the laser reflection from a displacing cantilever for force sensing (resolution ~10 μN) and a linear actuator for applying displacement (resolution, ~48 nm). To mount the film into the tester, water is used to release the spincast film from the substrate, leaving the film floating on the water surface. Thereafter, the film is raised into contact with two boundaries that act as a clamp and a cantilever. The surfaces of these boundaries are both coated with polystyrene (PS) to ensure sufficient adhesion between the boundaries and the film. First, one end of the film is attached to the fixed clamp moved simultaneously with the linear actuator, then the other end is attached to the stationary cantilever. As the reservoir and the fixed clamp (Si wafer) translate a total displacement δ_T at constant velocity, the film is stretched. Fixed strain rates were used (PS: 0.0033 s^{-1}, PC and PDMS: 0.0025 s^{-1}). Movement of the laser dot, reflected from the cantilever (Aluminum coated cover glass) determines deflection of the cantilever, δ_C, which translates to an applied load, P_F. We correlate laser dot movement in pixels to δ_C and P_F by calibrating the cantilever with both known displacements and standard weights. The displacement in the film, δ_F, is then calculated from subtracting the cantilever displacement from the total displacement (Equation 4.1).

$$\delta_F = \delta_T - \delta_C \qquad \text{Equation 4.1}$$

From δ_F, the strain in the 11 direction ε_{11} is determined by

$$\varepsilon_{11} = \delta_F / L_F \qquad \text{Equation 4.2}$$

where L_F is the film length before stretching. The nominal stress in the 11 direction σ_{11} is determined by

$$\sigma_{11} = P_F / \left(W_F h_F \right) \qquad \text{Equation 4.3}$$

where W_F is the initial film width and h_F is the initial film thickness.

4.3 Experimental

4.3.1 Materials

We demonstrate the UFT's ability to characterize full mechanical responses of ultrathin polymer films using three different materials at room temperature (Figure 4.1C-E): brittle PS (Polymer source, weight-average molecular weight M_W = 136,500 g/mol, polydispersity index (PDI) = 1.05), ductile polycarbonate (PC) (G.E., Lexan sheet, grade 103) and rubbery polydimethylsiloxane (PDMS, mix ratio 20 : 1) (Dow Corning, Sylgard 184^{TM}). By selecting an appropriate cantilever bending stiffness, the UFT is capable of measuring a wide range of moduli (in this chapter, 0.3 MPa to 4 GPa). Solutions of PS in toluene, solutions of PC in dichloromethane, or PDMS were spincast onto sacrificial layer of polyacrylic acid coated substrates (glass or Si wafers) to prepare the films. PS and PC samples were used immediately after spin-coating and PDMS samples were cross-linked at 70 °C without vacuum for 18 hours. W_F and L_F were 22 mm and 30 mm (PS) or 22 mm and 40 mm (PC and PDMS), respectively, after film release and attachment to the UFT boundaries.

The bulk counterparts of thin films (note: PS bulk was prepared from Aldrich, M_W = 350,000 g/mol, PDI = 1.7 by melt press at 175 °C for 40 minutes; PDMS bulk was prepared by cross-linking at 70 °C without vacuum for 18 hours.) were prepared as 3mm thick dog-bones without solvent (PS and PC follow ASTM D638, PDMS follows ASTM D1708) and stretched by a macroscale tensile tester (Instron, model 5500R) at the same strain rate as thin films.

Annealed PS films were prepared by spin-coating PS solutions onto freshly cleaved mica and then thermal annealed in a vacuum chamber at 115 °C for 15 hours.

4.3.2 Substrates Preparation

Substrates (silicon wafers for PS or glass slides for PC and PDMS) were first cleaned by consecutive sonication in soap and water, acetone and isopropanol for 15 minutes each. After sonication, substrates were dried under nitrogen and exposed to UV-Ozone (Jelight 342 UVO system) for 30 minutes. Next, a sacrificial layer of filtered 3 wt% polyacarylic acid (PAA) (Mw=1800 g/mol, Aldrich) in water solution was spin-coated at 3000 rpm for 30 seconds onto clean substrates.

4.3.3 Preparation of Samples for Quantifying Strain Measurements

We incorporate strain markers (flow-coated NPs grids) in the thin film to quantify accuracy of our strain measurements. We flow-coated nanoparticles (NPs) (same material as the NPs used in Chapter 3) grids on PAA coated glass slides (experimental details can be found in Chapter 3 and reference[118]). To simply describe how we made NPs grids, we flow-coated a first set of NPs lines with spacing of 100 μm on PAA coated silicon wafer and cross-linked them under UV (wavelength at 365 nm, intensity at 120 mJ/cm^2) for 20 minutes. Then we rotated the substrate 90°, flow-coated a second set of NPs lines on top of the first set of lines, and cross-linked them under UV for another 20 minutes. Next, we spin-coated a thin layer of 10:1 PDMS diluted in hexane on top. We placed the sample in a 70 °C oven without vacuum for 18 hours. Then we floated the composite of PDMS with QDs grids on to a water surface (Sample preparation schematics in Figure 4.2).

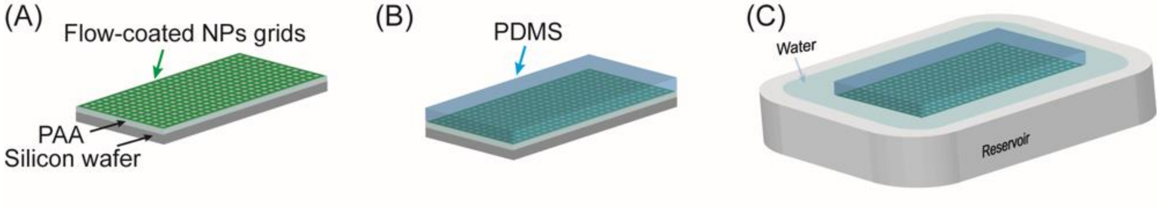

Figure 4.2 – Schematics of preparation process of strain markers (NPs grids) on PDMS thin films. (A) Flow-coat NPs grids on PAA coated silicon wafer. (B) Spin coat a thin layer of PDMS film and cross-link it. (C) Float the composite of PDMS with NPs grids on a water surface.

4.3.4 Finite Element Analysis (FEA)

Both PS and PDMS FEA models use two-dimensional 4-node bilinear plane stress quadrilateral elements with reduced integration and hourglass control. We assign PS as linear elastic material with Poisson's ratio (υ) of 0.3 and PDMS as Neo-Hookean material with Poisson's ratio of 0.4999.

4.3.5 Float Thin Polymer Films on Water

Thin polymer films were first cut into rectangular shape by a razor blade and water was added along edges of the thin films. We waited until water dissolved the sacrificial layer and the thin film was floated completely (the film detached from the substrate), then added water to the same level of the reservoir. The reservoir was an aluminum box with a stripe clamp (a rectangular silicon wafer with dimension of 1 cm by 7 cm) fixed to the reservoir top by epoxy. Next, we utilized tweezers to position the thin film to align with the clamp, followed by adding water to raise the film and attach one end to the clamp. After one end of the film was attached to the clamp, we carefully placed the reservoir on the linear actuator stage and brought the other end of the film to be in contact with the cantilever (Figure 4.1).

4.3.6 Dimension Measurement of Thin Films

Before stress-strain measurements of thin films, and after thin films were attached on both ends (clamp and cantilever), the thin film width (W_F) and thin film length (L_F) were measured from an in-situ top view HD camcorder (Canon VIXIA HF R400) with resolution of 1920 X 1080 pixel. Usually, thin film width (W_F) was 22 mm for PS, PC and PDMS, this was kept the same as the cantilever width. While thin film length (L_F) were 30 mm for PS or 40 mm for PC and PDMS.

4.3.7 Thickness Measurement of Thin Films

Thickness measurement of PS: After stress-strain measurements of PS with thin film tensile system, the PS samples were picked up by a cleaned silicon wafer (washed by sonication in soap water, acetone, toluene and isopropanol) for thickness measurements by ellipsometry (PS refractive index n_{PS}=1.59), atomic force microscopy, and contact profilometer.

Thickness measurement of PC and PDMS: Besides cutting the PC or PDMS film into rectangular piece, the same PC or PDMS sample at spare area was cut into a 1 cm by 2 cm piece, floated on to water surface, and picked up by a cleaned glass slide (washed by sonication in soap water, acetone and isopropanol) for thickness measurements by optical profilometer. Each PS, PC and PDMS sample thickness was averaged by 8 measurements from different locations of the same piece.

4.3.8 Video Capture and Detection

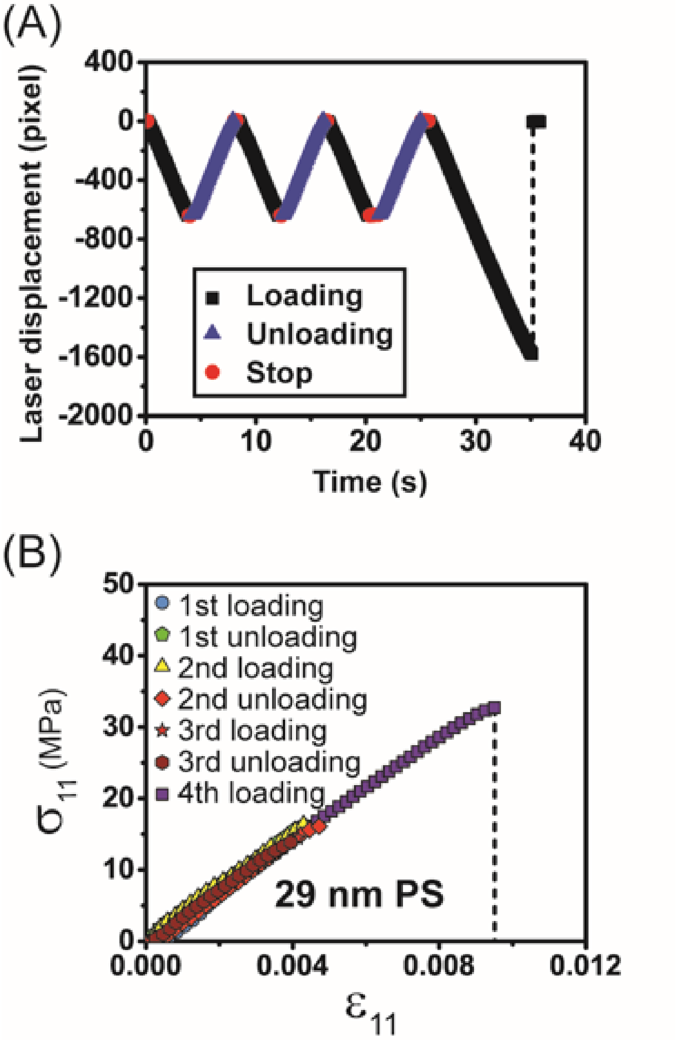

Figure 4.3 – Convert the laser point movement video of 29 nm thick PS to pixel-time relationship and stress-strain relationship. (A) Laser point pixel movement as a function of time converted from the captured video. (B) Convert graph (A) to the relationship of stress to strain by incorporating cantilever calibrations from Figure 4.4.

The laser point was directed from a helium neon laser system (ThorLabs HGR005) at wavelength of 543 nm with beam diameter of 0.64 mm. Experiments were carried out after 30 minutes of the laser system warm-up. Laser point movement was captured by a HD camcorder (Canon VIXIA HF R400) with resolution of 1920 X 1080 pixel. Frame rate was chosen to be 60 frames/seconds (fps) for stretching PS thin films and 30 fps for stretching PC and PDMS thin films. Images were extracted from videos at 30 fps for PS, and 10 fps for PC and PDMS. As the intensity profile of the laser point followed a Gaussian distribution, we fitted the intensity profile to a Gaussian function, determined the maximum intensity pixel position and quantified this position as the center of the laser point. The standard deviation of Gaussian function for the laser point was typically 7 pixels. In this case, to determine thin film strain, we classified the laser point movement by at least 10 pixels difference between two adjacent extracted laser point images. Then we can determine the laser point pixel displacement as a function of time through the whole video (Figure 4.3A). Incorporating the two calibrations of cantilevers (cantilever displacement to laser point movement, and cantilever applied load to laser point movement in Figure 4.4), we can convert the pixel and time relationship to the stress and strain relationship (Figure 4.3B).

4.3.9 Calibrations of the Cantilever

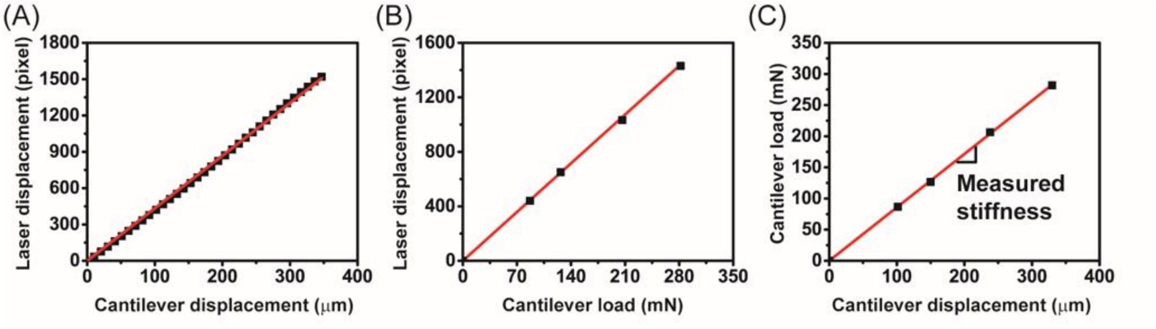

Figure 4.4 – Calibration of the cantilever. (A) Correlate laser point movement in pixel to cantilever known displacement in μm. (B) Correlate laser point movement in pixel to cantilever known load in mN. The error bars denote standard deviations for five independent applied times. (C) Measured stiffness of the cantilever is calculated combining graphs of (A) and (B).

Calibrations of the cantilever were conducted to relate pixel displacement (pixel) to known displacement (μm) and to relate pixel displacement (pixel) to known force (mN). A white screen was placed to reach maximum pixel displacement of the laser point when the cantilever bended to the extent that maximum weight (estimated by $2*E_F*\varepsilon_{11}*H_F*W_F$ (where E_F was an initial estimated value for aligning laser path (usually E_F = bulk material modulus) and ε_{11}=2% for PS or 20% for PC or 60% for PDMS) was applied in X_1 direction. First, by applying known displacement in X_1 direction to the cantilever, the pixel displacement on the white screen is determined (Figure 4.4A). Second, by applying known weights (each weight was applied 5 times) in X_1 direction to the cantilever, again the pixel displacement on the white screen can be determined (Figure 4.4B). 5 different weights for each cantilever was used with 0 g as the minimum and with $2*E_F*\varepsilon_{11}*H_F*W_F$ as the maximum. The other three weights were chosen to be evenly distributed between minimum and maximum weights. Using image analysis, both calibrations of the cantilever were fitted to linear lines with intercepts equal to 0 (Slope S_1 for first calibration of pixel to μm and slope S_2 for second calibration of pixel to mN). Cantilever displacement (δ_C) can be calculated from laser point pixel displacement divided by slope S_1, while total displacement (δ_T) can be calculated from translating actuator velocity multiplied time. As film displacement (δ_F) equaled to total displacement (δ_T) minus cantilever displacement (δ_C), we could calculate thin film strain ($\varepsilon_{11} = \delta_F / L_F$) by dividing film displacement (δ_F) to film length (L_F). Similarly, force exerted on the film (P_F) could be calculated from laser point pixel displacement divided by slope S_2. From theP_F, we could determine stress on the film as σ_{11} by dividing film width (W_F) and film thickness (H_F) to P_F ($\sigma_{11} = \frac{P_F}{W_F \cdot H_F}$). We could also determine measured cantilever stiffness (mN/µm) from these two cantilever calibrations (Figure 4.4C) and compare this measured stiffness to theoretical predicted stiffness by Equation 4.4. We could also use Equation 4.4 to estimate the cantilever modulus (E_C) as 90 GPa which was an expected value for glass.

$$S_C = {}^{P_C}\!/_{\delta_C} = \frac{3E_C I_C}{L_C^3} \qquad \text{Equation 4.4}$$

where S_C was theoretical predicted stiffness of the cantilever, P_C was applied force on the cantilever (which equals to P_F), δ_C was cantilever displacement, E_C was the cantilever modulus, $I_C = \frac{bh^3}{12}$ was the moment of inertia of the rectangular cantilever with b as the cantilever width and h as the cantilever thickness, and L_C was cantilever length.

4.3.10 Choose Appropriate Cantilever

In our system, we controlled the total displacement. If the cantilever were too compliant compared to the film (the cantilever stiffness was much less than the film stiffness), then the total displacement would be applied on the cantilever and the film would not be stretched. In this case, we could not detect any displacement on the thin film. To accurately quantify displacement as well as force exerted on the film in our system, we chose a cantilever which stiffness was comparable and usually two times to the stiffness of the thin film. The stiffness of the cantilever could be tuned to increase by shortening the cantilever length (from Equation 4.4). The stiffness of the film (S_F) was estimated by axial stiffness using Equation 4.5.

$$S_F = \frac{W_F H_F E_F}{L_F} \qquad \text{Equation 4.5}$$

4.4 Results and Discussion

4.4.1 Linear and Non-linear Responses of Polymer Thin Films

Table 4.1 – Modulus comparison between polymer thin films and bulk counterparts

Materials	Thin films			Bulk counterparts		
	Thickness	Number of samples	Modulus	Thickness	Number of samples	Modulus
PS	227 nm	5	3.75 ± 0.16 GPa	3 mm	2	3.12 ± 0.18 GPa
PC	100 nm	4	2.22 ± 0.24 GPa	3 mm	2	2.23 ± 0.04 GPa
PDMS	29 µm	7	0.58 ± 0.02 MPa	3 mm	3	0.57 ± 0.02 MPa

In linear elastic responses, to determine Young's modulus (E), for PS and PC thin films, we do linear fit from strain 0 to 1% in the stress-strain responses. In non-linear elastic responses, to determine E, for PDMS, we utilize Equation 4.6 from Neo-Hookean model to do function fit to calculate modulus. Young's modulus (E) values for films having a thickness greater than the confinement length agree well with bulk values (Table 4.1), which demonstrates the accuracy of our ultra-thin film tensile tester.

$$y = \frac{E}{2 \cdot (1+\upsilon)} (1 + x - \frac{1}{(1+x)^2}) \qquad \text{Equation 4.6}$$

$$y = \sigma_{11},\ x = \varepsilon_{11},\ \upsilon = 0.4999$$

Figure 4.1D and E illustrate the UFT's sensitivity to non-linear responses as exemplified by the plastic deformation of PC thin films (Figure 4.1D) and nonlinear elastic deformation of PDMS thin films (Figure 4.1E). This is the first time that non-linear responses of polymer thin films are directly measured. This non-linear response is from the thin film, not from the instrument (the linear actuator and cantilever), as the actuator exhibits linear relationship of displacement to time when simultaneously stretching the thin film (Figure 4.5).

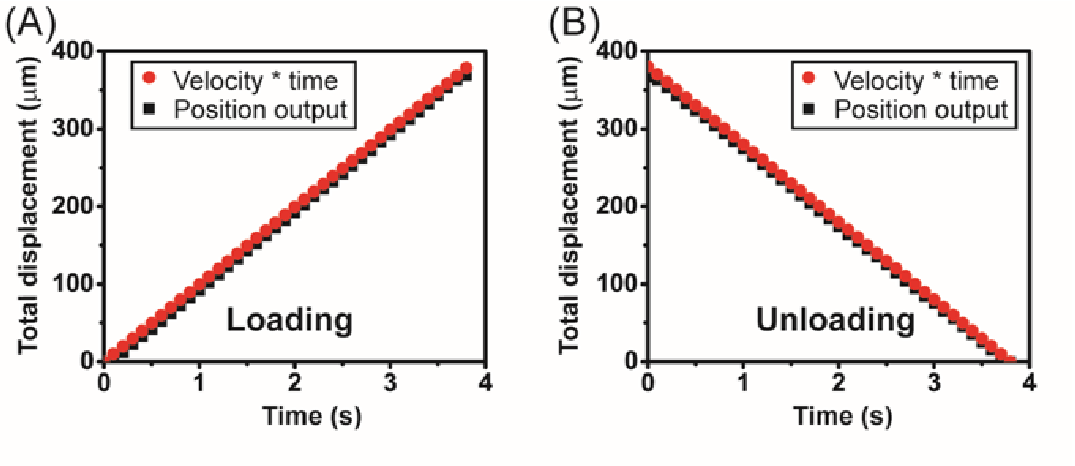

Figure 4.5 – Comparison between the position feedback (black squares) and the position command (velocity times time) (red circles) of the actuator when stretching the thin film. (A) In the loading case. (B) In the unloading case.

4.4.2 Finite Element Analysis

4.4.2.1 Agreement between Experiments and Finite Element Analysis

Finite element analysis (FEA) of the test geometry shows excellent agreement with experimental analysis of the strain state via strain markers (Figure 4.6). Strain markers of flow-coated fluorescent nanoparticle (NP) grids[76] are incorporated into a cross-linked PDMS thin film (Figure 4.2). By applying a fixed displacement to the film and assuming no-slip at the boundaries, we observe the deformation in the NP grid an increasing applied strain, $\varepsilon_{11,App}$ (Figure 4.6A). FEA assumes two-dimensional plane stress[52] and both the overall mesh deformation (Figure 4.6 A-B), and the strain (ε_{11} and ε_{22}) in the upper boundary (Figure 4.6C) and at the center of the film (Figure 4.6D) agree at every applied strain suggesting the FEA appropriately describes the experiments. Additionally, the strain state at the center of the film (Figure 4.6D), coincide with $\varepsilon_{11,App}$ and the strain predicted

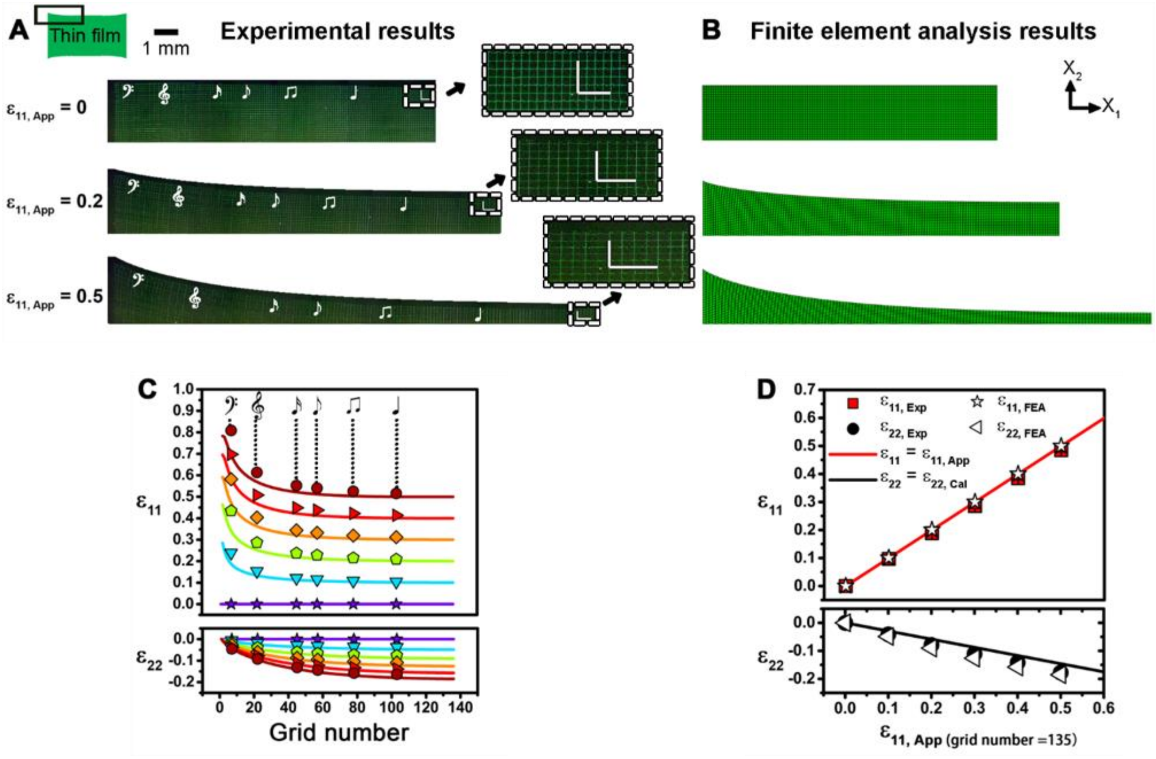

Figure 4.6 - Agreement between experiments and finite element analysis (FEA). (A to B) Representative images focus on upper left corner of the rectangular composite thin film (50 nm thick, 0.3 μm wide and 100 μm spaced QDs grids patterned on 4.5 μm thick, 2.2 cm wide and 4 cm long PDMS film). (A) Experimental results of the composite thin film under applied strains. Same music or L-shaped markers are labelled at the same location on the film. Insets of the L-shaped marker have length of 1.8 mm. (B) FEA results of the film under applied strains. (C) Compare measured strains (data points) from music markers and FEA strains (solid lines). (D) Compare average measured strains (solid data points with error bars) from L-shaped markers, FEA strains (open data points), applied strains (the red solid line) and calculated strains (the black solid line from fits to Equation 4.7). The error bars denote standard deviation for five measurements.

in the orthogonal direction, $\varepsilon_{22,\mathrm{Cal}}$ using an incompressible Neo-Hookean model (Equation 4.7).

$$\varepsilon_{22,Cal} = \left(1+\varepsilon_{11,App}\right)^{-1/2} - 1 \qquad \text{Equation 4.7}$$

4.4.2.2 Consider Stretching Rectangular Thin Films as Undergoing Uniaxial Tension

In classical uni-axial tensile tests, dog-bone shaped samples are prepared. In the gauge area of the dog-bone sample, stress and strain are uniformly distributed. However, in the thin film case, the dog-bone shaped sample is hard to prepare. We prepare rectangular shaped samples and utilize FEA to quantify whether we can consider stretching rectangular samples as undergoing uni-axial tension. In FEA, we define aspect ratio as the length of the film divided by the width. As we study thin films with high ratio of length to thickness (~10^5), these films could be considered as two-dimensional materials[52] and use two-

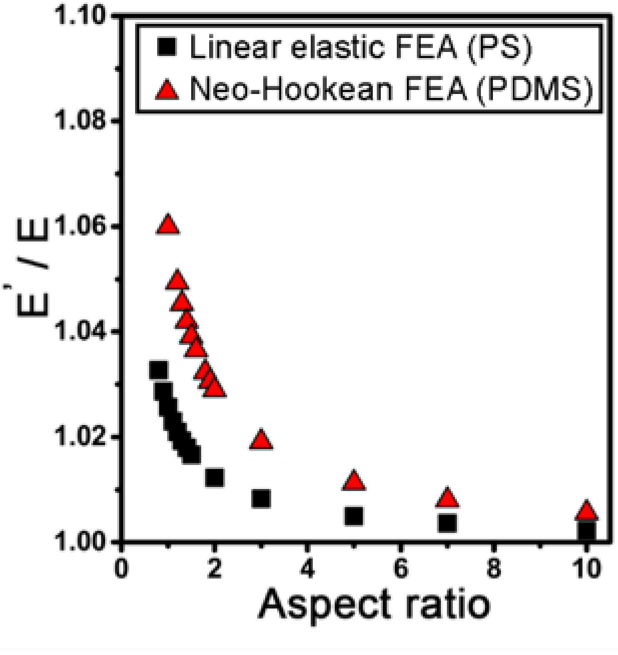

Figure 4.7 - Difference between nominal modulus from the rectangular thin film boundary E’ and material input modulus E for both PS and PDMS as a function of aspect ratio from FEA.

dimensional model in FEA. We calculate the nominal modulus, E', using the nominal stress

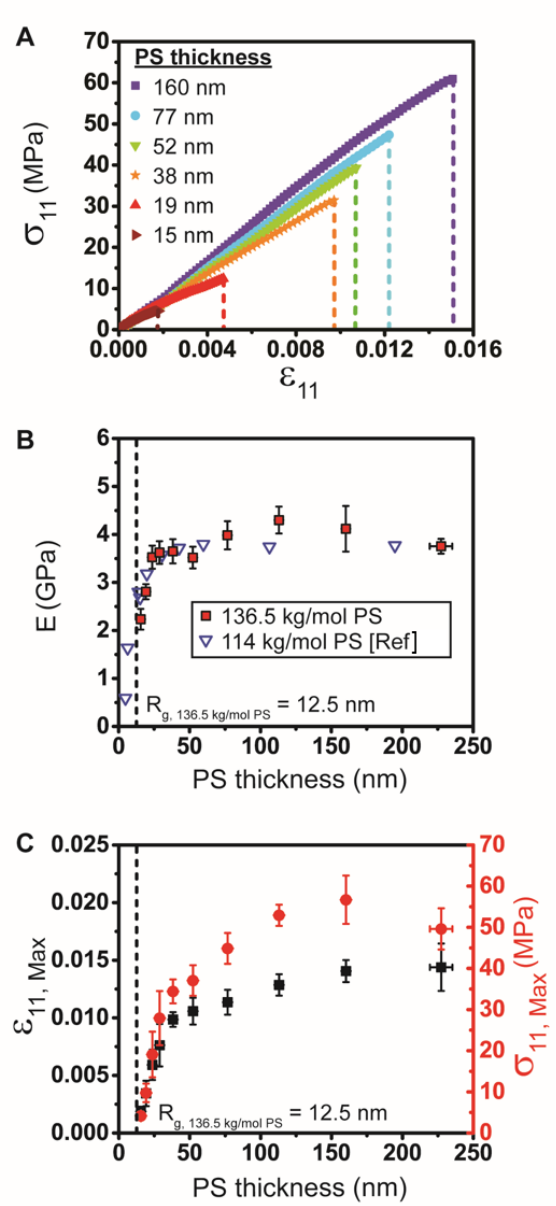

Figure 4.8 - Mechanical property dependence on PS thickness. (A) Six PS films of varying thicknesses stretching until break, each yields a stress-strain response. (B) Modulus E (red filled squares) versus PS thickness. The error bars denote standard deviations for five independent films. For thicknesses above 19 nm, each film has seven measurements (six measurements from cycling at small strains and one measurement from stretching until break). Violet open circles and blue open triangles are PS modulus from reference (Stafford, C. M.; Vogt, B. D.; Harrison, C.; April, R. V; Re, V.; Recei, M.; June, V. Elastic Moduli of Ultrathin Amorphous Polymer Films. *Macromolecules* **2006**, *39*, 5095–5099.) (C) The maximum strain $\varepsilon_{11,\mathrm{Max}}$ (black squares) and maximum stress $\sigma_{11,\mathrm{Max}}$ (red circles) of PS films as a function of thickness. The error bars denote standard deviations for five independent films.

at the film edge (similar to experiment) and compare it with the intrinsic modulus, E, input parameter. Figure 4.7 illustrates that the ratio of these moduli, E'/E, differ by a factor of less than 1.06 and 1.04 for simulated PS and PDMS, respectively. Nevertheless, for completeness, we use E'/E as a correction factor in the modulus values reported here.

4.4.3 Mechanical Properties of PS Thin Films as a Function of Film Thickness

After demonstrating the validity of UFT in characterizing rectangular thin films, we will investigate the effect of polymer chain nanoconfinement on the observed mechanical properties. Ultra-thin films of PS which thickness ranging from 15 nm to 220 nm were stretched at strain rate of 0.0033 s^{-1} until break (Figure 4.8A). Most notably, the modulus, E is observed to undergo a precipitous decrease as a function of film thickness starting at $h_F = 23$ nm (Figure 4.8B). We note that this transition length scale is similar to that in observations of T_g and E variation as well as the size of the polymer chain ($2R_g = 25$ nm, R_g is the radius of gyration) [41,62]. Maximum strain $\varepsilon_{11,Max}$ and the maximum stress

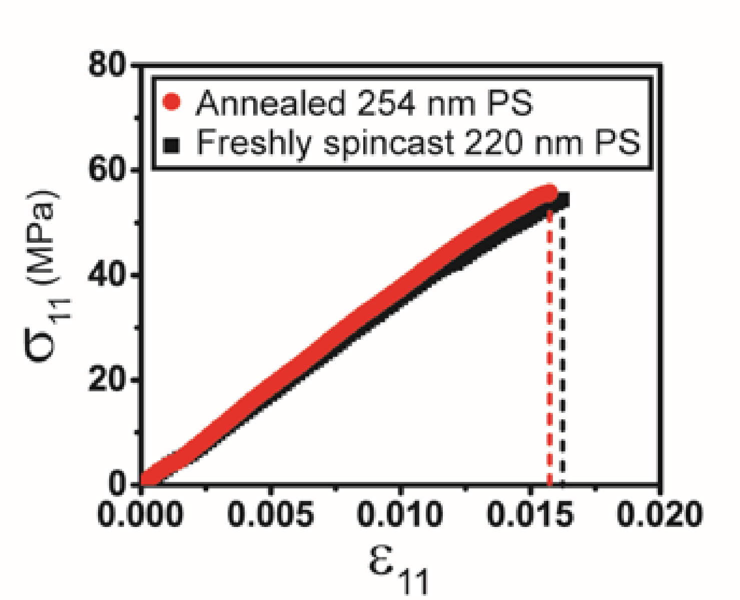

Figure 4.9 – Stress-strain responses of annealed PS films versus freshly spincast PS films.

$\sigma_{11,Max}$, which comprise the failure point on the stress-strain curves, decrease with decreasing PS thickness, but show an increased rate of deterioration at h_F = 38 nm (Figure 4.8C). (Vacuum annealing of the film above T_g of the thickest PS film tested here (~ 200 nm of 137 kg/mol (M_w) PS) has no influence on the stress-strain response (Figure 4.9).)

The precipitous decrease in E measured with the UFT agrees with previous predictions of surface mobility theory[41,43,44,48,62,111]. However, the surface mobility theory is insufficient to predict the decrease in $\varepsilon_{11,Max}$ we report here. This discrepancy is likely due to the dominant role of interchain entanglement density at strains close to failure. As the thin film thickness decreases, interchain entanglement density dramatically decreases with fewer entanglement points between chains[47,119]. To explain this dramatic embrittlement of ultra-thin films of polystyrene, we recall that polystyrene fails through the development and breakdown of crazes, which are networks of nanoscale fibrils. The stability of craze fibrils is controlled by the maximum stretch ratio of the molecular network: $\lambda \sim l_e / d_o$,

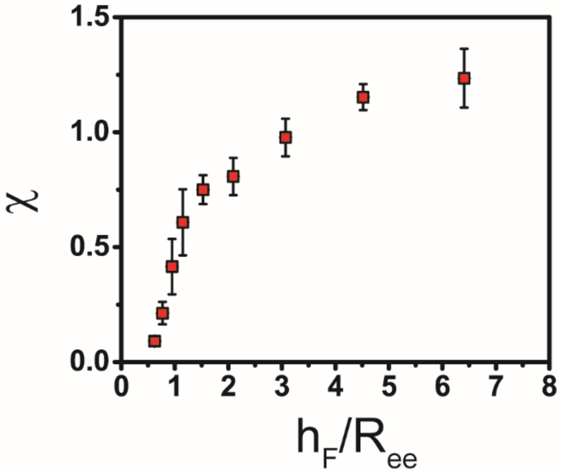

Figure 4.10 - The fraction of entangled chains under load bearing as a function of degree of thin film confinement. The error bars denote standard deviations for five independent films.

where l_e is the contour length of the chain between entanglements and d_o is the characteristic size scale of the chain between entanglements in the non-strained configuration. As proposed by Donald and Kramer[120], the breakdown of the craze fibrils is controlled by the true force exerted on the chains in the load bearing molecular network, f_m, within the craze. For a first order approximation, $f_m = \pi D_o^2 S/(4n_e)$ where S is the surface stress of the craze, D_o is the diameter of an unstrained cylinder of material that will form a craze fibril, and n_e is the total number of effectively entangled chains per area of deformed craze fibril. D_o can be considered a material constant, and $n_e \approx \frac{\pi}{24} v_{e,o} \chi^{3/2} D_o^4 / d_o$ where $v_{e,o}$ is the density of entangled chains in a thick film and χ is the fraction of entangled chains that participate in load sharing. If the craze fibril breakdowns when $f_m \geq f_B$, where $f_B$is the force to break a backbone bond of a polymer chain (~3x10^{-9} N for PS[121]), then the stress at failure is $S_f \approx \frac{f_B\, v_{e,o}\, D_o^2}{6d_o} \chi^{3/2}$. Therefore, the fraction of load bearing entangled chains scales as $\chi \sim \left(S_f / S_{f,o}\right)^{2/3}$ where $S_{f,o}$ is the craze failure stress for bulk materials. Figure 4.10 shows the determined fraction of load bearing entangled chains, χ, as a function of normalized thickness, h_F/R_{ee}. Consistent with recent theoretical studies [74], as well as an experimental study[47] that used indirect morphology data to determine the density of load bearing entanglements, we find that the number of inter-chain entanglements decreases significantly as thickness decreases. In support of scaling arguments put forward by DeGennes[73], as film thickness decreases, the statistical configuration of the chains within the film changes such that chains interact more with themselves rather than neighboring chains. As Si et al[47] describe, this configurational change results in fewer inter-chain entanglements (i.e. load bearing entanglements) and more intra-chain entanglements, while their sum remains approximately constant. Therefore, the loss of inter-chain entanglements does not allow polymers to be strained further as others have proposed, but rather polymers that fail by crazing, such as polystyrene, become increasingly brittle.

4.4.4 Hysteresis in the Elastic Region

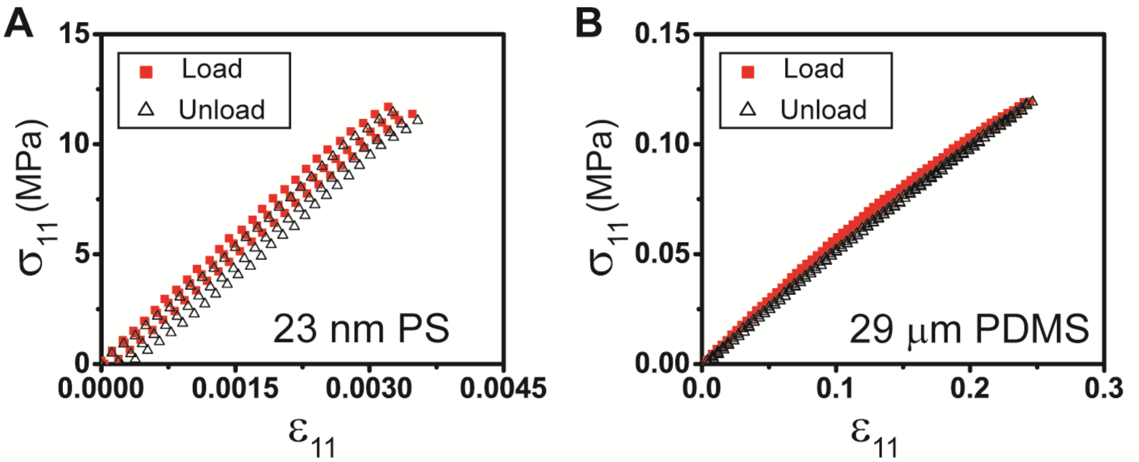

Figure 4.11 - Hysteresis via cycling. (A to B) Stress-strain responses of three load and unload cycles to a ε_{11} strain (0.4% for PS, and 24% for PDMS). (A) 23 nm PS. (B) 29 μm PDMS.

To demonstrate the reproducibility of UFT in characterizing the stress-strain response in the elastic regime prior to failure, load-unload cycles were conducted for the same thin film including PS (linear elastic response) and PDMS (nonlinear elastic response). After three cycles, PS demonstrates little hysteresis and PDMS demonstrates almost no hysteresis (Figure 4.11).

To quantify the qualitative amount of hysteresis, we utilize resilience value of each cycle. Resilience is the fraction of strain energy density from unloading (area underneath the unloading stress-strain curve) to strain energy density from loading (area underneath the loading stress-strain curve). For ideal elastic material, resilience equals to 1. From Figure 4.12, resilience of PS thin films does not vary statistically with PS film thickness and it falls in the range of 0.8 to 0.95. This resilience is lower than the resilience of PDMS thin film, as well as PDMS and PS bulk counterparts (Figure 4.12).

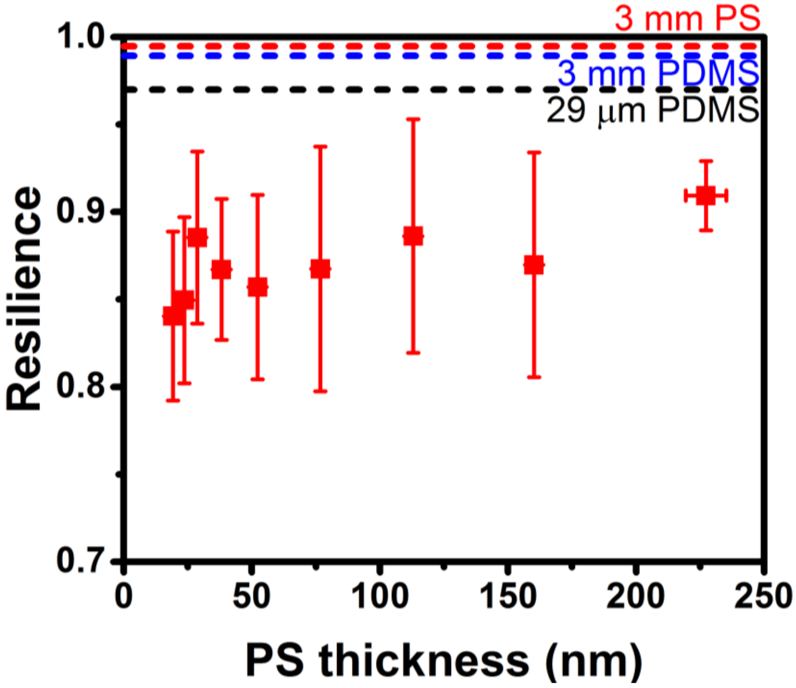

Figure 4.12 – Resilience via cycling. Red rectangles represent PS thin films, and red dashed line is its bulk counterpart (3mmm thick). Black dashed line is thin PDMS film (29 μm thick) and blue dashed line is its bulk counterpart (3 mm thick).

4.4.5 Elastic Stretching Energy versus Surface Energy

In this chapter, we stretch thin films uniaxially on water surface. In bulk material uniaxial tests, people stretch bulk samples in air. Is there any effect of liquid to our system? We do not consider any dissolving of the polymer from the liquid (tested polymer thin films are hydrophobic and are tested in less than 10 minutes)[122]. If there is any effect from liquid to our measurements, it would be taken into account on the aspect of the surface energy.

In bulk materials, its specific surface area (surface area divides by volume of the sample) is much smaller than the specific surface area of thin films. For thin films, surface energy (surface area dominated) will contribute more to the total energy than bulk materials. For thin films floating on the liquid, the surface tension (γ) is defined as

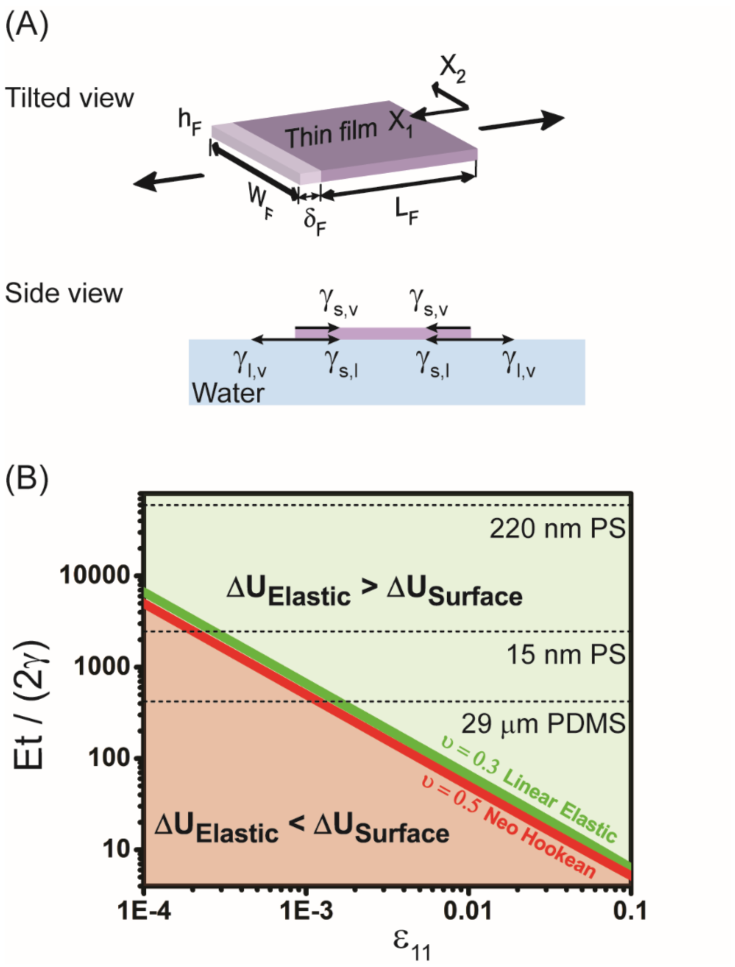

Figure 4.13 – Surface energy contribution in stretching thin films. (A) Schematic of surface tension acting on the thin film. (B) Comparison between elastic energy and surface energy as a function of strain. Two solid lines represent the state when elastic energy equals to surface energy. Green solid line and red solid line are for linear elastic material with Poisson's ratio (υ) of 0.3 and Neo-Hookean material with υ of 0.5 respectively. The two color shaded regime represent states of surface energy dominated regime (light red colored regime) and elastic energy dominated regime (light green colored regime).

$\gamma = \gamma_{s,V} + \gamma_{s,l} - \gamma_{l,V}$ by simplifying the thin film edge as being perpendicular to the liquid surface (Figure 4.13A). When stretching the thin film uni-axially on water surface, surface energy change of the thin film will be

$$\Delta U_{Surface} = \gamma\left[\left(w_F + \Delta w\right)\left(L_F + \Delta L\right) - w_F \cdot L_F\right] \qquad \text{Equation 4.8}$$

and elastic energy change of the thin film will be

$$\Delta U_{Elastic} = \int_0^{\delta_F} E \cdot \varepsilon_{11} \cdot w_F \cdot t_F \, d\left(\Delta L\right) \qquad \text{Equation 4.9}$$

The difference between elastic energy and surface energy can be calculated as a function of strain (Equation 4.10).

$$\frac{\Delta U_{Elastic}}{\Delta U_{Surface}} = \frac{E \cdot t_o \cdot \varepsilon_{11}}{2\gamma\ (1\text{-}\upsilon\text{-}\upsilon \cdot \varepsilon_{11})} \qquad \text{Equation 4.10}$$

For stretching thin polymer films on water surface, incorporating surface tension value from others for PS and PDMS[123–126], our tested polymer thin films are in an elastic energy dominated system (Equation 4.10 and Figure 4.13) and we can neglect surface energy contribution to the total energy.

4.5 Conclusion

In summary, we illustrate an ultrathin film tensile-tester (UFT) for delicately quantifying the full uniaxial stress-strain response of ultrathin polymer films. We then use this method to directly investigate the thickness dependence of modulus, maximum tensile strain and maximum tensile stress as thickness approaches the radius of gyration of the polymer chains. This method opens opportunities for analyzing not only the size dependence of the mechanical response of any polymer films or composites, but also enables testing of ultrathin two-dimensional materials including graphene[127] and molybdenum disulfide (MoS_2)[128].

4.6 Acknowledgements

This work was funded by the Center for Hierarchical Manufacturing (CMMI-1025020) at the University of Massachusetts. We thank NSF MRSEC (NSF DMR-2820506) for facilities support. I would like to thank Shelby Hutchens, Yu-Cheng Chen, Sami Fakhouri, Benny Davidovitch, Dayong Chen and Jon Pham for their fruitful discussions, Dan King, G. Connor Evans, Yue Zhang, Zhan H. Yang and Yuanfang Gong for help during the experiments, and Shelby Hutchens and Yu-Cheng Chen for proofreading support.

CHAPTER 5

MOLECULAR WEIGHT DEPENDENCE OF ULTRA-THIN POLYMER FILMS IN MECHANICAL PROPERTIES

5.1 Introduction

In Chapter 4, we have introduced the new method of custom built thin-film tensile tester and demonstrating its ability to quantify stress-strain response of brittle, ductile, elastomeric polymer thin films. The primary finding from Chapter 4 is that the failure properties depend on polystyrene thin film thicknesses, which we attribute to polymer chain entanglement density change in the confined thin film. To verify our hypothesis on chain entanglements in thin polymer films, we expand the thin film study in this chapter by varying polystyrene molecular weights.

Despite numerous studies of confinement effects on thin polymer film properties (e.g. glass transition temperature (T_g)[41,43,44,64] and viscosity[48]), many inconsistent theoretical explanations about thin film polymer chain dynamics have been proposed. Specifically, the importance of chain mobility and entanglements is not well understood. In addition, mechanical properties testing of thin films is usually limited to Young's modulus[67] at small applied strains. Few studies have been carried out on thin films at large applied strains when entanglements directly affect properties[47]. As molecular weight increases, the number of entanglements is expected to increase. We will investigate entanglement effects of thin films by systematically varying the molecular weight and delicately measuring the failure properties of thin films.

Many different polymers have been used to study the mechanical properties of thin films[129,130]. In particular, polystyrene (PS) has been studied extensively. For PS thin films, measurements of T_g[60,131] and modulus[49,50] have indicated that the PS chain mobility depends on film thickness and molecular weight. These two parameters are also applicable to PS chain entanglements from measuring neck thickness during crazing[47] and onset of plastic strain[70]. However, the full characterization of mechanical properties of PS thin films within one method, revealing polymer chain mobility and entanglements simultaneously, has been limited. Current methods usually examine only one property from a single method using indirect measurements. In this study, we directly measure the stress-strain responses of PS thin films with a custom built ultrathin-film tensile tester (introduced in the last chapter). Specifically, we investigate modulus, maximum tensile strain, and maximum tensile stress from the stress-strain response to gain new insights of polymer entanglements and chain mobility by varying PS molecular weights and film thicknesses.

5.2 Approach

We directly measure the stress-strain response of uniaxially stretched PS thin films to quantify maximum tensile strain ($\varepsilon_{11,max}$), maximum tensile stress ($\sigma_{11,max}$) and modulus (E). The custom built ultrathin-film tensile tester used here is the same as in Chapter 4. In brief, a thin rectangular film is stretched with the support of water. One end of the film is attached to a clamp (made of silicon wafer) and the other end is attached to a cantilever (made of cover glass). From the laser deflection off the cantilever, the force and displacement exerted on the film are quantified which provides stress-strain responses of the film.

5.3 Experimental

5.3.1 Materials

PS of four different molecular weights (Polymer Source Inc.) were used: (1) 61.8k PS: Weight-average molecular weight, M_w = 61.8 kg/mol, PDI = 1.03. (2) 137k PS: M_w = 137 kg/mol, PDI = 1.05. (3) 490k PS: M_w = 490 kg/mol, PDI = 1.05. (4) 853k PS: M_w = 853 kg/mol, PDI = 1.08. PS films with thicknesses ranging from 15 nm to 250 nm were prepared by spin-coating filtered PS solutions of different weight percent (0.5 wt% to 5 wt%) in toluene.

5.3.2 As-cast PS Films

Substrates (silicon wafers, ~ 500 µm thickness, 100 orientation, P/B doped, University Wafers) typically cut into 4 cm x 5 cm were first cleaned by sonication consecutively in soap and water, acetone, toluene and isopropanol for 15 minutes. After sonication, substrates were dried under nitrogen and exposed to UV-Ozone (Jelight 342 UVO system) for 30 minutes. Next, a sacrificial layer of filtered 1 wt% polyacarylic acid (PAA) (Mw=1800 g/mol, Aldrich) in water was spin-coated at 3000 rpm for 30 seconds onto clean substrates. Then the PS solution was spin-coated on top of the PAA layer.

5.3.3 Thermal Annealed PS Films

For approximately 200 nm thin films, PS solutions were spin-coated onto freshly cleaved mica.

For 15 nm to 25 nm thin films, PS solution were spin-coated onto poly (2-methacryloyloxyethl phosphorylcholine) (polyMPC) covered silicon wafers instead of PAA in as-cast PS films, as PAA cannot be easily dissolved after thermal annealing. The synthesis of polyMPC was discussed in details by G. Hu and coworkers[132]. Cleaning of silicon wafers followed the same procedure for as-cast polystyrene films. A sacrificial layer of filtered 1 wt% PolyMPC (Mw = 38 kg/mol, PDI = 1.19) in water was spin-coated onto cleaned silicon wafers. Then the PS solution was spin-coated on top of polyMPC layer.

After preparing PS thin films on substrates, these films were thermal annealed in the vacuum chamber at 115 °C for 15 hours.

5.3.4 Releasing PS Films from Substrates

Thin films were cut into rectangular shape by razor blade in the dimension of 2.2 cm by 4 cm. Then the sample was placed in a reservoir and water was added along edges of the thin film. We waited until water released the thin film completely (the film detached from the substrate) and added water to raise the film to the same level of the reservoir. The reservoir was an aluminum box with a stripe clamp (silicon wafer with dimension of 1 cm by 7 cm) fixed to the reservoir top by epoxy. Next, we utilized tweezers to position the thin film to align with the clamp and added water to attach one end of the film to the clamp. After one end of the film was attached to the clamp, we carefully placed the reservoir on the linear actuator stage and brought the other end of the film into contact with the cantilever.

5.3.5 Dimension Measurement of Thin Films

Before stress-strain measurements of thin films, and after thin films attached to both ends (clamp and cantilever), thin film width (W_F) and thin film length (L_F) were measured from an in-situ top view HD camcorder (Canon VIXIA HF R400) with resolution of 1920 X 1080 pixels. Usually, thin film width (W_F) was 22 mm, which was the same as the cantilever width and the thin film length (L_F) was 30 mm.

5.3.6 Thickness Measurement of PS Thin Films

After stress-strain measurements of PS with our thin film tensile testing system, the PS samples were picked up by a cleaned silicon wafer (washed by sonication consecutively in soap and water, acetone, toluene and isopropanol) for thickness measurements by ellipsometry (PS refractive index n_{PS}=1.59), atomic force microscopy, and contact profilometry. Each PS sample thickness was averaged by 8 measurements from different locations of the same piece.

5.4 Results and Discussion

5.4.1 Mechanical Properties Dependence on Molecular Weights and PS Film Thicknesses

When comparing bulk samples, no significant difference in bulk mechanical properties are expected for the four molecular weights examined here because they are all above the bulk critical entanglement molecular weight (M_c, 35 kg/mol)[133,134]. However, theories developed for bulk polymers do not translate to the case of thin films that are dimensionally confined by the thickness. To understand the mechanical properties of thin films, we must understand how dimensionally confined entanglements and mobility influence chain dynamics. We choose the route of examining dependence of $\sigma_{11,max}$, $\varepsilon_{11,max}$, and E on molecular weights and thin film thicknesses.

For 853 kg/mol (853k) and 490 kg/mol (490k) PS thin films, $\sigma_{11,max}$, $\varepsilon_{11,max}$, and E are independent of molecular weight within our tested film thickness region (Figure 5.1). For these two molecular weights, $\sigma_{11,max}$ and $\varepsilon_{11,max}$ decrease as the film thickness decreases from 254 nm to 25 nm. Modulus remains statistically unchanged from 254 nm to 100 nm, then decreases as thickness decreases from 75 nm to 25 nm. For very thin films with thicknesses of 20 nm and 16 nm, $\sigma_{11,max}$ and E deviate from this decreasing trend, but $\varepsilon_{11,max}$ continues to decrease.

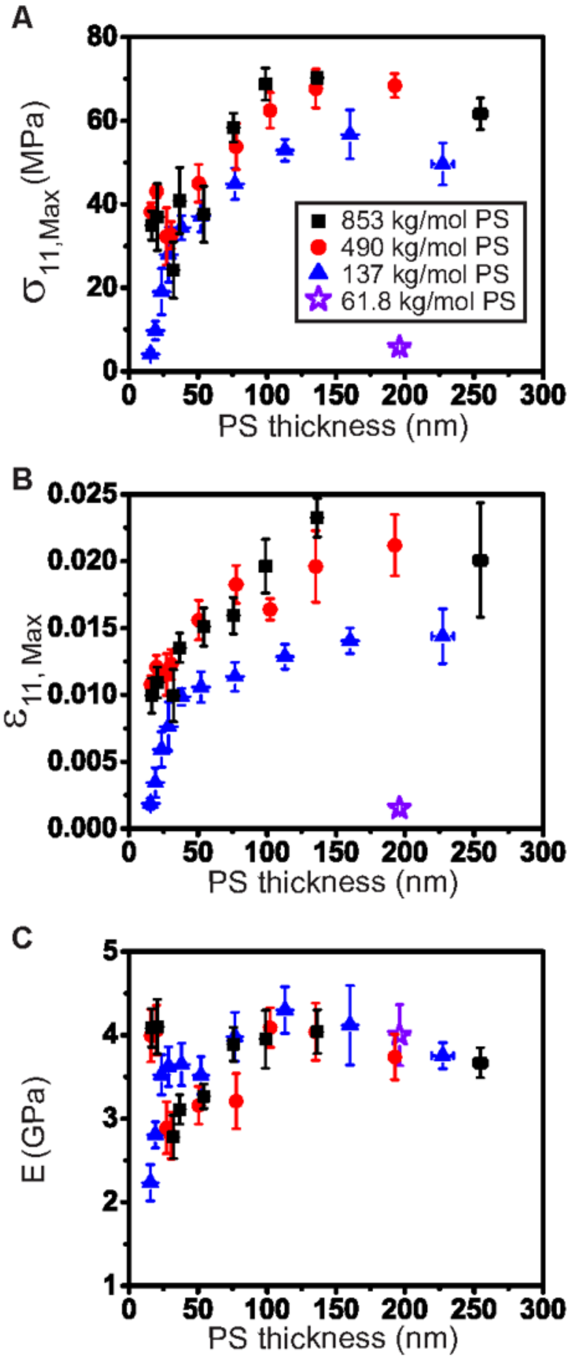

Figure 5.1 - Mechanical properties dependence on polystyrene (PS) film thickness and molecular weight**.** (A) Maximum tensile stress ($\sigma_{11,Max}$). (B) Maximum tensile strain ($\varepsilon_{11,Max}$). (C) Modulus (E). Four molecular weights examined here: 853 kg/mol (black solid squares), 490 kg/mol (red solid circles), 137 kg/mol (blue solid triangles), and 61.8 kg/mol (violet open stars). Each data point represent 5 independent films.

For 137 kg/mol (137k) PS thin films (Figure 5.1), all three parameters, $\sigma_{11,max}$, $\varepsilon_{11,max}$, and E decrease as the film thickness decreases from 250 nm to 16 nm. $\sigma_{11,max}$ and $\varepsilon_{11,max}$ demonstrate an increasing rate of decrease at a film thickness of 38 nm. Modulus demonstrates a precipitous decrease at the film thickness of 23 nm.

For 61.8 kg/mol (61.8k) PS thin films (Figure 5.1), modulus of 200 nm film is comparable with higher molecular weights, but maximum tensile strain and maximum tensile stress is much smaller than that of higher molecular weights. Due to extreme fragility experienced of films at low molecular weight, no stress-strain response can be measured with films below 200 nm with our current technique.

For thin PS films, previous researchers have predicted or measured larger maximum tensile strain for thinner PS films[47,53,70], which is the opposite trend for our measured maximum tensile strain dependence on film thickness (Figure 5.1B). However, they utilize indirect measurements of wrinkle wavelength and amplitude[53,70], and neck thickness during crazing[47] to derive the maximum tensile strain instead of direct measurements in our case. Furthermore, surface mobility theory[53,70] which we expect to be effective for properties in the small strain region, is utilized to explain their failure properties in the large strain region, e.g. the derived maximum tensile strain. We propose that we should utilize the inter-chain entanglement density change for thinner films to explain failure properties of thin films. As film thickness decreases, the inter-chain entanglement density or entanglement points between chains decrease[47,119]. When polymer chains with lower inter-chain entanglement density are stretched to large strains, each chain would result in higher stress and disentanglements would occur more easily. Thereafter, we would expect a lower maximum extensional strain. For the 853k, 490k and 137k PS

(Figure 5.1B), the $\varepsilon_{11,max}$ of each molecular weight decreases as thin film thickness decreases, which is what we expect from chain entanglements decrease. Recent simulation work[74] also predicts that as film thickness decreases, entanglement density decreases. Additionally, at a specific film thickness, entanglement density decreases with an increasing rate. This two features from simulated entanglement density decrease is consistent with our experimental $\varepsilon_{11,max}$ decrease observation.

For modulus within the same molecular weight, our measured modulus decreases for thinner films (Figure 5.1C) from 250 nm to 25 nm. This result is consistent with previous reported modulus[49,50] values using similar PS molecular weights in the same thickness region. Researchers[49,50] have used the surface mobility theory to explain the modulus decrease of thin PS films. However, instead of surface mobility, we think that average segmental chain mobility, which determines properties in the small strain region, is a better parameter to explain the modulus decrease. Furthermore, for higher molecular weight PS (490k and 853k), modulus in the ultra-thin film regime (15 nm to 20 nm) is higher compared to the thickness in the range of 30 nm to 50 nm, which is opposite to what previous researches reported[49,50]. We think that this difference in the ultra-thin film region is likely due to the high molecular weight of the polymer chains. According to previous work[135,136], properties of high molecular weight polymer films are highly affected by the film preparation process[135,136]. The fast solvent evaporation from spin-coating and the large reptation time of high molecular weight PS chains induce more chains to be out of equilibrium. These chains will then be kinetically trapped and have less chain segmental mobility[135,136]. When testing mechanical properties, the effects mentioned above will result in higher E in the ultra-thin film region for high molecular weight PS.

Each data point in Figure 5.1 represents the average of five independent films at a given thickness. Notably, for *E*, each data point consists of 35 measurements from the five independent films (Figure 5.2), as each film undergoes three cycles at small strain and one maximum extension to failure at large strain (exception for 61.8k PS at the thickness of 200 nm and 137k PS at the thickness of 15 nm and 19 nm, as usually only one extension is measured for these fragile films).

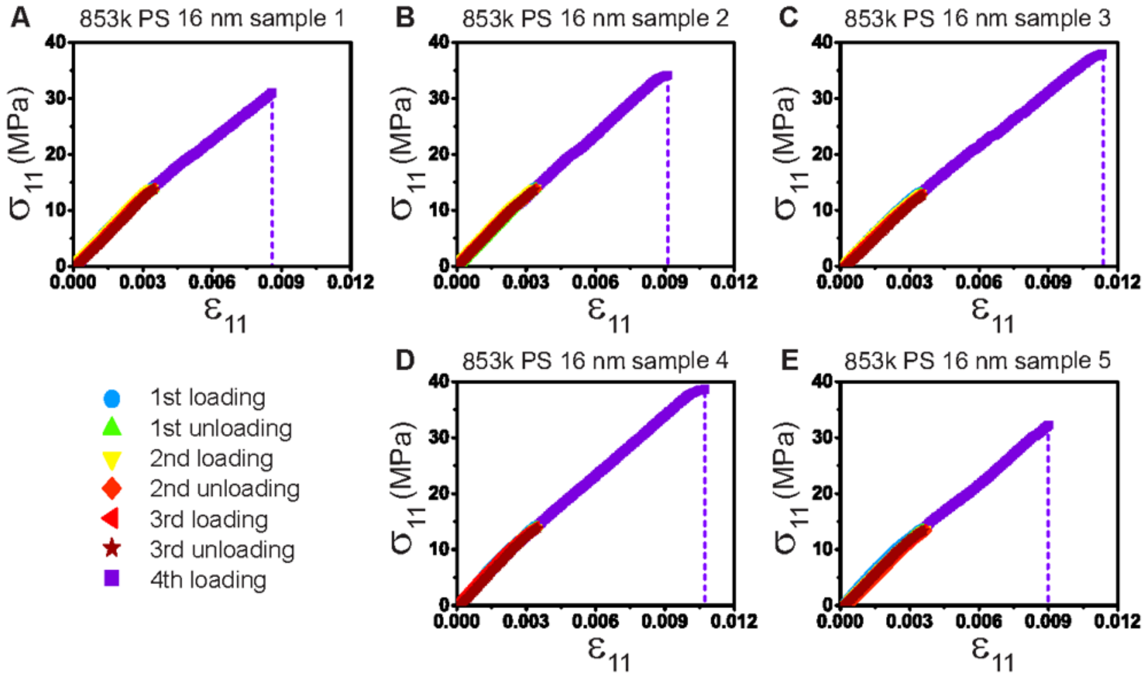

Figure 5.2 - Stress-strain responses of 5 independent samples of 853 kg/mol PS at the thickness of 16 nm. Each sample undergoes three cycles of load and unload to a ε_{11} strain around 0.4% and a maximum load until break.

5.4.2 Stress-Strain Response of Approximately 200 nm Films with Different Molecular Weights

To further support our hypothesis that inter-chain entanglements determines the failure properties of thin films, we examine molecular weight effects on failure properties, as the inter-chain entanglement density can be varied by changing polymer molecular weight. Previous studies demonstrate failure properties to be independent of molecular weights at the same thin film thickness[47]. In contrast, at the same film thickness (for example, ~ 200nm in Figure 5.3), $\varepsilon_{11,max}$ and $\sigma_{11,max}$ decrease as molecular weight lowers. $\varepsilon_{11,max}$ and $\sigma_{11,max}$ dramatically decrease for 61.8k PS. This decrease indicates the correlation of failure properties to molecular weight that controls inter-chain entanglement density in the thin film region. 200 nm films are at least three times thicker than the end to end distance of the polymer chains ($R_{EE} = 2R_g$) studied here (Table 5.1). Even so, this thickness is not thick enough for sufficient inter-chain entanglements to occur for 61.8k PS. In the bulk PS, each chain of 61.8k PS is estimated to have at most two entanglement points, which is not sufficient for strong entanglement properties. These inadequate inter-chain entanglements will result in low maximum tensile strain values when examining 61.8k PS films on the order of hundreds of nanometers.

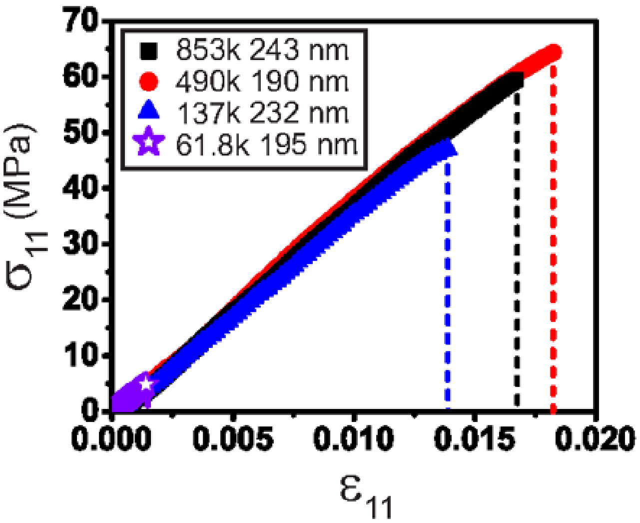

Figure 5.3 - Stress-strain responses of four different molecular weights PS at the thickness of approximately 200 nm.

Additionally, no significant difference is observed for E (Figure 5.1 and Figure 5.3) of ~200 nm PS with different weight average molecular weight (M_W) of 61.8k, 137k, 490k, and 853k. This unchanged modulus is comparable to the bulk PS modulus (Table

4.1). This unchanged *E* proposes that segmental chain mobility is independent of molecular weight for thin films of hundreds of nanometers in thickness. This propose is reasonable as segmental chain mobility is effective within each chain, which determines properties in the small strain region, e.g. *E*; while molecular weight determines inter-chain entanglements, which determines properties in the large strain region, e.g. $\varepsilon_{11,max}$.

Table 5.1 – End to end distance of the polymer chain for tested PS molecular weights

Mw (kg/mol)	R_{EE} (nm)
61.8	17
137	25
490	47
835	61

5.4.3 Thermal Annealing

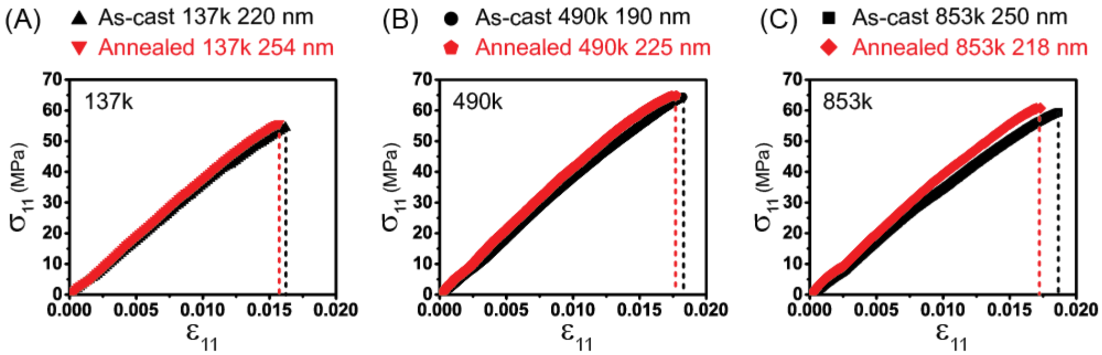

Figure 5.4 – Comparison of stress-strain responses between as-cast (black colored data point) and annealed (red colored data point) PS films with approximately 200 nm thickness. For different molecular weight: (A) 137k, (B) 490k, and (C) 853k.

Thermal annealing helps to remove possible residual solvent in the thin film from the film preparation process. When no difference is observed for approximately 200 nm films upon annealing, we believe that there is no residual solvent affecting mechanical properties. If there is residual solvent in the as-cast film, the modulus will increase upon thermal annealing. In addition, if there is residual solvent, upon thermal annealing, the

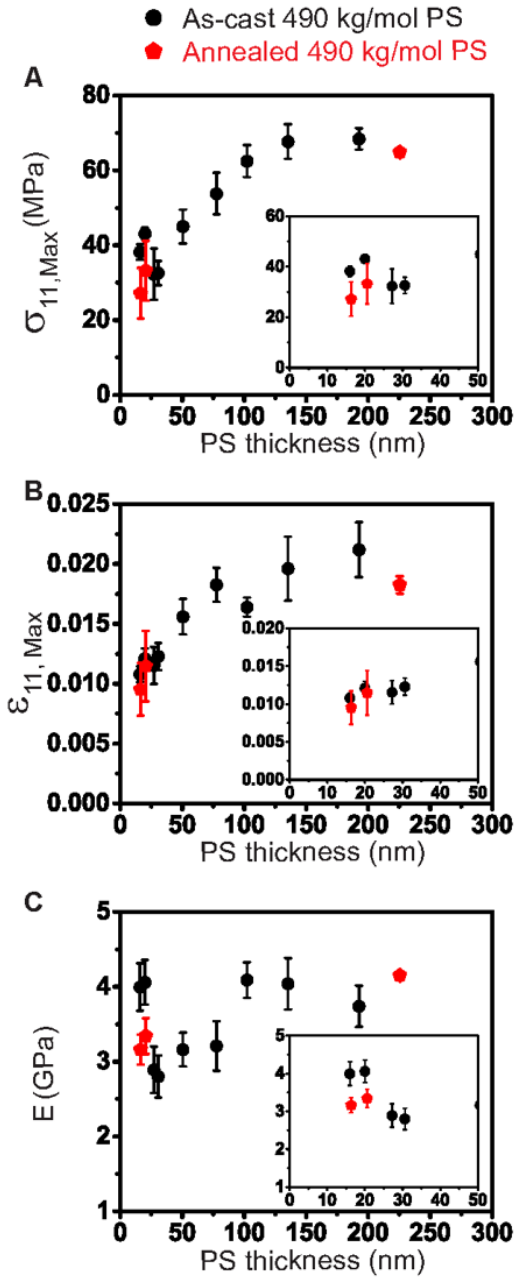

Figure 5.5 - Comparison of 490 kg/mol PS mechanical properties between as-cast (black solid circles) and annealed (red solid pentagons) films as a function of PS thickness. (A) Maximum tensile stress ($\sigma_{11,Max}$). (B) Maximum tensile strain ($\varepsilon_{11,Max}$). (C) Modulus (*E*). Insets are zoom in of the thickness from 10 nm to 50 nm. Each data point of as-cast films represents 5 independent films. Each data point of annealed films represent 2 independent films.

thickest film in our test region (approximately 200 nm) should exhibit the most prominent difference in mechanical properties, e.g. the most increase in *E*. For 853k, 490k, and 137k

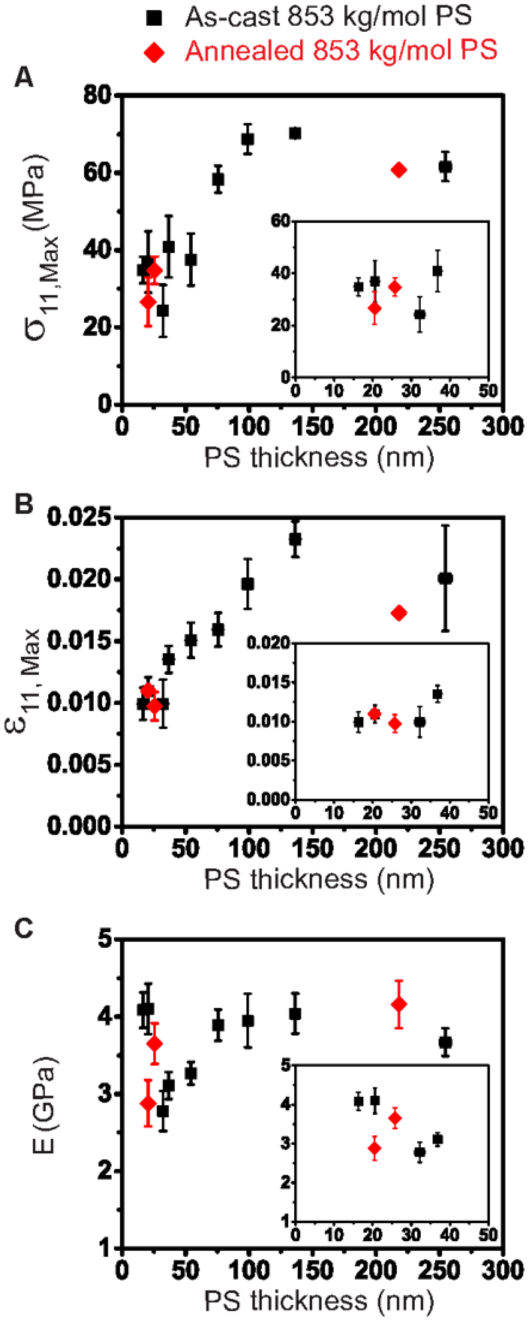

Figure 5.6 - Comparison of 853 kg/mol PS mechanical properties between as-cast (black solid squares) and annealed (red solid diamonds) films as a function of PS thickness. (A) Maximum tensile stress ($\sigma_{11,Max}$). (B) Maximum tensile strain ($\varepsilon_{11,Max}$). (C) Modulus (*E*). Insets are zoom in of the thickness from 10 nm to 50 nm. Each data point of as-cast films represents 5 independent films. Each data point of annealed films represent 2 independent films.

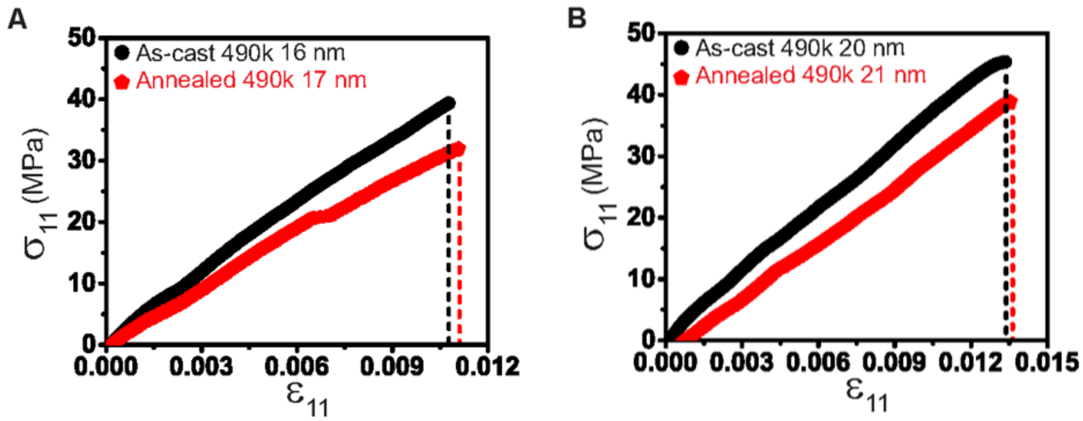

Figure 5.7 - Comparison of 490 kg/mol PS stress-strain responses between as-cast (black solid circles) and annealed (red solid pentagons) films at different PS film thicknesses. (A) 16 nm. (B) 20 nm.

PS films at a thickness of approximately 200 nm, the stress-strain responses of as-cast films are similar to that of annealed films (Figure 5.4). These 200 nm films exhibit no statistical difference in $\sigma_{11,max}$, $\varepsilon_{11,max}$, and E (Figure 5.5 Figure 5.6). These results confirm our belief that there is no effect from residual solvent on thin film mechanical properties.

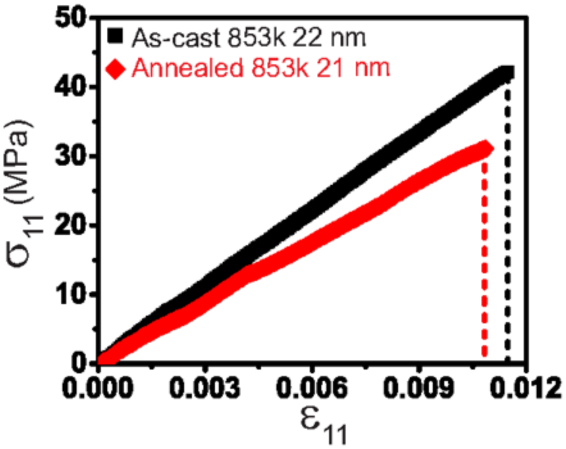

Figure 5.8 - Comparison of 853 kg/mol PS stress-strain responses between as-cast (black solid squares) and annealed (red solid diamonds) films at the film thickness of 21 nm.

Thermal annealing can also help to remove possible residual stress in the thin film from the spin coating process. If there is residual stress, mechanical property difference of thinner films will be more prominent upon thermal annealing, e.g. lower $\sigma_{11,max}$. One origin of residual stress is the radial stress on the polymer chain contributed by centrifugal force from spin-coating. In addition, the fast solvent evaporation leads to a residual tensile stress in the region near the free surface of the film[137]. For 853k and 490k PS films at thicknesses of 16 nm and 21 nm, thermal annealing yields lower $\sigma_{11,max}$ and lower E, while $\varepsilon_{11,max}$ remains unchanged (Figure 5.5, Figure 5.6, Figure 5.7and Figure 5.8). The lower $\sigma_{11,max}$ upon thermal annealing proves the release of residual stress from spin-coating. The stress-strain response difference before and after annealing provides a direct way to measure residue stress or residue strain energy from film preparation process.

At the same time, the lower E upon thermal annealing indicates that stiffening in polymer chains is relieved. In the as-cast films, the fast solvent evaporation induces kinetically trapping, which shows stiffening as segmental chain mobility is limited. As toluene, a good solvent for PS, evaporates during spin-coating to form thin films, PS chains of high molecular weight form oblate coil structures[135,136], which are confined in the thickness dimension and are elongated in the radial direction. Upon thermal annealing, residual stress on these oblate coils are relieved, leading to equilibrate structures such as spherical coils. Thus, upon thermal annealing, chains are less confined by other chains, and are free to move on the polymer chain segmental scale, which determines lower modulus.

For the movement of the entire polymer chain, it is determined by inter-chain entanglement density. The unchanged $\varepsilon_{11,max}$ before and after annealing indicates no average entanglement density change in the films upon annealing for high PS molecular weights. Even though thermal annealing helps to equilibrate chains, our results demonstrate that the transition from non-equilibrium chains to equilibrium chains has no difference in the average entanglement density.

5.5 Conclusions

In summary, we utilize our custom built thin-film tensile tester to quantify molecular weight effects on mechanical properties of thin polystyrene films. By comparing the stress-strain responses of thin films with different molecular weights and film thicknesses, we reveal that failure properties (maximum tensile strain and maximum tensile stress) of thin polymer films decrease as molecular weight or film thickness decreases. These decreases relationships suggest that the polymer chain entanglements decrease dominates failure property decrease in the thin film. Additionally, for ultra-thin polymer films of high molecular weight, preparation process induces residual stress and stiffening in the thin film which can be relieved by thermal annealing. The model polymer studied here is polystyrene at room temperature, a glassy and brittle polymer. Future studies on other types of polymers or materials as well as mechanical properties at elevated temperature (e.g. above T_g) can be developed based on the knowledge gained from PS thin films.

5.6 Acknowledgements

This work was funded by the Center for Hierarchical Manufacturing (CMMI-1025020) at the University of Massachusetts. We thank NSF MRSEC (NSF DMR-2820506) for facilities support. I would like to thank Dan King, Yu-Cheng Chen, and Jon Pham for their fruitful discussions, and Dan King and Jon Pham for proofreading support. I would also like to thank the Origin Lab Corporation for their help with developing video analysis tool. Specifically, Penn Lai, Easwar R. Iyer, Meili Yang and Snow Li from Origin Lab.

CHAPTER 6

CONCLUSION

The work of this thesis utilizes flexible blade flow-coating for assembling ordered polymer structures and composites, and focuses on mechanical property characterizations of thin polymer films. Here we discovered flow dynamics and instabilities in formations of small polymer features. Furthermore, we have developed a new method to directly quantify the full stress-strain responses of thin polymer films.

In Chapter 2, we focus on the formation of self-similar hyper-branched polystyrene structures on substrates with controlled wetting property via flexible blade flow-coating. Combined with flow-coating variables including set distance, stopping time, and initial concentration, we systematically tune the wetting properties (water advancing contact angle varies from 113° to 27°) of silanized substrates by UVO exposure and created a library of polystyrene structures at different controlled variables. At a specific substrate surface energy (UVO exposure time 60s), hyper-branched polystyrene structures are formed. We explain this novel pattern formation through the relationship between Marangoni flow, adsorption, friction and viscosity in the flow-coating. Beyond explaining the formation of these novel hyper-branched structures, our findings provide new, fundamental knowledge on the flexible blade flow-coating method, which is critical for improving and guiding practical implementation of this scalable method for polymer nanostructure fabrication.

In Chapter 3, we develop a one-step process for fabricating hierarchical composite thin films of nanoparticles and polymers via flexible blade flow-coating. The distribution of nanoparticles in different regions (regions with shear, and regions with no shear) is characterized by local volume fraction of nanoparticles. The local volume fraction of nanoparticles in the regions with shear is estimated to be lower than the original volume fraction in the solute. We expect to tune this volume fraction at designated regions by varying the molecular weight of the poly(methyl methacrylate) polymer matrix, as the conformational entropy of the polymer chain dominates the nanoparticle distribution. This is preliminary work demonstrating our capability of fabricating hierarchical nanocomposite thin films to a large scale (cm by cm). For future work, we can utilize energy filtered TEM for directly characterizing local volume fraction of nanoparticles. In addition, we provide a model hierarchical composite material for studying structural effects on mechanical properties of thin films, and studying structural and stiffness effects on directing cell alignments and movements.

In Chapter 4, we design and construct a custom built ultra-thin films tensile tester that stretches thin polymer films on a water surface. We conduct finite element analysis to model mechanical response of the tested samples, and quantitatively correlate results to experimentally measured strains. We quantify the full stress-strain responses of brittle (polystyrene), ductile (polycarbonate), and elastomeric (cross-linked polydimethylsiloxane) polymer thin films at room temperature, characterizing the responses including elastic and plastic regions. We perform measurements on films with thicknesses ranging from 15 nm to 29µm and moduli ranging from 0.2 MPa to 4 GPa. We discover that decreasing in inter-chain entanglement density with decreasing film thickness leads to diminished materials properties. This is, to our knowledge, the first direct measurement of full stress-strain responses of thin polymer films. This technique opens opportunities for testing two-dimensional materials, for example, graphene.

Finally, in Chapter 5, we investigate the molecular weight effect on mechanical properties of thin polystyrene films by utilizing the custom-built thin film tensile tester introduced in Chapter 4. Even though the four molecular weights of polystyrene tested are greater than the critical entanglement molecular weight of polystyrene in bulk, mechanical properties of the thin films are affected by molecular weight and film thickness. Our results verify our belief that inter-chain entanglement density determines the failure properties of thin polymers films, and segmental chain mobility determines the modulus. This study could also help us measure the residual stress in the ultra-thin film induced from the film preparation process. For future work, the temperature effect on mechanical properties of thin polymer films could be examined. As we could compare the modulus and maximum tensile strain values of the thin films as a function of temperature, we would provide a direct way for determining glass transition temperature of thin films and the interchain entanglement changes during the glass transition process.

In conclusion, this thesis demonstrates scientific advances by introducing fabrication of hierarchical composites on large scale and directly quantifying mechanical responses of uniform thin polymer films. The research in this thesis will provide stepping stones for various fields, including understanding polymer physics in confined thin films, and designing advanced devices for nanotechnology applications.

BIBLIOGRAPHY

(1) Grisolia, J.; Viallet, B.; Amiens, C.; Baster, S.; Cordan, A. S.; Leroy, Y.; Soldano, C.; Brugger, J.; Ressier, L. 99% Random Telegraph Signal-Like Noise in Gold Nanoparticle Micro-Stripes. *Nanotechnology* **2009**, *20*, 355303.

(2) Huang, J.; Kim, F.; Tao, A. R.; Connor, S.; Yang, P. Spontaneous Formation of Nanoparticle Stripe Patterns through Dewetting. *Nat. Mater.* **2005**, *4*, 896–900.

(3) Bowden, N.; Brittain, S.; Evans, A. Spontaneous Formation of Ordered Structures in Thin Films of Metals Supported on an Elastomeric Polymer. *Nature* **1998**, *393*, 146–149.

(4) Jing, J.; Reed, J.; Huang, J.; Hu, X.; Clarke, V.; Edington, J.; Housman, D.; Anantharaman, T. S.; Huff, E. J.; Mishra, B.; Porter, B.; Shenker, a; Wolfson, E.; Hiort, C.; Kantor, R.; Aston, C.; Schwartz, D. C. Automated High Resolution Optical Mapping Using Arrayed, Fluid-Fixed DNA Molecules. *Proc. Natl. Acad. Sci. U. S. A.* **1998**, *95*, 8046–8051.

(5) Kraus, T.; Malaquin, L.; Schmid, H. Nanoparticle Printing with Single-Particle Resolution. *Nanotechnology* **2007**, *2*, 570–576.

(6) Huang, J.; Fan, R.; Connor, S.; Yang, P. One Step Patterning of Aligned Nanowire Arrays by Programmed Dip Coating. *Angew Chem Int Ed* **2007**, *46*, 2414–2417.

(7) Cai, Y.; Newby, B. Z. Marangoni Flow-Induced Self-Assembly of Hexagonal and Stripelike Nanoparticle Patterns. *J. Am. Chem. Soc.* **2008**, *130*, 6076–6077.

(8) Hong, S.; Xia, J.; Lin, Z. Spontaneous Formation of Mesoscale Polymer Patterns in an Evaporating Bound Solution. *Adv. Mater.* **2007**, *19*, 1413–1417.

(9) Kim, H.; Lee, C.; Sudeep, P.; Emrick, T.; Crosby, A. J. Nanoparticle Stripes, Grids, and Ribbons Produced by Flow Coating. *Adv. Mater.* **2010**, *22*, 4600–4604.

(10) Lee, D. Y.; Pham, J. T.; Lawrence, J.; Lee, C. H.; Parkos, C.; Emrick, T.; Crosby, A. J. Macroscopic Nanoparticle Ribbons and Fabrics. *Adv. Mater.* **2013**, *25*, 1248–1253.

(11) Stafford, C. M.; Roskov, K. E.; Epps, T. H.; Fasolka, M. J. Generating Thickness Gradients of Thin Polymer Films via Flow Coating. *Rev. Sci. Instrum.* **2006**, *77*, 023908.

(12) Deegan, R. D.; Bakajin, O.; Dupont, T. F. Capillary Flow as the Cause of Ring Stains from Dried Liquid Drops. *Nature* **1997**, 827–829.

(13) Deegan, R. Pattern Formation in Drying Drops. *Phys. Rev. E. Stat. Phys. Plasmas. Fluids. Relat. Interdiscip. Topics* **2000**, *61*, 475–485.

(14) Hu, H.; Larson, R. Analysis of the Microfluid Flow in an Evaporating Sessile Droplet. *Langmuir* **2005**, *21*, 3963–3971.

(15) Kajiya, T.; Kaneko, D.; Doi, M. Dynamical Visualization of "Coffee Stain Phenomenon" in Droplets of Polymer Solution via Fluorescent Microscopy. *Langmuir* **2008**, *24*, 12369–12374.

(16) Kajiya, T.; Monteux, C.; Narita, T.; Lequeux, F.; Doi, M. Contact-Line Recession Leaving a Macroscopic Polymer Film in the Drying Droplets of Water-poly(N,N-Dimethylacrylamide) (PDMA) Solution. *Langmuir* **2009**, *25*, 6934–6939.

(17) Hu, H.; Larson, R. G. Marangoni Effect Reverses Coffee-Ring Depositions. *J. Phys. Chem. B* **2006**, *110*, 7090–7094.

(18) Maillard, M.; Motte, L.; Pileni, M.-P. Rings and Hexagons Made of Nanocrystals. *Adv. Mater.* **2001**, *13*, 200–204.

(19) Maillard, M.; Motte, L.; Ngo, a. T.; Pileni, M. P. Rings and Hexagons Made of Nanocrystals: A Marangoni Effect. *J. Phys. Chem. B* **2000**, *104*, 11871–11877.

(20) Nguyen, V.; Stebe, K. Patterning of Small Particles by a Surfactant-Enhanced Marangoni-Bénard Instability. *Phys. Rev. Lett.* **2002**, *88*, 164501.

(21) Ma, H.; Dong, R.; Van Horn, J. D.; Hao, J. Spontaneous Formation of Radially Aligned Microchannels. *Chem. Commun. (Camb).* **2011**, *47*, 2047–2049.

(22) Shmuylovich, L.; Shen, A.; Stone, H. Surface Morphology of Drying Latex Films: Multiple Ring Formation. *Langmuir* **2002**, 3441–3445.

(23) Maheshwari, S.; Zhang, L.; Zhu, Y.; Chang, H.-C. Coupling Between Precipitation and Contact-Line Dynamics: Multiring Stains and Stick-Slip Motion. *Phys. Rev. Lett.* **2008**, *100*, 044503.

(24) Adachi, E.; Dimitrov, A. S.; Nagayama, K. Stripe Patterns Formed on a Glass Surface during Droplet Evaporation. *Langmuir* **1995**, *11*, 1057–1060.

(25) Dimitrov, A. S.; Nagayama, K. Continuous Convective Assembling of Fine Particles into Two-Dimensional Arrays on Solid Surfaces. *Langmuir* **1996**, *12*, 1303–1311.

(26) Hu, H.; Larson, R. Analysis of the Effects of Marangoni Stresses on the Microflow in an Evaporating Sessile Droplet. *Langmuir* **2005**, *21*, 3972–3980.

(27) Hu, H.; Larson, R. G. Analysis of the Microfluid Flow in an Evaporating Sessile Droplet. *Langmuir* **2005**, *21*, 3963–3971.

(28) Mino, Y.; Watanabe, S.; Miyahara, M. T. Fabrication of Colloidal Grid Network by Two-Step Convective. **2011**, 5290–5295.

(29) Hong, S. W.; Jeong, W.; Ko, H.; Kessler, M. R.; Tsukruk, V. V.; Lin, Z. Directed Self-Assembly of Gradient Concentric Carbon Nanotube Rings. *Adv. Funct. Mater.* **2008**, *18*, 2114–2122.

(30) Hong, S. W.; Byun, M.; Lin, Z. Robust Self-Assembly of Highly Ordered Complex Structures by Controlled Evaporation of Confined Microfluids. *Angew. Chem. Int. Ed. Engl.* **2009**, *48*, 512–516.

(31) Hong, S. W.; Wang, J.; Lin, Z. Evolution of Ordered Block Copolymer Serpentines into a Macroscopic, Hierarchically Ordered Web. *Angew. Chem. Int. Ed. Engl.* **2009**, *48*, 8356–8360.

(32) Xu, J.; Xia, J.; Lin, Z. Evaporation-Induced Self-Assembly of Nanoparticles from a Sphere-on-Flat Geometry. *Angew. Chem. Int. Ed. Engl.* **2007**, *46*, 1860–1863.

(33) Han, W.; Lin, Z. Learning from "Coffee Rings": Ordered Structures Enabled by Controlled Evaporative Self-Assembly. *Angew. Chem. Int. Ed. Engl.* **2012**, *51*, 1534–1546.

(34) Hagedorn, J.; Martys, N.; Douglas, J. Breakup of a Fluid Thread in a Confined Geometry: Droplet-Plug Transition, Perturbation Sensitivity, and Kinetic Stabilization with Confinement. *Phys. Rev. E* **2004**, *69*, 056312.

(35) Cazabat, A.; Heslot, F.; Troian, S.; Carles, P. Fingering Instability of Thin Spreading Films Driven by Temperature Gradients. *Nature* **1990**, *346*, 824–826.

(36) Fanton, X.; Cazabat, A. Spreading and Instabilities Induced by a Solutal Marangoni Effect. *Langmuir* **1998**, *14*, 2554–2561.

(37) Prevo, B. G.; Velev, O. D. Controlled, Rapid Deposition of Structured Coatings from Micro- and Nanoparticle Suspensions. *Langmuir* **2004**, *20*, 2099–2107.

(38) Farcau, C.; Moreira, H.; Viallet, B.; Grisolia, J.; Ressier, L. Tunable Conductive Nanoparticle Wire Arrays Fabricated by Convective Self-Assembly on Nonpatterned Substrates. *ACS Nano* **2010**, *4*, 7275–7282.

(39) Chen, J.; Liao, W.-S.; Chen, X.; Yang, T.; Wark, S. E.; Son, D. H.; Batteas, J. D.; Cremer, P. S. Evaporation-Induced Assembly of Quantum Dots into Nanorings. *ACS Nano* **2009**, *3*, 173–180.

(40) Ray, M. A.; Kim, H.; Jia, L. Dynamic Self-Assembly of Polymer Colloids To Form Linear Patterns. *Langmuir* **2005**, *2*, 4786–4789.

(41) Forrest, J.; Dalnoki-Veress, K.; Stevens, J.; Dutcher, J. Effect of Free Surfaces on the Glass Transition Temperature of Thin Polymer Films. *Phys. Rev. Lett.* **1996**, *77*, 2002–2005.

(42) Wang, J.; McKenna, G. B. Viscoelastic and Glass Transition Properties of Ultrathin Polystyrene Films by Dewetting from Liquid Glycerol. *Macromolecules* **2013**, *46*, 2485–2495.

(43) Gao, S.; Koh, Y. P.; Simon, S. L. Calorimetric Glass Transition of Single Polystyrene Ultrathin Films. *Macromolecules* **2013**, *46*, 562–570.

(44) Ellison, C. J.; Torkelson, J. M. The Distribution of Glass-Transition Temperatures in Nanoscopically Confined Glass Formers. *Nat. Mater.* **2003**, *2*, 695–700.

(45) Hau-Nan Lee, Keewook Paeng, Stephen F. Swallen, M. D. E. Direct Measurement of Molecular Mobility in Actively Deformed Polymer Glasses. *Science (80-.).* **2009**, *323*, 231–234.

(46) Chai, Y.; Salez, T.; McGraw, J. D.; Benzaquen, M.; Dalnoki-Veress, K.; Raphaël, E.; Forrest, J. a. A Direct Quantitative Measure of Surface Mobility in a Glassy Polymer. *Science* **2014**, *343*, 994–999.

(47) Si, L.; Massa, M. V.; Dalnoki-Veress, K.; Brown, H. R.; Jones, R. a. L. Chain Entanglement in Thin Freestanding Polymer Films. *Phys. Rev. Lett.* **2005**, *94*, 127801.

(48) Yang, Z.; Fujii, Y.; Lee, F. K.; Lam, C.-H.; Tsui, O. K. C. Glass Transition Dynamics and Surface Layer Mobility in Unentangled Polystyrene Films. *Science* **2010**, *328*, 1676–1679.

(49) Torres, J. M.; Stafford, C. M.; Vogt, B. D. Impact of Molecular Mass on the Elastic Modulus of Thin Polystyrene Films. *Polymer (Guildf).* **2010**, *51*, 4211–4217.

(50) Stafford, C. M.; Vogt, B. D.; Harrison, C.; April, R. V; Re, V.; Recei, M.; June, V. Elastic Moduli of Ultrathin Amorphous Polymer Films. *Macromolecules* **2006**, *39*, 5095–5099.

(51) Du, B.; Tsui, O. K. C.; Zhang, Q.; He, T. Study of Elastic Modulus and Yield Strength of Polymer Thin Films Using Atomic Force Microscopy. *Langmuir* **2001**, *17*, 3286–3291.

(52) Huang, J.; Juszkiewicz, M.; de Jeu, W. H.; Cerda, E.; Emrick, T.; Menon, N.; Russell, T. P. Capillary Wrinkling of Floating Thin Polymer Films. *Science* **2007**, *317*, 650–653.

(53) Gurmessa, B.; Croll, A. Onset of Plasticity in Thin Polystyrene Films. *Phys. Rev. Lett.* **2013**, *110*, 074301.

(54) Torres, J. M.; Wang, C.; Coughlin, E. B.; Bishop, J. P.; Register, R. a; Riggleman, R. a; Stafford, C. M.; Vogt, B. D. Influence of Chain Stiffness on Thermal and Mechanical Properties of Polymer Thin Films. *Macromolecules* **2011**, *44*, 9040–9045.

(55) Stafford, C. M.; Harrison, C.; Beers, K. L.; Karim, A.; Amis, E. J.; Vanlandingham, M. R.; Kim, H.; Volksen, W.; Miller, R. D.; Simonyi, E. V. A. E. A Buckling-Based Metrology for Measuring the Elastic Moduli of Polymeric Thin Films. *Nat. Mater.* **2004**, *3*, 545–550.

(56) O'Connell, P. a; McKenna, G. B. Rheological Measurements of the Thermoviscoelastic Response of Ultrathin Polymer Films. *Science* **2005**, *307*, 1760–1763.

(57) Rubinstein, M.; Colby, R. *Polymer Physics*; Oxford, Oxford Univ Press, 2003.

(58) Donth, E. The Size of Cooperatively Rearranging Regions at the Glass Transition. *J. Non. Cryst. Solids* **1982**, *53*, 325–330.

(59) Wang, J.; McKenna, G. B. A Novel Temperature-Step Method to Determine the Glass Transition Temperature of Ultrathin Polymer Films by Liquid Dewetting. *J. Polym. Sci. Part B Polym. Phys.* **2013**, *51*, 1343–1349.

(60) Dalnoki-Veress, K.; Forrest, J.; Murray, C.; Gigault, C.; Dutcher, J. Molecular Weight Dependence of Reductions in the Glass Transition Temperature of Thin, Freely Standing Polymer Films. *Phys. Rev. E* **2001**, *63*, 031801.

(61) Mattsson, J.; Forrest, J.; Borjesson, L. Quantifying Glass Transition Behavior in Ultrathin Free-Standing Polymer Films. *Phys. Rev. E. Stat. Phys. Plasmas. Fluids. Relat. Interdiscip. Topics* **2000**, *62*, 5187–5200.

(62) Forrest, J. A.; Dutcher, J. R. Interface and Chain Confinement Effects on the Glass Transition Temperature of Thin Polymer Films. *Phys. Rev. E* **1997**, *56*, 5705–5716.

(63) Ediger, M. D.; Forrest, J. a. Dynamics near Free Surfaces and the Glass Transition in Thin Polymer Films: A View to the Future. *Macromolecules* **2014**, *47*, 471–478.

(64) Pye, J. E.; Roth, C. B. Two Simultaneous Mechanisms Causing Glass Transition Temperature Reductions in High Molecular Weight Freestanding Polymer Films as Measured by Transmission Ellipsometry. *Phys. Rev. Lett.* **2011**, *107*, 235701.

(65) Paeng, K.; Swallen, S. F.; Ediger, M. D. Direct Measurement of Molecular Motion in Freestanding Polystyrene Thin Films. *J. Am. Chem. Soc.* **2011**, *133*, 8444–8447.

(66) Miyake, K.; Satomi, N.; Sasaki, S. Elastic Modulus of Polystyrene Film from near Surface to Bulk Measured by Nanoindentation Using Atomic Force Microscopy. *Appl. Phys. Lett.* **2006**, *89*, 031925.

(67) Torres, J. M.; Stafford, C. M.; Vogt, B. D. Impact of Molecular Mass on the Elastic Modulus of Thin Polystyrene Films. *Polymer (Guildf).* **2010**, *51*, 4211–4217.

(68) Huang, J.; Juszkiewicz, M.; de Jeu, W. H.; Cerda, E.; Emrick, T.; Menon, N.; Russell, T. P. Capillary Wrinkling of Floating Thin Polymer Films. *Science* **2007**, *317*, 650–653.

(69) Kim, J.-H.; Nizami, A.; Hwangbo, Y.; Jang, B.; Lee, H.-J.; Woo, C.-S.; Hyun, S.; Kim, T.-S. Tensile Testing of Ultra-Thin Films on Water Surface. *Nat. Commun.* **2013**, *4*, 2520.

(70) Lee, J.-H.; Chung, J. Y.; Stafford, C. M. Effect of Confinement on Stiffness and Fracture of Thin Amorphous Polymer Films. *ACS Macro Lett.* **2012**, *1*, 122–126.

(71) Terence Chan, Athene M. Donald, E. J. K. Film Thickness Effects on Craze Micromechanics. *J. Mater. Sci.* **1981**, *16*, 676–686.

(72) Crosby, A. J.; Fasolka, M. J.; Beers, K. L. High-Throughput Craze Studies in Gradient Thin Films Using Ductile Copper Grids. *Macromolecules* **2004**, *37*, 9968–9974.

(73) DeGennes, P.-G. *Scaling Concepts in Polymer Physics*; Cornell University Press, Ithaca, N.Y., 1979.

(74) Sussman, D. M.; Tung, W.; Winey, K. I.; Schweizer, K. S.; Riggleman, R. a. Entanglement Reduction and Anisotropic Chain and Primitive Path Conformations in Polymer Melts under Thin Film and Cylindrical Confinement. *Macromolecules* **2014**, *47*, 6462–6472.

(75) Harris, D. J.; Lewis, J. A. Marangoni Effects on Evaporative Lithographic Patterning of Colloidal Films. *Langmuir* **2008**, *24*, 3681–3685.

(76) Lee, D. Y.; Pham, J. T.; Lawrence, J.; Lee, C. H.; Parkos, C.; Emrick, T.; Crosby, A. J. Macroscopic Nanoparticle Ribbons and Fabrics. *Adv. Mater.* **2013**, *25*, 1248–1253.

(77) Hong, S. W.; Xia, J.; Byun, M.; Zou, Q.; Lin, Z. Mesoscale Patterns Formed by Evaporation of a Polymer Solution in the Proximity of a Sphere on a Smooth Substrate : Molecular Weight and Curvature Effects. *Macromolecules* **2007**, *40*, 2831–2836.

(78) Roberson, S. V; Fahey, A. J.; Sehgal, A.; Karim, A. Multifunctional ToF-SIMS: Combinatorial Mapping of Gradient Energy Substrates. *Appl. Surf. Sci.* **2002**, *200*, 150–164.

(79) Weon, B. M.; Je, J. H. Fingering inside the Coffee Ring. *Phys. Rev. E* **2013**, *87*, 013003.

(80) Bodiguel, H.; Leng, J. Imaging the Drying of a Colloidal Suspension. *Soft Matter* **2010**, *6*, 5451.

(81) Kavehpour, P.; Ovryn, B.; McKinley, G. H. Evaporatively-Driven Marangoni Instabilities of Volatile Liquid Films Spreading on Thermally Conductive Substrates. *Colloids Surfaces A Physicochem. Eng. Asp.* **2002**, *206*, 409–423.

(82) Fournier, JB Cazabat, A. Tears of Wine. *EPL (Europhysics Lett.* **1992**, *20*, 517–522.

(83) Gennes, P. de; Brochard-Wyart, F.; Quere, D. *Capillarity and Wetting Phenomena*; Springer Science and Business Media: New York, 2004.

(84) Yabu, B. H.; Shimomura, M. Preparation of Self-Organized Mesoscale Polymer Patterns on a Solid Substrate : Continuous Pattern Formation from a Receding Meniscus. *Adv. Funct. Mater.* **2005**, *15*, 575–581.

(85) Doumenc, F.; Guerrier, B. Self-Patterning Induced by a Solutal Marangoni Effect in a Receding Drying Meniscus. *EPL (Europhysics Lett.* **2013**, *103*, 14001.

(86) Kajiya, T.; Monteux, C.; Narita, T.; Lequeux, F.; Doi, M. Contact-Line Recession Leaving a Macroscopic Polymer Film in the Drying Droplets of Water-poly(N,N-Dimethylacrylamide) (PDMA) Solution. *Langmuir* **2009**, *25*, 6934–6939.

(87) Monteux, C.; Elmaallem, Y.; Narita, T.; Lequeux, F. Advancing-Drying Droplets of Polymer Solutions: Local Increase of the Viscosity at the Contact Line. *EPL (Europhysics Lett.* **2008**, *83*, 34005.

(88) Poh, B. T.; Ong, B. T. Dependence of Viscosity of Polystyrene Solutions on Molecular Weight and Concentration. *Eur. Polym. J.* **1984**, *20*, 975–978.

(89) Han, C. C.; Akcasu, A. Z. Concentration Dependence of Diffusion Coefficient at Various Molecular Weights and Temperatures. *Polymer (Guildf).* **1981**, *22*, 1165–1168.

(90) Hu, H.; Larson, R. G. Analysis of the Effects of Marangoni Stresses on the Microflow in an Evaporating Sessile Droplet. *Langmuir* **2005**, *21*, 3972–3980.

(91) Golovko, D. S.; Butt, H.-J.; Bonaccurso, E. Transition in the Evaporation Kinetics of Water Microdrops on Hydrophilic Surfaces. *Langmuir* **2009**, *25*, 75–78.

(92) Su, G. M.; Best, K.; Ranganathan, T.; Emrick, T.; Crosby, A. J. Tailored Nanoparticles for Enhancing Polymer Adhesion. *Macromolecules* **2011**, *44*, 5256–5261.

(93) Gupta, S.; Zhang, Q.; Emrick, T.; Balazs, A. C.; Russell, T. P. Entropy-Driven Segregation of Nanoparticles to Cracks in Multilayered Composite Polymer Structures. *Nat. Mater.* **2006**, *5*, 229–233.

(94) Lee, J.-Y.; Zhang, Q.; Emrick, T.; Crosby, A. J. Nanoparticle Alignment and Repulsion during Failure of Glassy Polymer Nanocomposites. *Macromolecules* **2006**, *39*, 7392–7396.

(95) Monteux, C.; Lequeux, F. Packing and Sorting Colloids at the Contact Line of a Drying Drop. *Langmuir* **2011**, *27*, 2917–2922.

(96) Chhasatia, V. H.; Sun, Y. Interaction of Bi-Dispersed Particles with Contact Line in an Evaporating Colloidal Drop. *Soft Matter* **2011**, *7*, 10135.

(97) Deegan, R. D.; Bakajin, O.; Dupont, T. F. Capillary Flow as the Cause of Ring Stains from Dried Liquid Drops. **1997**, 827–829.

(98) Prentice, P. Influence of Molecular Weight on the Fracture of Poly (methyl methacrylate)(PMMA). *Polymer (Guildf).* **1983**, *24*, 344–350.

(99) Graessley, W. W. The Entanglement Concept in Polymer Rheology. *Adv. Polym. Sci.* **1974**, *16*, 1–179.

(100) Perelaer, J.; Smith, P. J.; Hendriks, C. E.; van den Berg, A. M. J.; Schubert, U. S. The Preferential Deposition of Silica Micro-Particles at the Boundary of Inkjet Printed Droplets. *Soft Matter* **2008**, *4*, 1072.

(101) Kirste, R.; Kruse, W.; Ibel, K. Determination of the Conformation of Polymers in the Amorphous Solid State and in Concentrated Solution by Neutron Diffraction. *Polymer (Guildf).* **1975**, 120–124.

(102) Peterson, J. D.; Vyazovkin, S.; Wight, C. a. Stabilizing Effect of Oxygen on Thermal Degradation of Poly(methyl Methacrylate). *Macromol. Rapid Commun.* **1999**, *20*, 480–483.

(103) Gupta, S.; Zhang, Q.; Emrick, T.; Balazs, A. C.; Russell, T. P. Entropy-Driven Segregation of Nanoparticles to Cracks in Multilayered Composite Polymer Structures. *Nat. Mater.* **2006**, *5*, 229–233.

(104) Balazs, A. C.; Emrick, T.; Russell, T. P. Nanoparticle Polymer Composites: Where Two Small Worlds Meet. *Science* **2006**, *314*, 1107–1110.

(105) Tang, R.; Moyano, D. F.; Subramani, C.; Yan, B.; Jeoung, E.; Tonga, G. Y.; Duncan, B.; Yeh, Y.-C.; Jiang, Z.; Kim, C.; Rotello, V. M. Rapid Coating of Surfaces with Functionalized Nanoparticles for Regulation of Cell Behavior. *Adv. Mater.* **2014**, n/a – n/a.

(106) Tseng, P.; Di Carlo, D. Substrates with Patterned Extracellular Matrix and Subcellular Stiffness Gradients Reveal Local Biomechanical Responses. *Adv. Mater.* **2013**, 1242–1247.

(107) Wang, H.; Keum, J. K.; Hiltner, A.; Baer, E.; Freeman, B.; Rozanski, A.; Galeski, A. Confined Crystallization of Polyethylene Oxide in Nanolayer Assemblies. *Science* **2009**, *323*, 757–760.

(108) Xiangfeng Duan, Chunmin Niu, Vijendra Sahi, Jian Chen, J. Wallace Parce, Stephen Empedocles, J. L. G. High-Performance Thin-Film Transistors Using Semiconductor Nanowires and Nanoribbons. *Nature* **2003**, *425*, 274–278.

(109) Cao, Q.; Kim, H.; Pimparkar, N.; Kulkarni, J. P.; Wang, C.; Shim, M.; Roy, K.; Alam, M. a; Rogers, J. a. Medium-Scale Carbon Nanotube Thin-Film Integrated Circuits on Flexible Plastic Substrates. *Nature* **2008**, *454*, 495–500.

(110) Lee, H.; Alcoutlabi, M.; Watson, J. V.; Zhang, X. Polyvinylidene Fluoride- Co -Chlorotrifluoroethylene and Polyvinylidene Fluoride- Co -Hexafluoropropylene Nanofiber-Coated Polypropylene Microporous Battery Separator Membranes. *J. Polym. Sci. Part B Polym. Phys.* **2013**, *51*, 349–357.

(111) Fakhraai, Z.; Forrest, J. a. Measuring the Surface Dynamics of Glassy Polymers. *Science* **2008**, *319*, 600–604.

(112) Miyake, K.; Satomi, N.; Sasaki, S. Elastic Modulus of Polystyrene Film from near Surface to Bulk Measured by Nanoindentation Using Atomic Force Microscopy. *Appl. Phys. Lett.* **2006**, *89*, 031925.

(113) Lauterwassera, B. D.; Kramera, E. J. Microscopic Mechanisms and Mechanics of Craze Growth and Fracture. *Philos. Mag. A* **1979**, *39*, 469–495.

(114) Edward J. Kramer and Larry L. Berger. Fundamental Processes of Craze Growth and Fracture. *Adv. Polym. Sci.* **1990**, 2–67.

(115) Lee, J.-Y.; Crosby, A. J. Crazing in Glassy Block Copolymer Thin Films. *Macromolecules* **2005**, *38*, 9711–9717.

(116) King, H.; Schroll, R. D.; Davidovitch, B.; Menon, N. Elastic Sheet on a Liquid Drop Reveals Wrinkling and Crumpling as Distinct Symmetry-Breaking Instabilities. *Proc. Natl. Acad. Sci. U. S. A.* **2012**, *109*, 9716–9720.

(117) Chai, Y.; Salez, T.; McGraw, J. D.; Benzaquen, M.; Dalnoki-Veress, K.; Raphaël, E.; Forrest, J. a. A Direct Quantitative Measure of Surface Mobility in a Glassy Polymer. *Science* **2014**, *343*, 994–999.

(118) Pham, J. T.; Lawrence, J.; Lee, D. Y.; Grason, G. M.; Emrick, T.; Crosby, A. J. Highly Stretchable Nanoparticle Helices through Geometric Asymmetry and Surface Forces. *Adv. Mater.* **2013**, *25*, 6703–6708.

(119) Brown, H. R.; Russell, T. P. Entanglements at Polymer Surfaces and Interfaces. *Macromolecules* **1996**, *27*, 798–800.

(120) Kramer, E. J. Microscopic and Molecular Fundamentals of Crazing. *Adv. Polym. Sci.* **1983**, *52-53*, 1–56.

(121) Kausch, H. H. *Polymer Fracture*; 1978.

(122) Connell, P. A. O.; Hutcheson, S. A.; Kenna, G. B. M. C. Creep Behavior of Ultra-Thin Polymer Films. *J. Polym. Sci. Part B Polym. Phys.* **2008**, *46*, 1952–1965.

(123) Dann, J. R. Forces Involved in the Adhesive Process I. Critical Surface Tensions of Polymeric Solids as Determined with Polar Liquids. *J. Colloid Interface Sci.* **1970**.

(124) Li, I. T. S.; Walker, G. C. Interfacial Free Energy Governs Single Polystyrene Chain Collapse in Water and Aqueous Solutions. *J. Am. Chem. Soc.* **2010**, *132*, 6530–6540.

(125) Ober, R.; Paz, L.; Taupin, C.; Pincus, P.; Boileau, S. Study of the Surface Tension of Polymer Solutions: Theory and Experiments. Good Solvent Conditions. *Macromolecules* **1983**, 50–55.

(126) Wu, S. Calculation of Interfacial Tension in Polymer Systems. *J. Polym. Sci. Part C Polym. Symp.* **1971**, *30*, 19–30.

(127) Koenig, S. P.; Boddeti, N. G.; Dunn, M. L.; Bunch, J. S. Ultrastrong Adhesion of Graphene Membranes. *Nat. Nanotechnol.* **2011**, *6*, 543–546.

(128) He, K.; Poole, C.; Mak, K. F.; Shan, J. Experimental Demonstration of Continuous Electronic Structure Tuning via Strain in Atomically Thin MoS2. *Nano Lett.* **2013**, *13*, 2931–2936.

(129) Alcoutlabi, M.; McKenna, G. B. Effects of Confinement on Material Behaviour at the Nanometre Size Scale. *J. Phys. Condens. Matter* **2005**, *17*, R461–R524.

(130) Zhai, M.; McKenna, G. B. Elastic Modulus and Surface Tension of a Polyurethane Rubber in Nanometer Thick Films. *Polym. (United Kingdom)* **2014**, *55*, 2725–2733.

(131) Bäumchen, O.; McGraw, J. D.; Forrest, J. a.; Dalnoki-Veress, K. Reduced Glass Transition Temperatures in Thin Polymer Films: Surface Effect or Artifact? *Phys. Rev. Lett.* **2012**, *109*, 055701.

(132) Hu, G.; Parelkar, S. S.; Emrick, T. A Facile Approach to Hydrophilic, Reverse Zwitterionic, Choline Phosphate Polymers. *Polym. Chem.* **2015**, *6*, 525–530.

(133) Fox, T. G.; Flory, P. J. Viscosity—Molecular Weight and Viscosity—Temperature Relationships for Polystyrene and Polyisobutylene1, 2. *J. Am. Chem. Soc.* **1948**, 2384–2395.

(134) Fox, T.; Allen, V. Dependence of the Zero Shear Melt Viscosity and the Related Friction Coefficient and Critical Chain Length on Measurable Characteristics of Chain Polymers. *J. Chem. Phys.* **1964**, *41*, 344–352.

(135) Raegen, A.; Chowdhury, M.; Calers, C.; Schmatulla, A.; Steiner, U.; Reiter, G. Aging of Thin Polymer Films Cast from a Near-Theta Solvent. *Phys. Rev. Lett.* **2010**, *105*, 227801.

(136) Thomas, K. R.; Chenneviere, A.; Reiter, G.; Steiner, U. Nonequilibrium Behavior of Thin Polymer Films. *Phys. Rev. E* **2011**, *83*, 021804.

(137) De Gennes, P. G. Solvent Evaporation of Spin Cast Films:“crust” Effects. *Eur. Phys. J. E Soft Matter Biol. Phys.* **2002**, *7*, 31–34.